

Density functional theory study of hydrogen storage by spillover on graphene and boron nitride sheet: doping effect and the kinetic issues

Wu, Hongyu

2012

Wu, H. Y. (2012). Density functional theory study of hydrogen storage by spillover on graphene and boron nitride sheet: doping effect and the kinetic issues. Doctoral thesis, Nanyang Technological University, Singapore.

<https://hdl.handle.net/10356/48237>

<https://doi.org/10.32657/10356/48237>



**NANYANG
TECHNOLOGICAL
UNIVERSITY**

**DENSITY FUNCTIONAL THEORY STUDY OF
HYDROGEN STORAGE BY SPILLOVER ON
GRAPHENE AND BORON NITRIDE SHEET: DOPING
EFFECT AND THE KINETIC ISSUES**

HONGYU WU

SCHOOL OF PHYSICAL & MATHEMATICAL SCIENCES

2012

**DENSITY FUNCTIONAL THEORY STUDY OF
HYDROGEN STORAGE BY SPILLOVER ON
GRAPHENE AND BORON NITRIDE SHEET: DOPING
EFFECT AND THE KINETIC ISSUES**

HONGYU WU

(M.Sc. Beijing University, P. R. China)

Division of Physics & Applied Physics

School of Physical & Mathematical Sciences

A Thesis Submitted to Nanyang Technological University in Partial
Fulfillment of the Requirements for the Degree of Doctor of Philosophy
in Physics

2012

ACKNOWLEDGMENTS

First of all, I would like to express my sincere thanks to my supervisors: Dr. Kuo Jer-Lai and Prof. Shen Zexiang. As an expert in the computational science, Dr. Kuo patiently guided me through the whole Ph.D. program and taught me a lot of valuable research skills from his own academic experiences. His hard-working and humbleness also set a good example for me. As a knowledgeable experimentalist, Prof. Shen provided me with many helpful suggestions on the research project, and that enriched my work in terms of practical applications. I really appreciate their wholehearted help and support throughout my Ph.D. project.

During my stay at DICP in China, I also had a great collaboration experience with Dr. Deng Wei-Qiao. Dr. Deng has an acute sense on the research tides and his quick thinking also impresses me. I am grateful to him and his group members for their support on my project.

Another big thank goes to my senior colleague Dr. Fan Xiaofeng, who is actually a valuable asset in our research group. We had gone through a wonderful time working together, and he was always willing to help and gave constructive advices whenever I met difficulties. Most importantly, we have built a deep friendship through the cooperation.

Many thanks to my group colleagues, Dr. Bing Dan, Dr. Nguyen Quoc Chinh, Dr. Guan Lixiu, Miss Zhang Jingyun, Miss Zhang Xi, Dr. Xie Zhizhong, Dr. Zhu Zexuan, and Dr. Xiao Zhiren, who have become my friends and made life colourful. I also would like to thank the people in Dr. Kuo' group at IAMS in Taiwan, for their hospitality during my stay in Taipei. There are still a lot of peers and staffs to thank at SPMS, and I appreciate their numerous help all these years.

Last but not least, I would like to extend my thanks to my family for their comprehension, support and encouragement all the way.

Table of Contents

Acknowledgments	i
Table of Contents	ii
Summary	v
List of Figures	vii
List of Tables	xii
Publications	xiii

Chapter 1 Introduction

1.1 Hydrogen energy chain	1
1.2 Hydrogen storage	3
1.2.1 Sorbents	4
1.2.2 Metal hydrides	5
1.2.3 Chemical hydrides	6
1.3 Material simulations on hydrogen storage property	7
1.4 Summary	9

Chapter 2 Overview of Density Functional Theory

2.1 Thomas-Fermi approximation	10
2.2 Hartree-Fock approximation	11
2.3 Density functional theory	13
2.3.1 Hohenberg-Kohn theorems	13
2.3.2 Kohn-Sham equations	14
2.3.3 Local density approximation	16
2.3.4 Generalized gradient approximation	17
2.3.5 Hybrid functional B3LYP	18

2.4 Summary	18
-------------	----

Chapter 3 DFT Study of Hydrogen Storage by Spillover on Graphene with Boron Substitution

3.1 Introduction	19
3.2 Computational methods	21
3.3 Results and discussion	22
3.3.1 Adsorption of H on pure graphene and 1B-doped graphene sheet	22
3.3.2 Hydrogen adsorption on Pt ₄ cluster supported by G or G _B sheet	26
3.3.3 H migration from Pt ₄ cluster onto the supporting G/G _B sheet	28
3.3.4 Hydrogen spillover on BC ₃ sheet	30
3.4 Summary	36

Chapter 4 DFT Study of Hydrogen Spillover on Nitrogen Doped Graphene

4.1 Introduction	37
4.2 Computational methods	38
4.3 Results and discussion	38
4.3.1 Adsorption of H on 1N-doped graphene sheet	38
4.3.2 Hydrogen adsorption and migration on Pt ₄ -supported G _N sheet	40
4.3.3 Adsorption of H on pyridinic-N doped graphene sheet	43
4.3.4 Hydrogen adsorption and migration on Pt ₄ -supported G _{pyr-N} sheet	45
4.3.5 Comparison between B-doped and N-doped graphene for the H spillover	48
4.4 Summary	49

Chapter 5 DFT Study of Hydrogen Spillover on Carbon Doped Boron Nitride Sheet

5.1 Introduction	50
5.2 Computational methods	51
5.3 Results and discussion	52
5.3.1 Adsorption of H on boron nitride sheet and 1C-doped BN sheet	52

5.3.2 Hydrogen adsorption on Pt ₄ cluster supported by C-doped BN sheet	56
5.3.3 H migration from Pt ₄ cluster onto the supporting BN-C _{B(N)} sheet	57
5.3.4 Comparison between B/N-doped graphene and C-doped BN sheet for the H spillover	59
5.4 Summary	60

Chapter 6 DFT Study of Hydrogen Storage on Carbon Doped Boron

Nitride Fullerene

6.1 Introduction	61
6.2 Computational methods	62
6.3 Results and discussion	64
6.3.1 Thermodynamics of hydrogen chemisorption on C-doped BN fullerenes	64
6.3.2 Kinetics of the hydrogenation reaction on C-doped BN fullerenes	67
6.3.3 Curvature effect on the hydrogenation kinetics of C-doped BN fullerenes	71
6.4 Summary	74

Chapter 7 Conclusions and Future Work

7.1 Conclusions	75
7.2 Future work	76
References	78

Summary

The lack of efficient hydrogen storage materials has hindered the potential use of hydrogen as fuel for transportation, personal electronics and other portable power applications. Hydrogen spillover has been experimentally demonstrated to be an effective approach for hydrogen storage applications. To have a fundamental understanding of the hydrogen spillover mechanism, theoretical investigations on the doping effect and the kinetic issues of the hydrogen storage by spillover on graphene and boron nitride sheet have been carried out in this thesis.

By incorporating boron into the graphene sheet, DFT calculations have shown that B-doping can effectively enhance the hydrogen adsorption strength of graphene. Compared with the undoped case, the metal catalyst (Pt_4) has higher stability on B-doped graphene, where more H_2 molecules can readily dissociate into H atoms on the supported metal cluster, which then serves as a steady H source for the subsequent H migration process. The estimated activation barrier for H migration from metal to substrate is much lower than that for the undoped case. The BC_3 sheet with boron atoms uniformly distributed is then investigated. According to our calculations, the activation barriers for both H migration and diffusion on the BC_3 sheet are less than 0.7 eV, thus more hydrogen can adsorb on B-doped graphene than on the pristine graphene under ambient conditions. Our theoretical result is a good support of the experimental findings that B-doped microporous carbon has an enhanced hydrogen storage capacity. With proper metal catalyst, the BC_3 sheet could be a potential candidate of hydrogen storage material.

Further investigations on the N-doped graphene show that the pyridinic-N doping is the favored method for hydrogen spillover rather than the graphitic-N doping. Higher stability of metal catalyst and more dissociated hydrogen can be obtained on the pyridinic-N doped graphene, compared with the graphitic-N doped case. The activation barrier for H migration from the Pt_4 cluster to the pyridinic-N doped graphene is estimated to be around 1 eV, indicating that pyridinic-N doping

could be an effective approach in modifying graphitic surface for hydrogen storage applications by H spillover, and further improvement on the H spillover kinetics for N-doped graphene is highly desired.

As an analogue of B/N-doped graphene, C-doped boron nitride sheet has also been investigated on the H spillover effect. Replacing one N by a C (BN-C_N) is favored over replacing one B by a C (BN-C_B) on the BN sheet. However, the estimated activation barrier for H migration from metal to substrate is as high as ~ 1.4 eV for the BN-C_N sheet, indicating the difficulty for the hydrogen spillover at ambient conditions. Therefore, graphene based materials have advantages over BN sheet based materials for hydrogen storage applications by H spillover.

Another form of BN materials, the boron nitride fullerene, has been studied on the hydrogen storage properties. First-principles calculations show that C-doping has great tunability of the thermodynamic properties of BN fullerenes, and the B₁₁N₁₂C compound is predicted to be able to reversibly store up to 7.43 wt% hydrogen under ambient conditions. Further investigation on the hydrogenation kinetics shows that the hydrogenation reaction on C-doped BN fullerene is a metal free and self-catalyzed process, in which the H₂ molecule can be effectively dissociated on the C atom as an activation center, with the corresponding activation barrier for the H₂ chemisorption substantially lowered, compared with the pristine BN fullerene. A clear curvature effect is found for the hydrogenation of the BN fullerene, that small BN nanocage with large curvature is favorable for practical applications as hydrogen storage material. We hope that our research work will stimulate the experimental effort in this direction.

List of Figures

1.1 The hydrogen energy chain in the long term.

3.1 (a-d) Deformation electron density isosurfaces of the four hydrogenated structures in Table 3.1 illustrated by top views (green, electron accumulation; yellow, electron depletion); (e-h) Hirshfeld charge distributions of the four hydrogenated structures in Table 3.1 illustrated by side views (H, white; B, pink; C, grey).

3.2 Optimized structures of (a) Pt₄ cluster on pure graphene (G-Pt₄), (b) Pt₄ cluster on G_B sheet (G_B-Pt₄), (c) saturated Pt₄ cluster on graphene with 10 H atoms chemisorbed (G-Pt₄-10H), and (d) saturated Pt₄ cluster on G_B sheet with 14 H atoms chemisorbed (G_B-Pt₄-14H) (H, white; B, pink; C, grey; Pt, cyan). The binding strength of Pt₄ $|\Delta E_{\text{Pt}}|$ on G_B sheet is 2.379 eV, much stronger than that of 1.184 eV on graphene. The chemisorption energy per H atom ΔE_{chem} for the saturated Pt₄ cluster on G and G_B sheet is -2.841 eV and -2.702 eV, respectively, indicating a strong H₂ dissociation ability for the metal cluster.

3.3 Optimized structures of initial (R), transition (TS), and final (P) states for the H migration process from saturated Pt₄ cluster to the supporting G/G_B substrate. The black bars denote the relative energy levels of these structures, with the corresponding schematic diagrams (H, white; B, pink; C, grey; Pt, cyan) drawn above or below. The calculated activation energy E_a for the H migration from Pt₄ to G and G_B sheet is 2.721 eV and 1.940 eV, respectively. The purple and blue dashed arrows are respectively used to guide the eyes for the two separate migration reactions on G and G_B substrates. The reaction energy of the migration E_m with respect to the initial state is estimated to be 2.198 eV and 1.578 eV, respectively, for the G and G_B cases.

3.4 Optimized structures of (a) BC₃ sheet (G_{BC₃}), (b) H adsorption on B in G_{BC₃} (G_{BC₃}-B-H), (c) H adsorption on C in G_{BC₃} (G_{BC₃}-C-H), (d) Pt₄ cluster on G_{BC₃} (G_{BC₃}-Pt₄), and (e) saturated Pt₄ cluster on G_{BC₃} with 14 H atoms chemisorbed (G_{BC₃}-Pt₄-14H) (H, white; B, pink; C, grey; Pt, cyan). A (3×3) supercell was used for

modelling the BC₃ substrate. The optimized bond length of C-C (d_{C-C}) and B-C (d_{B-C}) for G_{BC₃} is 1.422 Å and 1.567 Å, respectively.

3.5 Calculated reaction diagrams of (a) H migration from saturated Pt₄ to C on the BC₃ sheet, (b) H diffusion along the C-C path on G_{BC₃}, and (c) H diffusion along the C-B-C path on G_{BC₃}. The schematic diagrams of initial (IS), transition (TS), intermediate (IMS), and final (FS) states involved in the reactions are illustrated by top views (H, white; B, pink; C, grey; Pt, cyan). The reactive H atom is highlighted by red. The lines that link critical points are used to guide the eyes. The energy of reactant in each reaction diagram is set to be zero.

3.6 Evolution profiles of migration reaction energy E_m , hydrogen adsorption energy ΔE_H , and average H chemisorption energy ΔE_{chem} for the G, G_B, and G_{BC₃} sheets. The binding energy of H₂ molecule per H atom $E_{H-bind} = -2.272$ eV is denoted with a horizontal line. The single-arrow line points downward from E_{H-bind} to ΔE_{chem} , indicating the energetically favored H₂ dissociation process on the catalytic metal, and then points upward from ΔE_{chem} to ΔE_H , showing that the H migration from metal to substrate is endothermic. The difference between ΔE_{chem} and ΔE_H is labeled beside the single-arrow line.

4.1 (a,b) Deformation electron density isosurfaces of the two hydrogenated structures for G_N sheet in Table 4.1 illustrated by top views (green, electron accumulation; yellow, electron depletion); (c,d) Hirshfeld charge distributions of the two hydrogenated structures for G_N sheet in Table 4.1 illustrated by side views (H, white; N, blue; C, grey).

4.2 Optimized structures of (a) Pt₄ cluster on G_N sheet (G_N-Pt₄), and (b) saturated Pt₄ cluster on G_N sheet with 10 H atoms chemisorbed (G_N-Pt₄-10H) (H, white; N, blue; C, grey; Pt, cyan). The binding strength of Pt₄ $|\Delta E_{Pt}|$ on G_N sheet is 1.582 eV, a little bit stronger than that of 1.184 eV for the undoped graphene case. The chemisorption energy per H atom ΔE_{chem} for the saturated Pt₄ cluster on G_N sheet is about -2.802 eV, indicating a strong H₂ dissociation ability for the metal cluster.

4.3 Optimized structures of initial (R), transition (TS), and final (P) states for the H migration process from saturated Pt₄ cluster to the supporting G_N sheet. The black bars denote the relative energy levels of these structures, with the corresponding schematic diagrams (H, white; N, blue; C, grey; Pt, cyan) drawn aside. The calculated activation energy E_a for the H migration from Pt₄ to the G_N sheet is 1.994 eV. The reaction energy of the migration E_m with respect to the initial state is estimated to be 1.576 eV. The dashed arrows are used to guide the eyes.

4.4 (a,b) Schematic diagrams of two lowest-energy structures for hydrogenated G_{pyr-N} sheet illustrated by side views (H, white; N, blue; C, grey); (c,d) Top views of deformation electron density isosurfaces of (a,b) (green, electron accumulation; yellow, electron depletion); (e,f) Side views of Hirshfeld charge distributions of (a,b).

4.5 Optimized structures of (a) Pt₄ cluster on G_{pyr-N} sheet (G_{pyr-N}-Pt₄), and (b) saturated Pt₄ cluster on G_{pyr-N} sheet with 16 H atoms chemisorbed (G_{pyr-N}-Pt₄-16H) (H, white; N, blue; C, grey; Pt, cyan). The binding strength of Pt₄ $|\Delta E_{Pt}|$ on G_{pyr-N} sheet is 3.925 eV, much stronger than that for G_N-Pt₄. The average chemisorption strength per H atom $|\Delta E_{chem}|$ for the saturated Pt₄ cluster on G_{pyr-N} sheet is about 2.709 eV, which is weaker than that for G_N-Pt₄-10H.

4.6 Optimized structures of initial (R), transition (TS), and final (P) states for the H migration process from saturated Pt₄ cluster to the supporting G_{pyr-N} sheet. The black bars denote the relative energy levels of these structures, with the corresponding schematic diagrams (H, white; N, blue; C, grey; Pt, cyan) drawn aside. The calculated activation energy E_a for the H migration from Pt₄ to the G_{pyr-N} sheet is about 1.052 eV. The reaction energy of the migration E_m with respect to the initial state is estimated to be 0.675 eV. The dashed arrows are used to guide the eyes.

5.1 Deformation electron density isosurfaces of the six hydrogenated structures in Table 5.1 illustrated by top views (green, electron accumulation; yellow, electron depletion).

5.2 Optimized structures of (a) Pt₄ cluster on BN-C_B sheet (BN-C_B-Pt₄), (b) Pt₄ cluster on BN-C_N sheet (BN-C_N-Pt₄), (c) saturated Pt₄ cluster on BN-C_B with 10 H atoms chemisorbed (BN-C_B-Pt₄-10H), and (d) saturated Pt₄ cluster on BN-C_N sheet with 16

H atoms chemisorbed (BN-C_N-Pt₄-16H) (H, white; B, pink; C, grey; N, blue; Pt, cyan). The binding strength of Pt₄ $|\Delta E_{\text{Pt}}|$ on BN-C_N sheet is 3.275 eV, stronger than that of 2.869 eV on BN-C_B sheet. The chemisorption energy per H atom ΔE_{chem} for the saturated Pt₄ cluster on BN-C_B and BN-C_N sheet is -2.770 eV and -2.658 eV, respectively, indicating a strong H₂ dissociation ability for the metal cluster.

5.3 Optimized structures of initial (R), transition (TS), and final (P) states for the H migration process from saturated Pt₄ cluster to the supporting BN-C_{B(N)} substrate. The black bars denote the relative energy levels of these structures, with the corresponding schematic diagrams (H, white; B, pink; C, grey; N, blue; Pt, cyan) drawn above or below. The calculated activation energy E_a for the H migration from Pt₄ to BN-C_B and BN-C_N sheet is 2.313 eV and 1.418 eV, respectively. The purple and blue dashed arrows are respectively used to guide the eyes for the two separate migration reactions on BN-C_B and BN-C_N substrates. The reaction energy of the migration E_m with respect to the initial state is estimated to be 1.917 eV and 0.640 eV, respectively, for the BN-C_B and BN-C_N cases.

6.1 (BN)₁₂ fullerene with an overall symmetry of T_h , composed of six squares and eight hexagons. All B sites are equivalent, so are all N.

6.2 Calculated hydrogenation reaction diagram for the undoped B₁₂N₁₂ fullerene. The schematic diagrams of initial (IS), transition (TS), and final (FS) states are illustrated by side views (H, white; B, pink; N, blue.). The energy of the reactant (IS), which corresponds to the H₂ physisorption state of B₁₂N₁₂, is set to be zero. The activation barrier for the H₂ adsorption on B₁₂N₁₂ is about 1.194 eV, and the energy of product (FS) with respect to reactant (IS) is estimated to be -0.464 eV.

6.3 Calculated hydrogenation reaction diagram for the B₁₁N₁₂C fullerene. The schematic diagrams of initial (IS), transition (TS), intermediate (IMS), and final (FS) states are illustrated by side views beside each energy bar (H, white; B, pink; C, grey; N, blue.). The energy of the reactant (IS), which corresponds to the H₂ physisorption state of B₁₁N₁₂C, is set to be zero. The overall activation barrier for the H₂ adsorption on B₁₁N₁₂C is estimated to be 0.677 eV, much lower than that for the undoped B₁₂N₁₂ case. The energy of product (FS) with respect to reactant (IS) is around -0.411 eV,

indicating a thermodynamically favored hydrogenation reaction for the $B_{11}N_{12}C$ nanocage.

6.4 (a) $(BN)_{16}$ fullerene under the symmetry of T_d , composed of six squares and twelve hexagons; (b) $(BN)_{24}$ fullerene under the symmetry of O , composed of twelve squares, eight hexagons and six octagons.

List of Tables

3.1 Calculated hydrogen adsorption energy (ΔE_H), the corresponding H-bond length (d_{C-H}/d_{B-H}), and the Hirshfeld charges of B and H-bond related atoms, for the hydrogenation on pure graphene (G) and 1B-doped graphene sheet (G_B).

4.1 Calculated hydrogen adsorption energy (ΔE_H), the corresponding H-bond length (d_{C-H}), and the Hirshfeld charges of N and H-bond related atoms, for the hydrogenation on pure graphene (G) and 1N-doped graphene sheet (G_N).

5.1 Calculated hydrogen adsorption energy (ΔE_H), the corresponding H-bond length ($d_{C-H}/d_{B(N)-H}$), and the Hirshfeld charges of C and H-bond related atoms, for the hydrogenation on boron nitride sheet and 1C-doped BN sheet ($BN-C_{B(N)}$).

6.1 Calculated thermodynamic data (ΔH_e , ΔG , ΔG_1 , ΔG_2 , kJ/mol; ΔS_e , J/mol-K) per mole of H_2 gas (average values of full hydrogenation) adsorbed/released in the hydrogenation reaction of the BNC, and the maximum hydrogen content (wt%) of the corresponding BNC_H . T_e ($^{\circ}C$) refers to the temperature when Gibbs free energy change for the dehydrogenation reaction equals zero. The front views of investigated BNC molecules are shown (B, pink; C, grey; N, blue).

6.2 Calculated activation energy (E_a), reaction energy (E_r), and the H-H bond distance (d_{H-H}) in the transition state, for the hydrogenation reaction on pristine/C-doped $(BN)_{16}$ and $(BN)_{24}$ fullerenes. The side views of the transition states (TS) for the hydrogen dissociation on these clusters are shown (H, white; B, pink; C, grey; N, blue).

Publications during my Ph. D. study at NTU

1. **H. Y. Wu**, X. F. Fan, and Jer-Lai Kuo, “*Metal free hydrogenation reaction on carbon doped boron nitride fullerene: a DFT study on the kinetic issue*”, submitted to International Journal of Hydrogen Energy.
2. **H. Y. Wu**, X. F. Fan, Jer-Lai Kuo and Wei-Qiao Deng, “*DFT study of hydrogen storage by spillover on graphene with boron substitution*”, Journal of Physical Chemistry C **115**, 9241 (2011).
3. **H. Y. Wu**, X. F. Fan, Jer-Lai Kuo and Wei-Qiao Deng, “*Carbon doped boron nitride cages as competitive candidates for hydrogen storage materials*”, Chemical Communications **46**, 883 (2010).
4. **H. Y. Wu**, X. F. Fan, and Jer-Lai Kuo, “*Direct enumeration of wurtzite BC_2N configurations for structural stability and hardness evaluation*”, Diamond and Related Materials **19**, 100 (2010).
5. X. F. Fan, **H. Y. Wu**, Z. X. Shen, and Jer-Lai Kuo, “*A first-principle study on the structure, stability and hardness of cubic BC_2N* ”, Diamond and Related Materials **18**, 1278 (2009).

Chapter 1

Introduction

Hydrogen has been considered to have the long-term potential to provide a more secure, sustainable and affordable energy future for human beings. To achieve this promising goal, plenty of time, effort and money have been devoted to accelerate the implementation of the hydrogen energy chain in our daily life. In this chapter, we are going to have a brief view of the hydrogen fuel and state its advantages over the traditional fossil fuels. With a focus on the hydrogen storage, the middle link in the hydrogen energy chain, the critical challenges and some potential candidates for the hydrogen storage materials will be reviewed. Finally, we shall have a look at the theoretical efforts in exploring the hydrogen storage materials.

1.1 Hydrogen energy chain

The world is developing at an unprecedented pace. Tremendous changes in our ordinary life have taken place, along with the rapid progress in science and technology. Nowadays, there is a great abundance of materials and wealth in the economic life. At the meantime, the demand for material wealth increases daily as the global population grows. However, the material production is at the expense of energy source consumptions and the contradiction between the depleted sources and the growing needs for energy is more and more sharpening.

The primary energy consumptions all over the world are based on the fossil fuels, which include coal, oil and natural gas. The fossil fuels are usually formed through complex geological processes over millions of years. Since they are unrecoverable once used up in a short period on the geological time scale, the fossil fuels are non-renewable energy sources. As a result, the prices of fossil fuels, especially the oil prices, rise fast while their reserves decline on the earth. Since the distribution of fossil fuels on the earth is nonuniform, many countries have to spend an enormous amount of money on the energy import every year. This is certainly a great burden for

the economy of these countries. Sometimes, there are even geopolitical issues raised by the conspiracy to plunder these limited resources. Furthermore, the fossil fuels have high concentrations of carbon; hence the burning of them will give off plenty of carbon dioxide, one of the greenhouse gases. Since the emitted carbon dioxide is too much to be absorbed by nature, it aggravates the global warming and the climate on the earth becomes abnormal as a consequence.

To solve this series of problems, people began to find other energy sources as the alternative to the fossil fuels. Hydrogen, which is abundant in water and many organic compounds, has later been considered to have a great potential to change the current energy chain status quo. A big advantage of hydrogen over the fossil fuels is that the combustion of hydrogen will only produce water and heat, without emissions of other pollutant gases like carbon dioxide. In addition, the hydrogen can be combined with oxygen to generate electricity with high efficiency in the fuel cells, which then can be incorporated in many end applications such as transportation, portable electronics and stationary generation. Therefore, in the long run, an energy chain based on hydrogen (Figure 1.1) should be like:

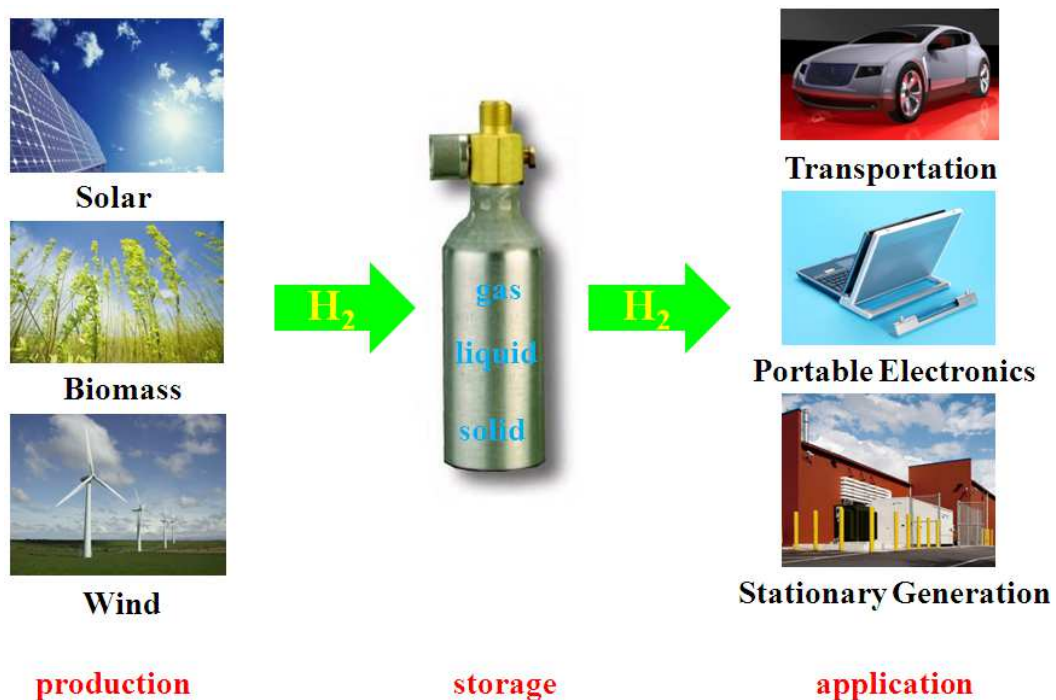


Figure 1.1 The hydrogen energy chain in the long term.

(a) The hydrogen is produced from some renewable energy sources such as solar or wind energy through the electrolysis of water, and the biomass via photosynthesis;

(b) The produced hydrogen is then stored into some storage medium in the form of gas, liquid or solid;

(c) Eventually hydrogen is released from the storage medium to be used in fuel cells for power supplies, and the resultant water can be recycled for another hydrogen production.

In this way, from production, to storage, and to application, a sustainable hydrogen energy chain is established, which will greatly reduce our dependence on oil and the emission of pollutant gases.

However, the energy revolution doesn't happen overnight. There are still lots of difficulties to overcome. Right now, the technologies for hydrogen production from renewable energy sources still need much improvement, in order to increase the energy transfer efficiency and lower the production cost. The relative infrastructure for fuel cell vehicles and stationary applications is far yet to meet the requirements for the energy transfer from fossil to hydrogen. As for the hydrogen storage, the lack of effective storage media for on-board applications has greatly hindered the potential use of the hydrogen fuel. Since the topic of this thesis is related to the hydrogen storage materials, I will discuss this point especially in the following sections.

1.2 Hydrogen storage

As the middle link of the hydrogen energy chain, hydrogen storage has attracted much attention of research scientists. Currently, the main methods for hydrogen storage are limited to compressed gas and liquefaction. On one hand, the tank for storing the compressed hydrogen gas usually is of bulk size, which is not appropriate to be carried by electrical vehicles and portable electronics using fuel cells; on the other hand, the liquefaction of hydrogen requires energy to cool it down to a very low temperature (~ 20 K), thus a large energy loss is inevitable during the process. To facilitate the use of hydrogen fuel for on-board applications, solid materials that can

bind or adsorb hydrogen and liquid hydrides, are then highly expected to meet the critical hydrogen storage challenges,¹⁻³ which involve high hydrogen storage capacity, ambient conditions operation, reversibility of storage and fast charge/release kinetics. In the following, I will give a brief account of some potential candidates for hydrogen storage materials, and state the pros and cons of each kind.

1.2.1 Sorbents

The sorbent materials are usually nanoporous materials, which can physically adsorb hydrogen molecules via van der Waals interactions. These materials have large surface areas and can store hydrogen with ready reversibility. However, the physisorption energy of H₂ is so weak (~ 1 kcal/mol) that low temperatures (~ 77 K) are needed for the materials to achieve a reasonable hydrogen content.

Carbon-based materials,⁴⁻⁶ organic polymers⁷⁻⁹ and metal-organic frameworks¹⁰⁻¹² in terms of sorbents have received extensive investigations. It was reported that the heat of adsorption of H₂ is related to the pore size of the sorbent materials,¹³ and the zeolite-templating method, which uses zeolite structures as a template to form microporous carbons, seems to be a good approach to control the pore size of materials. The hydrogen storage capacity of 6.9 wt% was achieved at 77 K and 20 bar on such kinds of zeolite-like carbon materials.⁶ Alternatively, organic polymers with intrinsic microporosity can also have tunable surface area and pore size. Such kinds of polymers are rigid and contorted macromolecules, made of small organic molecules, which can link with each other to produce microporosity and even ultramicroporosity.⁸ Recent research reported that the hydrogen storage amount could reach up to 6.1 wt% at 77 K and 1 bar for lithium-doped microporous organic polymers.⁹ Similarly, organic molecules can also link between metal ions or clusters to form metal-organic frameworks (MOF), whose porosity can be modulated with different metal and organic bridges for hydrogen storage applications.¹⁰ The incorporation of proper cations into the pores of MOF can form a kinetic trap for H₂ with increased heat of adsorption.¹² However, the hydrogen gravimetric capacity of MOF is usually low due to the inclusion of metals, which still needs further

optimizations for practical applications.

Recently, as an effective approach for hydrogen storage at ambient temperature, hydrogen spillover has been experimentally demonstrated by Yang and co-workers on many sorbent materials, including graphite nanofibers,¹⁴ carbon nanotubes,¹⁴⁻¹⁶ activated carbons,^{14, 16} metal-organic frameworks¹⁷⁻¹⁹ and covalent-organic frameworks.¹⁹ In these experiments, carbon substrate materials were doped with metal catalysts, which dissociated the H₂ molecules into H atoms. Then the H atoms migrated from metal to the supporting carbon materials and further diffused on the carbon substrate. With this hydrogen spillover process, significant enhancements of hydrogen uptake at 298 K by a factor of ca. 3 were observed, and the storage was found to be reversible with fast rates. Since the spillover process involves H₂ dissociation on the metal and H diffusion on the substrate, the overall heat of adsorption of hydrogen on the sorbent materials can be seen as a combination of chemisorption and physisorption, which will facilitate the hydrogen storage applications at ambient conditions. As the main topic of this thesis, hydrogen spillover will be discussed in detail later in several chapters.

1.2.2 Metal hydrides

Different from the physisorption manner of sorbent materials, metal hydrides as potential hydrogen storage materials rely on chemisorption to reversibly store hydrogen. Since the chemical interaction between metal and hydrogen is strong, metal hydrides are stable at ambient conditions. However, high temperatures (> 150 °C) are usually required to release the hydrogen. The hydrogen gravimetric capacity of metal hydrides is not high due to the existence of relatively heavy metals. The dehydrogenation and rehydrogenation kinetics of metal hydrides also need improvement for practical applications.

Sodium alanate (NaAlH₄) is a well-known metal hydride, which can reversibly store ~ 3 wt% of hydrogen, when doped with titanium compounds.²⁰ The catalytic titanium compounds can significantly enhance the kinetics of dehydrogenation and rehydrogenation of NaAlH₄. Later investigation found that further improvement of

dehydrogenation kinetics could be achieved by introducing titanium catalyst into the NaAlH₄ host with dry doping method instead of the wet doping method.²¹ To increase the hydrogen gravimetric capacity of materials, light weight elements such as boron and nitrogen are introduced to form complex metal hydrides. By properly choosing the reaction couples of two hydrides, reversible dehydrogenation can be achieved.²²⁻²⁴ It was reported that mechanically milled mixtures of LiBH₄ and MgH₂ can reversibly store 8-10 wt% hydrogen at 350-450 °C; however, the reaction rates are too low for practical applications.²³ Direct thermal decomposition of some complex metal hydrides is another way to release hydrogen reversibly.^{25, 26} Recently, dehydrogenation of solid state Mg(BH₄)₂ was reported to occur at 200 °C, and the reverse process takes place at 250 °C under 120 atm H₂, with a 2.5 wt% hydrogen cycling capacity.²⁶ The thermodynamics for the reverse reaction will be more favorable if a less stable metal hydride is formed in the decomposition process.

1.2.3 Chemical hydrides

Similar to metal hydrides, chemical hydrides also implement the chemisorption manner as a potential hydrogen storage material. Since they typically consist of light elements such as boron, carbon and nitrogen, the chemical hydrides can have relatively high gravimetric capacity of hydrogen. To achieve the reversibility for practical applications, usually the Gibbs free energy (ΔG) for the dehydrogenation of chemical hydrides is required to be near zero, with the corresponding reaction enthalpy (ΔH) being slightly positive. The reaction kinetics is another challenge for the chemical hydrides to meet.

As typical chemical hydrides, cyclic organic molecules have been proposed for hydrogen storage applications.²⁷ Since the dehydrogenation reaction of such organic hydrides is highly endothermic, metal catalysts and high temperatures (> 200 °C) are needed to facilitate the hydrogen release. Later investigations showed that the incorporation of nitrogen atoms into the organic molecules could greatly change the reaction chemistry of the materials.^{28, 29} The N-containing heterocyclic organic

hydrides can release hydrogen at 110 °C, with the dehydrogenation both thermodynamically and kinetically improved, compared with the undoped case.²⁸ Furthermore, the co-doping of boron and nitrogen, where the B-N bond replaces the C-C bond of the organic molecule, also shows great tunability of the thermodynamical properties of the material.³⁰

Ammonia borane ($\text{H}_3\text{N-BH}_3$, AB) is another appealing chemical hydride and has received particular attention for hydrogen storage applications.^{31,32} The big advantage of AB is that it possesses approximately 20 wt% hydrogen, an extremely high energy density. The existence of both hydridic (B-H) and protic (N-H) bonds in AB also facilitates the hydrogen release process. However, pure AB has slow hydrogen release rate and its regeneration efficiency is also a problem to solve. Ionic liquids (IL) were reported to be advantageous media for AB dehydrogenation.³³ Upon heating at 85 °C, the ammonia borane in IL began to release hydrogen immediately, while the solid state AB needed an initial induction period before hydrogen production. In addition, more hydrogen were produced by AB in IL, compared with the solid state AB case. Alternatively, using strong Lewis or Brønsted acids could also promote the hydrogen release from AB, however, the efficient way to regenerate AB is still not clear.³⁴ Recently, quantitative conversion of AB spent fuel was demonstrated to be possible.³⁵ After 24-hour treatment of the highly dehydrogenated AB with hydrazine (N_2H_4) in liquid ammonia (NH_3) at 40 °C, AB could be regenerated with a conversion rate of 92%, which shed light on the development of AB regeneration methods.

1.3 Material simulations on hydrogen storage property

Besides the experimental effort in exploring applicable hydrogen storage materials, more and more studies have turned to theoretical simulations on the hydrogen storage properties of materials. As the computer technology develops fast, material simulations have become the virtual experiments for the scientists who can save cost and time in studying interested properties of materials. Since this thesis is based on the computational study of hydrogen storage materials, I will talk about some commonly used computational methods for investigating hydrogen storage

materials in the following. We will see how theoretical work helps the real experiments in materials design and synthesis.

Grand canonical Monte Carlo (GCMC) simulations have been widely used to study various sorbent materials.^{9, 36-39} In GCMC simulations, by randomly distributing the H₂ molecules all around the sorbent materials, the total adsorption amount of H₂ can be obtained when the simulated system reaches equilibrium at the fixed temperature and pressure. If the employed force fields describing the interactions between H₂ and sorbent, as well as H₂ and H₂ are accurate enough, most GCMC results of H₂ uptake isotherms can have good agreements with the experimental measurements. A big advantage of simulation study is that, the structural models of sorbent materials can be easily built in the computer programs, and one can implement many strategies to design new hypothetical materials with high hydrogen storage capacity through simulations, which helps the experiments in synthesizing most promising hydrogen storage materials.³⁹

Reaction kinetics is a key issue for hydrogen storage applications. However, it is difficult for the experiments to characterize the microscopic behaviors of hydrogen in the storage media. In this aspect, molecular dynamics (MD) simulations are very helpful in investigating the diffusion mechanisms of hydrogen storage materials.⁴⁰⁻⁴² By numerically solving the Newton's equations of motion for a system, the trajectories of the atoms and molecules in the system can be determined in MD simulations, thus the evolution of the system can be realized at certain temperature and pressure. A good example of using the MD simulation in the study of diffusion mechanisms is that, the diffusion of AlH₃ vacancies rather than NaH vacancies has been identified to be the rate-limiting step for the dehydrogenation of Ti-doped NaAlH₄, since the calculated activation barrier for the decomposition of NaAlH₄ via the AlH₃ vacancy is in good agreement with the experimental data.⁴⁰ Moreover, the structure stability can also be tested for the proposed hydrogen storage materials via MD simulations. Whether the materials are capable of storing high amount of hydrogen under ambient conditions would be clear to see after the simulations.^{43, 44}

Density functional theory^{45, 46} (DFT) is the most popular calculation method used

to study hydrogen storage materials. By solving the Schrödinger equation, which is expressed by electron density of the system, the total energy of the system at 0 K can be calculated by DFT. In this way, the binding energy of hydrogen in the storage medium can thus be obtained, which can be used to guide the design of materials with favorable hydrogen binding strength.^{47, 48} Since the theoretical calculation is based on the structural model of the material, structure prediction via DFT is also possible for some hydrogen storage materials.^{49, 50} In addition, by evaluating the vibrational modes of the system, many thermodynamic properties such as entropy, enthalpy, Gibbs free energy etc. can also be obtained for the materials under certain temperature and pressure.⁵¹ Therefore, DFT becomes a powerful tool in efficiently screening potential metal hydrides with favored reaction thermodynamics for hydrogen storage applications.⁵² New ideas on the material designs are also readily tested by DFT calculations, due to the easy modifications of structural models in the computer programs. For example, charging⁵³ and electrical field⁵⁴ are theoretically predicted to be effective approaches in achieving high hydrogen storage capacity, which provides new thoughts for experiments in designing hydrogen storage materials.

1.4 Summary

Hydrogen fuel has been considered to be a promising alternative to the traditional fossil fuel for many practical applications. However, the lack of efficient storage material, which can reversibly store hydrogen with high amount and fast kinetics under ambient conditions, has greatly hindered the massive use of the hydrogen fuel. Several potential candidates of hydrogen storage materials such as sorbents, metal hydrides and chemical hydrides have received intensive investigations, and great achievements have been made on material explorations in the last few years, yet further improvements on the hydrogen storage properties of these materials are still needed. As a complementary approach to the experimental study, theoretical simulation has played an active role in material designs, which saves the experimental cost and time in synthesizing potential hydrogen storage materials.

Chapter 2

Overview of Density Functional Theory

The theoretical calculations in this thesis are based on the density functional theory (DFT) method, which becomes popular for solving many-electron Schrödinger equations with the development of modern computer technology. In this chapter, we will have a general introduction to the density functional theory. At first, we will have a look at Thomas-Fermi approximation and Hartree-Fock approximation, two commonly used methods trying to deal with many-electron systems before the emergence of DFT. Then Hohenberg-Kohn theorems and Kohn-Sham equations will be stated, they establishing the theoretical basis of DFT. At last, two important approximations for DFT, local density approximation (LDA) and generalized gradient approximation (GGA), as well as the popular hybrid functional B3LYP will be outlined.

2.1 Thomas-Fermi approximation

The first attempt to treat many-electron Schrödinger equations as density functionals can be backdated to the Thomas-Fermi approximation, which is a semiclassical approximation by assuming the uniform distribution of electrons.⁵⁵ For a uniform electron gas, the total number of the electrons N can be expressed as:

$$N = 2 \frac{V}{(2\pi)^3} \int_0^{k_F} 4\pi k^2 dk = \frac{V}{3\pi^2} k_F^3, \quad (2.1)$$

where k_F is the Fermi momentum. Thus, the electron density n can be obtained:

$$n = \frac{N}{V} = \frac{k_F^3}{3\pi^2}. \quad (2.2)$$

The kinetic energy of this N -electron system T is given in a similar form to Eq. (2.1):

$$T = 2 \frac{V}{(2\pi)^3} \int_0^{k_F} \frac{\hbar^2 k^2}{2m} 4\pi k^2 dk = \frac{V \hbar^2}{10m\pi^2} k_F^5. \quad (2.3)$$

By substituting Eq. (2.2) into Eq. (2.3), we can have:

$$T = N \frac{3}{5} \frac{\hbar^2 k_F^2}{2m}. \quad (2.4)$$

If the density locally depends on the position $n(r)$, and assuming the Eq. (2.2) still applies, then the kinetic energy of the system becomes:

$$T[n] = \frac{3\hbar^2}{10m} (3\pi^2)^{2/3} \int n(r)^{5/3} d^3r, \quad (2.5)$$

where the kinetic energy $T[n]$ is a functional, function of function. The kinetic energy T is a function of the density n , and n is a function of the position r , so the kinetic energy is a density functional $T[n]$.

Under the Thomas-Fermi approximation, the external potential and the electron-electron Coulomb interaction of the system can also be expressed as density functionals, thus the many-electron Schrödinger equation becomes a density functional and can be solved with ease. However, since the kinetic energy is approximate and there is not much consideration of the exchange and correlation energy of electrons, Thomas-Fermi approximation is usually used to get qualitative trends and is not suitable to obtain quantitative results for realistic systems.

2.2 Hartree-Fock approximation

The exact electron exchange energy is included in the Hartree-Fock approximation, which assumes the antisymmetric wave function of the N -electron system can be represented by a Slater determinant:^{56, 57}

$$\Psi_{AS}(x_1, \dots, x_N) = \frac{1}{\sqrt{N!}} \begin{vmatrix} \psi_1(x_1) & \psi_1(x_2) & \cdots & \psi_1(x_N) \\ \psi_2(x_1) & \psi_2(x_2) & \cdots & \psi_2(x_N) \\ \vdots & \vdots & & \vdots \\ \psi_N(x_1) & \psi_N(x_2) & \cdots & \psi_N(x_N) \end{vmatrix}, \quad (2.6)$$

where x_i is the spin-orbital coordinate of the i th electron, and ψ_i is the corresponding single electron wave function, satisfying the condition of orthonormality:

$$\int \psi_i^*(x) \psi_j(x) d^3x = \delta_{ij}. \quad (2.7)$$

Under the Born-Oppenheimer approximation,⁵⁸ which assumes the nuclei of the system are static with respect to the electrons since the nuclei are much heavier than the electrons, the Hamiltonian for the electrons in atomic units is as follows:

$$H = \sum_i \left(-\frac{1}{2} \nabla_i^2 - \sum_n \frac{Z_n}{|r_i - R_n|} \right) + \frac{1}{2} \sum_{i,j \neq i} \frac{1}{|r_i - r_j|}, \quad (2.8)$$

where the r_i and R_n denote the positions of the electrons and nuclei respectively, and the Z_n refer to the nuclei charges. Then the expectation value of the energy of the system can be determined as:

$$\begin{aligned} E = \langle \Psi_{AS} | H | \Psi_{AS} \rangle &= \sum_i \int \psi_i^*(x) \left(-\frac{1}{2} \nabla^2 - \sum_n \frac{Z_n}{|r - R_n|} \right) \psi_i(x) d^3x \\ &+ \frac{1}{2} \sum_{i,j \neq i} \iint |\psi_i(x)|^2 \frac{1}{|r - r'|} |\psi_j(x')|^2 d^3x d^3x' \\ &- \frac{1}{2} \sum_{i,j \neq i} \iint \psi_i^*(x) \psi_j^*(x') \frac{1}{|r - r'|} \psi_j(x) \psi_i(x') d^3x d^3x' \end{aligned} \quad (2.9)$$

In Eq. (2.9), the first two terms on the right hand side represent the electron kinetic energy and the external potential generated by static nuclei of the system, respectively. The third term is the electron Coulomb interaction, and the fourth term is called the electron exchange energy, which is due to the antisymmetry of the electron wave function. By using variational principle $\frac{\delta E}{\delta \psi_i^*(x)} = 0$ to Eq. (2.9), we can get the

Hartree-Fock equation:

$$\begin{aligned} &\left[-\frac{1}{2} \nabla^2 - \sum_n \frac{Z_n}{|r - R_n|} + \sum_j \int \frac{1}{|r - r'|} |\psi_j(x')|^2 d^3x' \right] \psi_i(x) \\ &- \sum_j \left[\int \psi_j^*(x') \frac{1}{|r - r'|} \psi_i(x') d^3x' \right] \psi_j(x) = \varepsilon_i \psi_i(x) \end{aligned} \quad (2.10)$$

where ε_i is the Lagrange multiplier. The Hartree-Fock equation can be solved by a self-consistency iterative procedure, so the Hartree-Fock method is also called the self-consistent field method (SCF).

According to Pauli's exclusion principle, two electrons with the same spin may

not occupy the same quantum state simultaneously. Therefore, the two electrons with the parallel spin separate from each other, and this effect has been well taken into account as the electron exchange energy in the Hartree-Fock approximation. For two electrons with opposite spins, since they are in two orthogonal states, they would not produce electron exchange energy. However, two electrons with opposite spins do correlate with each other, and the corresponding electron correlation energy has not been included in the Hartree-Fock approximation.

2.3 Density functional theory

2.3.1 Hohenberg-Kohn theorems

In 1964, Hohenberg and Kohn put forward that the ground state properties of an N -electron system can be uniquely determined by its electron density and the energy of the system is a functional of the density, with the ground state energy corresponding to the ground state density, which are called the Hohenberg-Kohn theorems.⁴⁵

For an N -electron system, the stationary Schrödinger equation is:

$$H\Psi = (T + V + U)\Psi = \left[\sum_i -\frac{1}{2}\nabla_i^2 + \sum_i V(r_i) + \frac{1}{2} \sum_{i,j \neq i} \frac{1}{|r_i - r_j|} \right] \Psi = E\Psi, \quad (2.11)$$

where T is the electron kinetic energy, $V(r)$ is the external potential generated by static nuclei, and U is the electron Coulomb repulsion energy. Then the electron density can be given by:

$$n(r) = \int d^3r_2 \int d^3r_3 \cdots \int d^3r_N |\Psi(r, r_2, \cdots r_N)|^2. \quad (2.12)$$

Since the external potential $V(r)$ is system dependent and different $V(r)$ would result in different ground state wave function Ψ , the $V(r)$ should be uniquely determined by $n(r)$ according to Hohenberg-Kohn theorems. This can be proved as followings.

Suppose there are two $V_1(r)$ and $V_2(r)$ giving the same $n(r)$, and they are associated with different Hamiltonians, ground state wave functions and energies by H_1 and H_2 , Ψ_1 and Ψ_2 , and E_1 and E_2 unless $V_1(r) - V_2(r) = \text{const}$. Then we can have

$$E_1 = \langle \Psi_1 | H_1 | \Psi_1 \rangle < \langle \Psi_2 | H_1 | \Psi_2 \rangle = \langle \Psi_2 | H_2 - V_2 + V_1 | \Psi_2 \rangle, \text{ so we can get}$$

$$E_1 < E_2 + \int d^3r (V_1 - V_2)n(r). \quad (2.13)$$

Similarly, we can also have

$$E_2 < E_1 + \int d^3r (V_2 - V_1)n(r). \quad (2.14)$$

Combining Eq. (2.13) and (2.14), we get the following contradiction:

$$E_1 - E_2 < \int d^3r (V_1 - V_2)n(r) < E_1 - E_2. \quad (2.15)$$

Hence, we prove that the external potential $V(r)$ is a unique functional of the density $n(r)$. Since $V(r)$ determines the Hamiltonian of the system H , which determines the ground state wave function Ψ , the ground state is also a unique functional of the density $\Psi[n]$.

From $E = \langle \Psi[n] | H | \Psi[n] \rangle$, we can see that the energy of the system can also be expressed as a functional of the density:

$$E[n] = T[n] + U[n] + \int d^3r V(r)n(r), \quad (2.16)$$

where the functional $E[n]$ can be minimized to the ground state energy with respect to the density, subject to the constraint $\int d^3r n(r) = N$.

2.3.2 Kohn-Sham equations

By using the density functional to describe the N -electron system, the ground state properties of the system are then only dependent on the electron density with 3 spatial coordinates, which is much simplified compared with the original problem of N electrons with $3N$ degrees of freedom. However, the form of the energy functional $E[n]$ is unknown, so Eq. (2.16) remains to be unsolvable. In 1965, Kohn and Sham developed several equations, which can self-consistently solve the density functional equations of an N -electron system by using an effective potential with the analogue of the noninteracting electron system. These equations are called Kohn-Sham equations.⁴⁶

For the system of N interacting electrons, the corresponding energy functional can be written as:

$$E[n] = T[n] + \int d^3r V(r)n(r) + \frac{1}{2} \iint d^3r d^3r' n(r') \frac{1}{|r-r'|} n(r) + E_{xc}[n], \quad (2.17)$$

where the first term $T[n]$ is the kinetic energy of the noninteracting electron gas, the second term is the external potential energy, the third term is the Hartree energy describing the electron Coulomb repulsion, and the last term is the exchange and correlation energy, which contains all the other energy contributions that are not included in the first three terms. To solve this complex N -electron problem, let us first look at the noninteracting electron system whose energy functional is:

$$E[n] = T[n] + \int d^3r V(r)n(r). \quad (2.18)$$

Using variational principle, we can get

$$\frac{\delta T[n]}{\delta n(r)} + V(r) = \mu n(r), \quad (2.19)$$

where μ is the Lagrange multiplier. We know that the ground state of the noninteracting electron system can be expressed as a Slater determinant, in which the single electron wave functions satisfy:

$$\left[-\frac{1}{2} \nabla^2 + V(r) \right] \psi_i(r) = \varepsilon_i \psi_i(r). \quad (2.20)$$

Then the ground state density of the system is given by:

$$n(r) = \sum_i |\psi_i(r)|^2. \quad (2.21)$$

Now we use variational principle to Eq. (2.17):

$$\frac{\delta T[n]}{\delta n(r)} + V(r) + \int d^3r' n(r') \frac{1}{|r-r'|} + \frac{\delta E_{xc}[n]}{\delta n(r)} = \mu n(r), \quad (2.22)$$

and define the effective potential $V_{eff}(r)$ as:

$$V_{eff}(r) = V(r) + \int d^3r' n(r') \frac{1}{|r-r'|} + \frac{\delta E_{xc}[n]}{\delta n(r)}. \quad (2.23)$$

Then Eq. (2.22) turns to be $\frac{\delta T[n]}{\delta n(r)} + V_{eff}(r) = \mu n(r)$, which has a similar form to that

of Eq. (2.19). The analogue of Eq. (2.20) should be:

$$\left[-\frac{1}{2}\nabla^2 + V_{\text{eff}}(r) \right] \psi_i(r) = \varepsilon_i \psi_i(r), \quad (2.24)$$

where $\psi_i(r)$ still satisfies Eq. (2.21). Now combining Eq. (2.21), (2.23) and (2.24), the electron density $n(r)$ can be obtained iteratively, and the total energy of the N -electron system is given by:

$$E = \sum_i \varepsilon_i - \frac{1}{2} \iint d^3r d^3r' n(r) \frac{1}{|r-r'|} n(r') + E_{\text{xc}}[n] - \int d^3r V_{\text{xc}}[n] n(r), \quad (2.25)$$

where $V_{\text{xc}}[n] = \frac{\delta E_{\text{xc}}[n]}{\delta n(r)}$ is the exchange correlation potential.

Now we arrive at several density functional equations that can be solved by self-consistent iterative method. The problem is the exact form of the exchange correlation potential, which is a density functional, is not known. In order to put the density functional theory in practical use, we have to use some approximations to $V_{\text{xc}}[n]$.

2.3.3 Local density approximation

One of the most commonly used approximations to the exchange correlation density functionals is the local density approximation (LDA), which assumes that the exchange correlation energy only depends on the electron density at r . Under the LDA, the exchange correlation energy can be expressed as:

$$E_{\text{xc}} = \int d^3r \varepsilon_{\text{xc}}[n(r)] n(r), \quad (2.26)$$

where $\varepsilon_{\text{xc}}[n(r)]$ is the exchange correlation energy density of an electron gas at density $n(r)$. LDA is correct for a homogeneous electron gas and works well for systems whose electron densities change slowly.

Furthermore, we can split E_{xc} into exchange energy E_x and correlation energy E_c . A simple form of E_x is usually taken from the calculations for the homogeneous electron gas.⁵⁹

$$E_x \propto \int d^3r n^{4/3}(r), \quad (2.27)$$

and E_c can also be obtained by using quantum Monte Carlo simulations for the homogeneous electron gas at several intermediate densities.⁶⁰ Some other forms of the exchange correlation energy were also reported.⁶¹⁻⁶⁴

The DFT-LDA method has turned out to be very successful in the electronic structure calculations of atoms, molecules and solids. However, the LDA potential has a relatively rapid decay and its prediction to the stability of some anions is poor. Hence, further improvements on the exchange correlation energy are needed.

2.3.4 Generalized gradient approximation

Actually the exchange correlation energy not only depends on the electron density at r but also on the density variations close to r . If we take the gradient of the electron density into account, then the exchange correlation energy can be expressed as:

$$E_{xc} = \int d^3r \epsilon_{xc}[n(r), \nabla n(r)] n(r), \quad (2.28)$$

which is called the generalized gradient approximation (GGA).

Similar to the LDA case, the exchange correlation energy E_{xc} can also be divided into two parts: exchange energy E_x and correlation energy E_c , with each part treated individually under the GGA. There are several well known exchange correlation functionals that have been developed under the GGA scheme, such as B88,⁶⁵ LYP,⁶⁶ PW91⁶⁷ and PBE.⁶⁸

More accurate results for the N -electron system can be obtained by GGA than by LDA. However, the exchange energy formulated under DFT is not exact. The Coulomb couplings between an electron and its own charge distribution result in the overestimation of the electron Coulomb repulsion, thus this electron self interaction should be cancelled in the Hartree energy, the third term in Eq. (2.17). To solve this problem, the hybrid functionals have been developed to improve the DFT results.

2.3.5 Hybrid functional B3LYP

Since the electron exchange energy is exact under the Hartree-Fock approximation, by combining the exchange energy from Hartree-Fock method and the exchange correlation energy from the density functional theory, a hybrid functional of the exchange correlation energy was introduced by Becke to solve the N -electron problems.⁶⁹ The exchange correlation energy has a form like:

$$E_{xc} = \frac{1}{2}E_x^{HF} + \frac{1}{2}E_{xc}^{LSDA}, \quad (2.29)$$

where E_x^{HF} is the Hartree-Fock based exact exchange energy, and E_{xc}^{LSDA} is the DFT-based exchange correlation potential energy under the local spin-density approximation (LSDA). Enlightened by this hybridization scheme, various exchange and correlation functionals can be combined with E_x^{HF} to construct a hybrid exchange correlation functional. For example, the widely used hybrid functional B3LYP has a form as follows:⁷⁰

$$E_{xc}^{B3LYP} = (1-a_0)E_x^{LSDA} + a_0E_x^{HF} + a_xE_x^{B88} + a_cE_c^{LYP} + (1-a_c)E_c^{VWN}, \quad (2.30)$$

where $a_0 = 0.2$, $a_x = 0.72$, and $a_c = 0.81$, which are obtained by a linear least-squares fitting.⁷¹ It can be seen that both exchange and correlation energy functionals under LDA (E_x^{LSDA} , E_c^{VWN}) and GGA (E_x^{B88} , E_c^{LYP}) are used to combine with E_x^{HF} for constructing the B3LYP hybrid functional.

2.4 Summary

Combining with the modern computer technology, density functional theory method has become a powerful tool in solving many-electron problems related to atoms, molecules and solids. Nowadays, many computer programs based on DFT, such as CASTEP,⁷² DMol³,^{73, 74} Gaussian⁷⁵ and VASP,^{76, 77} have been developed for theoretical simulations, which make great contributions in various research fields.

Chapter 3

DFT Study of Hydrogen Storage by Spillover on Graphene with Boron Substitution

From this chapter on, I am going to use four chapters to elaborate my theoretical investigations on the hydrogen spillover by first-principles calculations. The hydrogen spillover mechanism on B-doped graphene and N-doped graphene will be discussed in Chapter 3 and Chapter 4, respectively. We will see how doping B/N helps in lowering the H migration barrier from metal to substrate and thus improves the hydrogen storage property of the graphitic surface. As an analogue to B/N-doped graphene, C-doped boron nitride (BN) sheet is also selected as a substrate for hydrogen spillover study. The possibility of hydrogen spillover on BN sheet will be addressed in Chapter 5. Following Chapter 5, to further understand the kinetic issues on the BN-based materials for hydrogen storage, C-doped BN nanocages are proposed as potential candidates for hydrogen storage materials, and how the size or curvature of the BN fullerene influences on the H₂ dissociation barrier is going to be illustrated in Chapter 6.

3.1 Introduction

As we have known from Chapter 1 that hydrogen spillover has been proposed as an effective approach for hydrogen storage at ambient temperature.⁷⁸ However, to fulfill the requirements for hydrogen storage materials, further improvement of hydrogen storage properties of carbon materials is still needed, where a deep understanding of the hydrogen spillover process is of great importance. In this aspect, theoretical calculation can play a leading role and provide helpful information. Cheng *et al.* have studied the dissociation of molecular hydrogen on the Pt₆ cluster, and by approaching the fully saturated Pt₆ cluster toward the graphene sheet, they proposed a migration of two H atoms from metal to graphene, with an average activation barrier of 0.48 eV per H atom; however, thermodynamically, the migration process is

endothermic.⁷⁹ Further investigation by Froudakis *et al.* about hydrogen spillover on Pt-doped graphite, which is the real case in experiments in which metal clusters are supported on the substrate, showed a rather higher migration barrier of 2.6 eV for H atom diffusing from a fully saturated Pt₄ cluster to the supporting graphitic surface.⁸⁰ Yakobson *et al.* also pointed out that it is difficult for a pristine graphene to attract the H atom down from the saturated metal catalyst, due to the weak C-H binding strength for the pristine graphene, which greatly inhibits the spillover process at ambient temperature.⁸¹ So, how to improve the C-H binding or the hydrogen adsorption strength on the graphitic surface naturally becomes one of the crucial points in the hydrogen spillover research.

Recently, enhanced hydrogen adsorption was reported on boron-substituted carbon.^{82, 83} Experimental synthesis of B-doped carbon materials and their applications for hydrogen storage were also carried out.^{84, 85} Yang's group studied hydrogen storage via spillover on Ru-supported B- and N-doped microporous carbon, and 2.2-fold enhanced hydrogen uptake of 1.2 wt % at 298 K and 10 MPa was obtained.⁸⁶ All the information gives a strong indication that B-doping could be an effective approach in the modification of carbon materials for hydrogen storage applications. Despite the experimental observation of enhanced hydrogen storage capacity of B-doped carbon materials with spillover method, the whole picture about the spillover mechanism, such as how the metal catalyst interacts with the B-doped carbon substrate and dissociates H₂ molecules, how the migration process for H atoms from metal to substrate takes place, and what the diffusion behavior of H atoms looks like in the vicinity of the hydrogenated metal on the substrate, is not yet well-understood.

In the present work, DFT calculations have been conducted to investigate the hydrogen spillover process on B-doped graphene in detail, which should be a potential candidate for hydrogen storage materials. In the simulation, the Pt₄ cluster with tetrahedral geometry is chosen as a model to represent metal catalyst, which can effectively dissociate H₂ molecules and efficiently describe such kind of interactions.⁸⁰ We first dope only one B atom in the graphene sheet and find that the

Pt₄ cluster is more strongly bound to the B-doped graphene compared with the undoped case. Then by putting H₂ molecules around the supported Pt₄ cluster, geometry optimization yields a saturated Pt₄ cluster with 14 H atoms, while Pt₄ supported by pure graphene can only adsorb 10 H atoms without detaching from the substrate. Second, we estimate the activation barrier for one H atom migrating from Pt₄ to B-doped graphene, and a much lowered migration barrier is obtained due to the enhanced C-H binding strength around the B atom. Finally, we investigate the hydrogen spillover on the BC₃ sheet with a similar procedure as described above. The uniform B-C network presents sufficiently low activation barriers for both migration and diffusion of H atoms on the BC₃ substrate. The thermodynamic issues of hydrogen spillover on B-doped graphene are also addressed in the end.

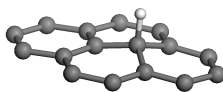
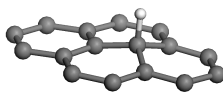
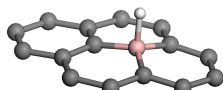
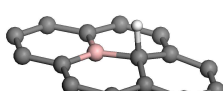
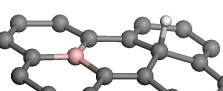
3.2 Computational methods

All calculations have been carried out using the DMol³ program^{73, 74} based on DFT with GGA-PBE⁶⁸ for exchange and correlation potential. We used DFT semicore pseudopotential with double numerical basis set plus polarization functions (DNP), which is comparable with the Gaussian 6-31G(d,p) basis set in size and quality. A (6×6) supercell with periodic boundary conditions on the *x-y* plane was employed to model the infinite graphene sheet. The vacuum space was set with 20 Å in the *z* direction to avoid the interactions between periodic images. For BC₃ substrate, since its primitive cell is about twice the size of graphene's, a (3×3) supercell was used for the modelling. A 3×3×1 mesh of *k*-points⁸⁷ and the global orbital cutoff of 5.0 Å have been used in the spin-unrestricted calculations. All structures were relaxed without any symmetry constraints. Convergence in energy, force and displacement was set as 10⁻⁵ Ha, 0.001 Ha/Å, and 0.005 Å, respectively. All transition states were located via complete LST/QST method⁸⁸ as implemented in DMol³ package and verified by vibrational frequency analysis. The in-plane lattice parameter of the graphene sheet has been optimized to be 2.469 Å, which is close to the ideal value of 2.46 Å. For the BC₃ substrate, the optimized in-plane lattice parameter is 5.178 Å, in good agreement with the value of 5.168 Å calculated by Ferro *et al.*⁸²

3.3 Results and discussion

3.3.1 Adsorption of H on pure graphene and 1B-doped graphene sheet

Table 3.1 Calculated hydrogen adsorption energy (ΔE_H), the corresponding H-bond length (d_{C-H}/d_{B-H}), and the Hirshfeld charges of B and H-bond related atoms, for the hydrogenation on pure graphene (G) and 1B-doped graphene sheet (G_B).^a

G-H/ G_B -H		ΔE_H (eV)	d_{C-H}/d_{B-H} (Å)	Hirshfeld charge		
				B	C	H
G-H		-1.009 (1.263)	1.124		-0.019	0.060
G_B -B-H		-1.600 (0.672)	1.259	-0.063		0.020
G_B -C-H- <i>ortho</i>		-1.933 (0.339)	1.132	0.066	-0.075	0.089
G_B -C-H- <i>para</i>		-1.646 (0.626)	1.121	0.046	-0.011	0.075

^a The value of ΔE_H that is calculated with reference to $1/2 E_{H_2}$ is also listed in parentheses. The three lowest-energy structures for hydrogenated G_B sheet, as well as the optimized structure for hydrogenated graphene, are illustrated by side views. For clarity, only the hydrogenation regions are drawn as schematic diagrams (H, white; B, pink; C, grey).

The influence of boron doping on the hydrogenation of graphene sheet was investigated. Table 3.1 shows the calculated adsorption energy of a single H atom on pure graphene (G) and on different sites of one B atom doped graphene sheet (G_B), the corresponding H-bond length, and the Hirshfeld charges⁸⁹ of relevant atoms. The schematic diagram of each stable structure obtained after optimization is shown. For clarity, only the substrate regions involving hydrogen or Pt₄ cluster are drawn in the schematic diagrams in this thesis, unless stated otherwise. The isosurface of deformation electron density and Hirshfeld charge distribution for each structure in

Table 3.1 is illustrated in Figure 3.1 to assist our analysis. The adsorption energy of H atom (ΔE_H) on G/G_B sheet is calculated as:

$$\Delta E_H = E_{\text{Sub-H}} - E_{\text{Sub}} - E_H, \quad (3.1)$$

where E_{Sub} , E_H , and $E_{\text{Sub-H}}$ represent the energies of the substrate (G or G_B sheet), a single H atom, and the hydrogenated substrate, respectively. Optionally, ΔE_H can also be calculated with reference to the half energy of a H₂ molecule $1/2 E_{\text{H}_2}$, instead of E_H in Eq. (3.1). Thus, both values of ΔE_H with different reference energy are listed in Table 3.1 for comparison. The adsorption energy for H atom directly adsorbed on B atom in G_B sheet (G_B-B-H) is -1.600 eV, which is almost 60% enhanced hydrogenation strength with respect to that of -1.009 eV for hydrogenated graphene (G-H). In addition, we also find that when the H atom is adsorbed on the C atom next to (G_B-C-H-*ortho*) or opposite to (G_B-C-H-*para*) the B atom in the same hexagonal ring, the adsorption strength is even stronger, with $\Delta E_H = -1.933$ eV and $\Delta E_H = -1.646$ eV, respectively. This is in good agreement with Yang *et al.*'s experimental results that doped carbon is favorable for H adsorption.⁸⁶

When using $1/2 E_{\text{H}_2}$ as the reference energy, all the calculated values of ΔE_H are positive, 2.272 eV bigger than their counterparts, as shown in the parentheses of Table 3.1. On one hand, the positive hydrogenation energy indicates that it is hard for the supporting G/G_B sheet to dissociate the H₂ molecule directly. This is the reason why the metal catalyst is used in the hydrogen spillover process, which will be addressed in detail in the following. On the other hand, the energy difference between ΔE_H of each structure in Table 3.1 is independent of the choice of energy reference. Since the hydrogen spillover process is related to the H atom diffusion behavior on the supporting substrate, we think it is more evident and convenient in formulating the H spillover mechanism by taking E_H as the reference energy. In Ref. 20, Froudakis *et al.* also used E_H as the reference energy in their H spillover study.

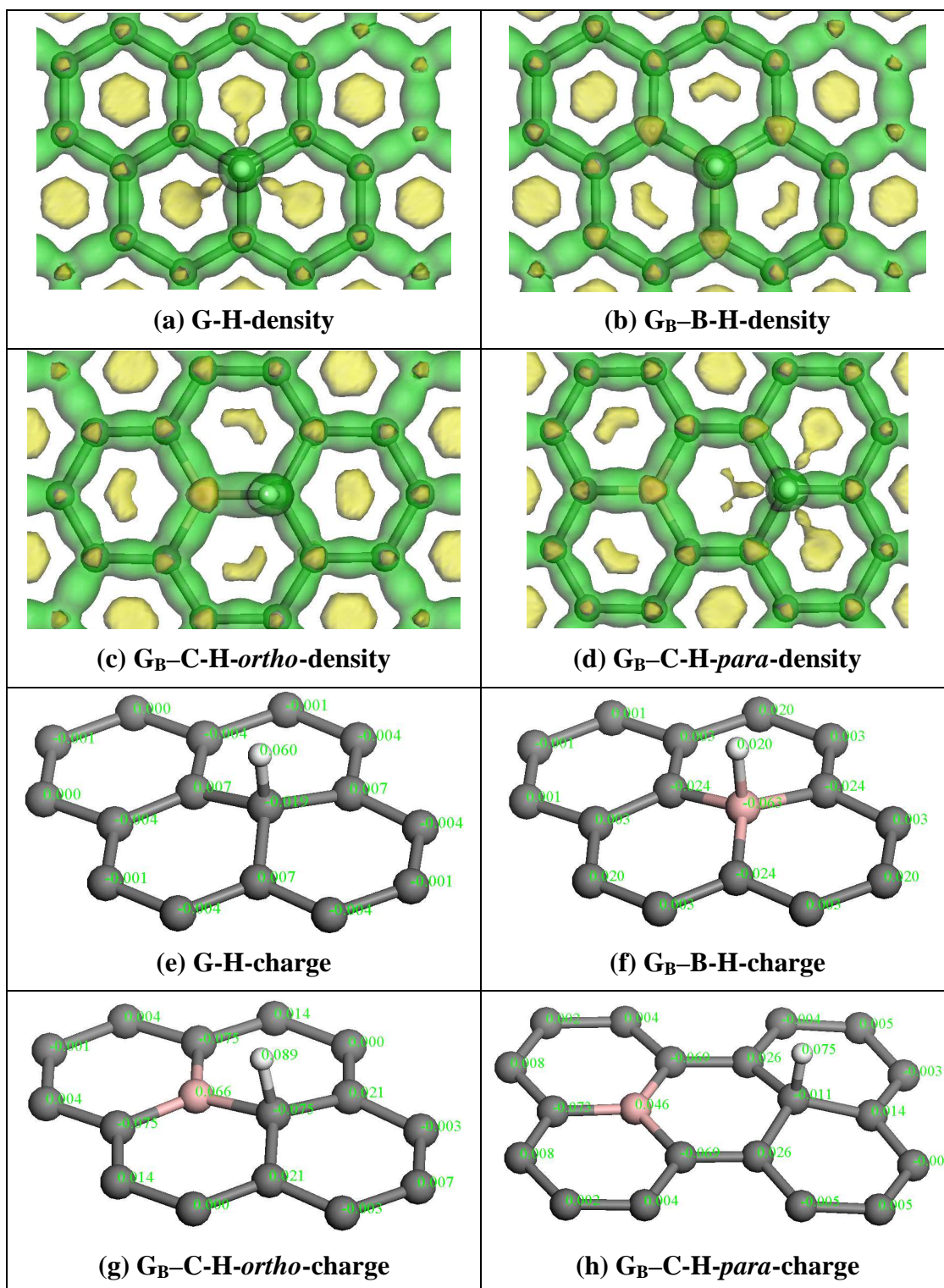


Figure 3.1 (a-d) Deformation electron density isosurfaces of the four hydrogenated structures in Table 3.1 illustrated by top views (green, electron accumulation; yellow, electron depletion); (e-h) Hirshfeld charge distributions of the four hydrogenated structures in Table 3.1 illustrated by side views (H, white; B, pink; C, grey).

From the isosurface of deformation electron density, which is calculated by

subtracting the electron density of the isolated atoms from the total electron density, it can be found that the electrons accumulate (green regions) between in-plane atoms to form covalent bonds on the substrate (Figure 3.1a-d). Upon the hydrogenation, the in-plane π -electrons move upward to form a C-H bond, which results in a small depletion of electron (yellow regions) around the hydrogenated C atom (Figure 3.1a). Interestingly, the three depletion areas surrounding the B atom, as shown in Figure 3.1b, are even smaller and there is a relatively big accumulation area of electron around B. This can be attributed to that boron has one less valence electron than carbon, and the doped B acts as an electron-acceptor, trapping electrons from the nearby regions. This also results in a Hirshfeld charge of -0.063 for the B atom, indicating a strong B-H bond is formed (G_B -B-H). In addition, the C atom adjacent to B is also affected by the electron clouds around B, which leads to an enhanced C-H bonding, with a Hirshfeld charge of -0.075 for the hydrogenated C (G_B -C-H-*ortho*). Actually, the H atom in G_B -C-H-*ortho* structure is not vertically bound on the top of C but leans toward the B atom, resulting in an elongated C-H bond length of 1.132 Å. Therefore, the hydrogen adsorption is considered to be cooperatively strengthened by boron and carbon. Apparently, boron atom acts as an effective electron accumulation center in the graphene sheet, where either B atom or its adjacent C atoms have relatively large values in terms of Hirshfeld charge (Figure 3.1f-h), compared with the undoped graphene case (Figure 3.1e). Hence, it is possible that hydrogenation is more thermodynamically favored due to the enhanced interaction between the electron of H and the π -cloud of the G_B sheet. To summarize, the DFT calculations suggest that B doping can greatly enhance the surface hydrogenation strength of graphene, and the C atom adjacent to B is the most favorable site for hydrogen adsorption.

3.3.2 Hydrogen adsorption on Pt₄ cluster supported by G or G_B sheet

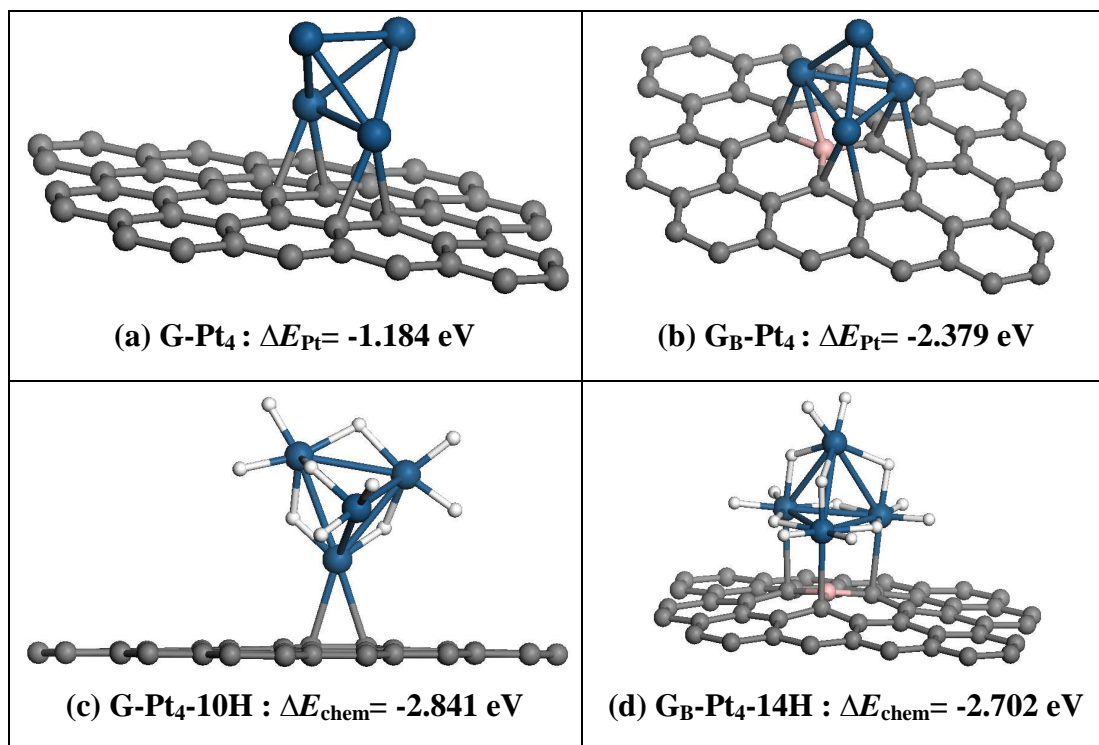


Figure 3.2 Optimized structures of (a) Pt₄ cluster on pure graphene (G-Pt₄), (b) Pt₄ cluster on G_B sheet (G_B-Pt₄), (c) saturated Pt₄ cluster on graphene with 10 H atoms chemisorbed (G-Pt₄-10H), and (d) saturated Pt₄ cluster on G_B sheet with 14 H atoms chemisorbed (G_B-Pt₄-14H) (H, white; B, pink; C, grey; Pt, cyan). The binding strength of Pt₄ $|\Delta E_{Pt}|$ on G_B sheet is 2.379 eV, much stronger than that of 1.184 eV on graphene. The chemisorption energy per H atom ΔE_{chem} for the saturated Pt₄ cluster on G and G_B sheet is -2.841 eV and -2.702 eV, respectively, indicating a strong H₂ dissociation ability for the metal cluster.

The tetrahedral Pt₄ cluster is chosen as the representative catalyst to study the H₂ dissociative chemisorption on metal cluster. Since the chemisorption and desorption properties of H at full coverage are almost independent of cluster size,⁹⁰ a small Pt₄ cluster can provide us with a relatively large supercell to simulate the H diffusion process on the substrate, without losing accuracy and efficiency. To find the most stable structure for Pt₄ adsorbed on the supporting substrate, we tried different initial configurations by putting Pt₄ above C (B) site, C-C (C-B) bond, or hollow site of the hexagonal ring. As shown in Figure 3.2a, the Pt₄ cluster is attached to the graphene sheet (G-Pt₄) with two Pt atoms above the C-C bonds after the optimization. The

adsorption energy of Pt₄ on graphene ΔE_{Pt} is calculated to be -1.184 eV. Similarly, Pt atoms also interact with the C-C and C-B bonds to form a stable structure on G_B sheet (Figure 3.2b, G_B-Pt₄), where three Pt atoms are attached on the substrate. The corresponding adsorption strength $|\Delta E_{Pt}|$ for Pt₄ on G_B is about 2.379 eV, much stronger than that for G-Pt₄. Combining with what we have learned from the hydrogenation reaction on the G/G_B sheet, we can conclude that B-doping not only improves the hydrogen adsorption ability, but also enhances the metal binding strength for graphene sheet.

To simulate the H₂ dissociation process and model the H saturation on Pt₄ cluster, initially eight H₂ molecules are put around the metal cluster at various locations for G-Pt₄ or G_B-Pt₄. While sequential H₂ adsorption behavior on the metal cluster may be of interest to some researchers in the field, it is not within the scope of this work. Without losing the contact between Pt₄ and the supporting substrate after the optimization, there are totally 10 H and 14 H atoms fully chemisorbed on Pt₄ for G (G-Pt₄-10H) and G_B sheet (G_B-Pt₄-14H), respectively.¹ H₂ molecules spontaneously dissociate onto the Pt₄ cluster; i.e., a barrierless H₂ dissociation process takes place, which was also reported in Ref. 20. As shown in Figure 3.2c, the Pt₄ cluster is saturated with 10 H atoms, with only one Pt above the C-C bond of graphene. The average chemisorption energy per H atom ΔE_{chem} on Pt₄ is calculated by:

$$\Delta E_{chem} = \frac{1}{n} \left(E_{H_nPt@Sub} - E_{Pt@Sub} - nE_H \right), \quad (3.2)$$

where $E_{Pt@Sub}$, $E_{H_nPt@Sub}$, and n represent the energies of Pt₄ cluster with the substrate,

¹ Close contact between the Pt₄ cluster and the G or G_B sheet can provide a steady H flow from the metal cluster to the supporting substrate; otherwise, the long distance between the chemisorbed H atom and the surface C atom will definitely increase the hydrogen migration barrier from metal to substrate, thus weakening the hydrogen spillover effect. For G_B-Pt₄, seven H₂ molecules are fully dissociated onto the Pt₄ cluster, with only one H₂ departing away after optimization. However, the Pt₄ cluster will detach from the undoped graphene sheet, when eight H₂ molecules are initially put around the metal cluster. Therefore, we gradually decrease the number of H₂ put around the Pt₄ in the initial arrangement and reoptimize the structure until we get a saturated Pt₄ without flying away from the substrate. Different initial positions of H₂ molecules have been considered, and the optimized structure with the lowest energy has been selected as the saturation state.

H-saturated Pt₄ cluster with the substrate, and the number of H atoms chemisorbed on Pt₄, respectively. The ΔE_{chem} is estimated to be -2.841 eV for undoped graphene, with respect to the energy of a single H atom. It is evident that the Pt₄ cluster has a tendency to detach and leaves only one Pt atom in direct contact with the graphene surface upon hydrogenation, which also indicates a weak interaction between Pt₄ and graphene sheet. In contrast, Pt₄ cluster on G_B sheet can fully chemisorb 14 H atoms with $\Delta E_{\text{chem}}=-2.702$ eV, where the three Pt atoms still bind to the underlying substrate (Figure 3.2d). Obviously, more hydrogen can be dissociated via the metal cluster on B-doped graphene than that in the pure graphene case. In addition, B-doping can also stabilize the Pt₄ cluster upon hydrogenation, where saturated Pt₄ serves as a stable H source for the subsequent hydrogen migration process.

3.3.3 H migration from Pt₄ cluster onto the supporting G/G_B sheet

A key step for the hydrogen spillover to take place is how the H atoms migrate onto the supporting substrate from the metal cluster and whether the migration barrier is low enough to gain fast kinetics at room temperature. As shown in Figure 3.3, by dragging one H atom from the starting reactant (R) to the top of a C atom in the substrate, we carried out geometry optimization subsequently to get the final product (P). Then the transition state (TS) was searched by using complete LST/QST method⁸⁸, followed by vibrational frequency calculation for further confirmation. For clarity, the red arrow is used to depict the H migration direction, pointing to the closest and unoccupied C atom on the substrate.

For the undoped graphene, in which the H atom is manually put on a C atom of graphene, we found the H atom migrates back to the Pt₄ cluster after the optimization, which means that it only forms a metastable state for the hydrogenation due to the presence of Pt₄ cluster (see P(G) in Figure 3.3). In this case, we thus used the constrained geometry optimization to estimate the H migration barrier, by gradually changing the Pt-H bond distance. The calculated activation barrier $E_a(\text{G})$ for H migrating to graphene is about 2.721 eV, which is close to the reported value of 2.6 eV calculated by a different DFT functional and software package.⁸⁰ This comparison

also validates the accuracy and reliability of our computational methods. The corresponding transition state TS(G), as illustrated in Figure 3.3, has the H atom away from saturated Pt₄ with a Pt-H distance about 2.7 Å. There is also no C-H bond formed in TS(G), indicating an unrealistic migration process for undoped graphene. The migration reaction is actually an endothermic process, and the reaction energy $E_m(G)$ is around 2.198 eV with respect to the energy of initial state R(G). Both the high values of $E_a(G)$ and $E_m(G)$ prohibit the H migration at ambient conditions for graphene.

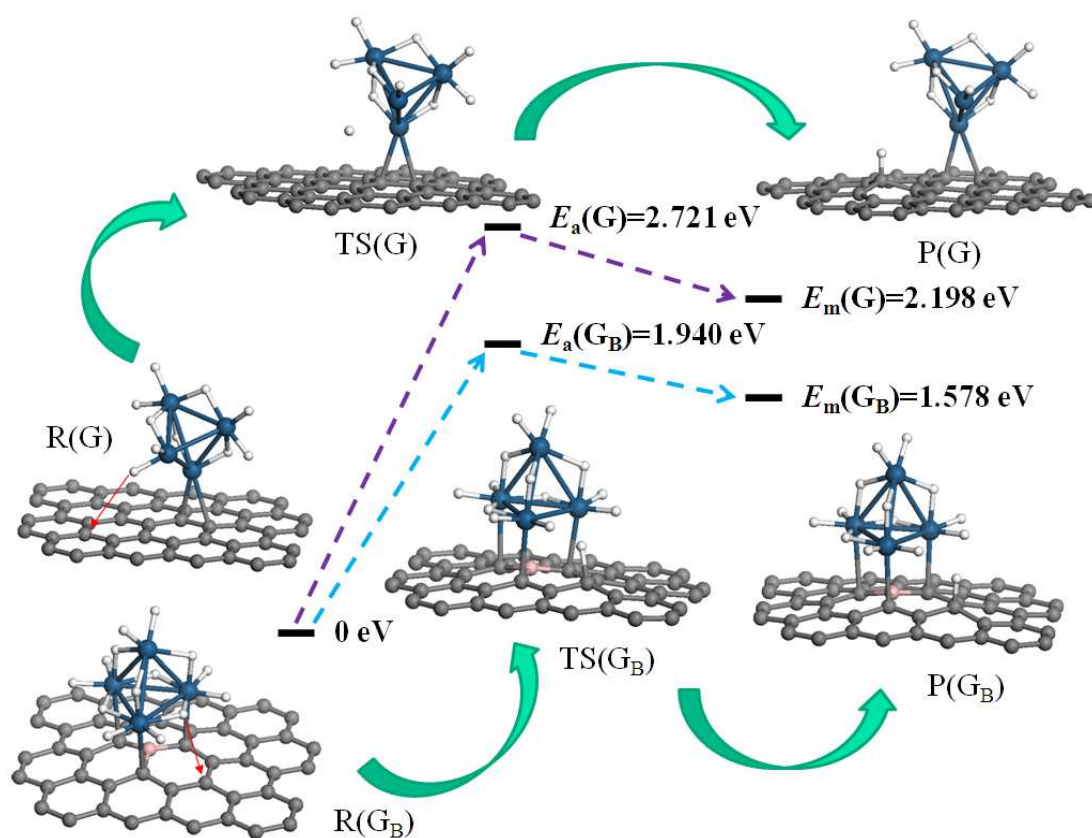


Figure 3.3 Optimized structures of initial (R), transition (TS), and final (P) states for the H migration process from saturated Pt₄ cluster to the supporting G/G_B substrate. The black bars denote the relative energy levels of these structures, with the corresponding schematic diagrams (H, white; B, pink; C, grey; Pt, cyan) drawn above or below. The calculated activation energy E_a for the H migration from Pt₄ to G and G_B sheet is 2.721 eV and 1.940 eV, respectively. The purple and blue dashed arrows are respectively used to guide the eyes for the two separate migration reactions on G and G_B substrates. The reaction energy of the migration E_m with respect to the initial state is estimated to be 2.198 eV and 1.578 eV, respectively, for the G and G_B cases.

For the saturated Pt₄ cluster on G_B sheet (see R(G_B) in Figure 3.3), the H atom is either adsorbed on Pt (corner site) or on a Pt-Pt bond (bridge site). When we dragged one H atom from the corner site onto the C atom in the substrate, the H atom would rebind to the corner site of Pt₄ cluster after optimization. Only H from the bridge site could form a stable state, binding on top of the C opposite to B in the hexagonal ring, with a C-H bond length of 1.134 Å (see P(G_B) in Figure 3.3). On one hand, H atoms are weakly bound to the bridge sites compared with those bound on the corner sites.⁹⁰ Therefore, the H migration from the bridge site is more likely to take place. On the other hand, from our discussions about H adsorption on G_B sheet, the C atom opposite to B becomes a favorable site to adsorb H with $\Delta E_{\text{H}} = -1.646$ eV (see Table 3.1), since all the three C atoms adjacent to B are occupied by Pt atoms for R(G_B). The transition state TS(G_B), as shown in Figure 3.3, has an activation energy $E_{\text{a}}(\text{G}_{\text{B}}) = 1.940$ eV for the H migration, with a C-H bond distance of 1.391 Å. The calculated imaginary frequency of TS(G_B) is about -1301.1 cm⁻¹. The corresponding reaction energy $E_{\text{m}}(\text{G}_{\text{B}})$ is about 1.578 eV with respect to the energy of R(G_B). Both the activation and reaction energies have been lowered by almost 30% for the H migration on G_B sheet compared with the undoped graphene case. B-doping not only enhances the H adsorption strength $|\Delta E_{\text{H}}|$ of the substrate but also leads to averagely weakened H chemisorption strength $|\Delta E_{\text{chem}}|$ on saturated Pt₄ cluster. This eventually results in an improved thermodynamical migration reaction, accompanied by a substantially lowered activation barrier. However, the H migration is still the rate-limiting step, with an activation energy of around 2 eV for G_B sheet; hence, further modification on the graphene is desired to facilitate the hydrogen spillover at ambient conditions.

3.3.4 Hydrogen spillover on BC₃ sheet

Capacity for H in graphitic materials has been experimentally observed to increase with boron concentration.⁹¹ Kouvetakis *et al.* have synthesized the graphite-like BC₃ compound containing 25% of boron.⁹² Theoretical studies have suggested that bulk BC₃ could be a potential candidate for hydrogen storage

material.^{93, 94} The adsorption and recombination mechanism of hydrogen on the BC₃ sheet has also been investigated, where both better H retention capability and easier recombination into H₂ were reported.⁸² Evidently, by increasing the boron doping content in graphene, further improvement on hydrogen spillover and more hydrogen uptake on the substrate are expected. Therefore, as a high B content model of B-doped graphene, BC₃ sheet is a good substrate for studying the H spillover effect, which would be helpful in further understanding the H spillover mechanism on B-doped graphene.

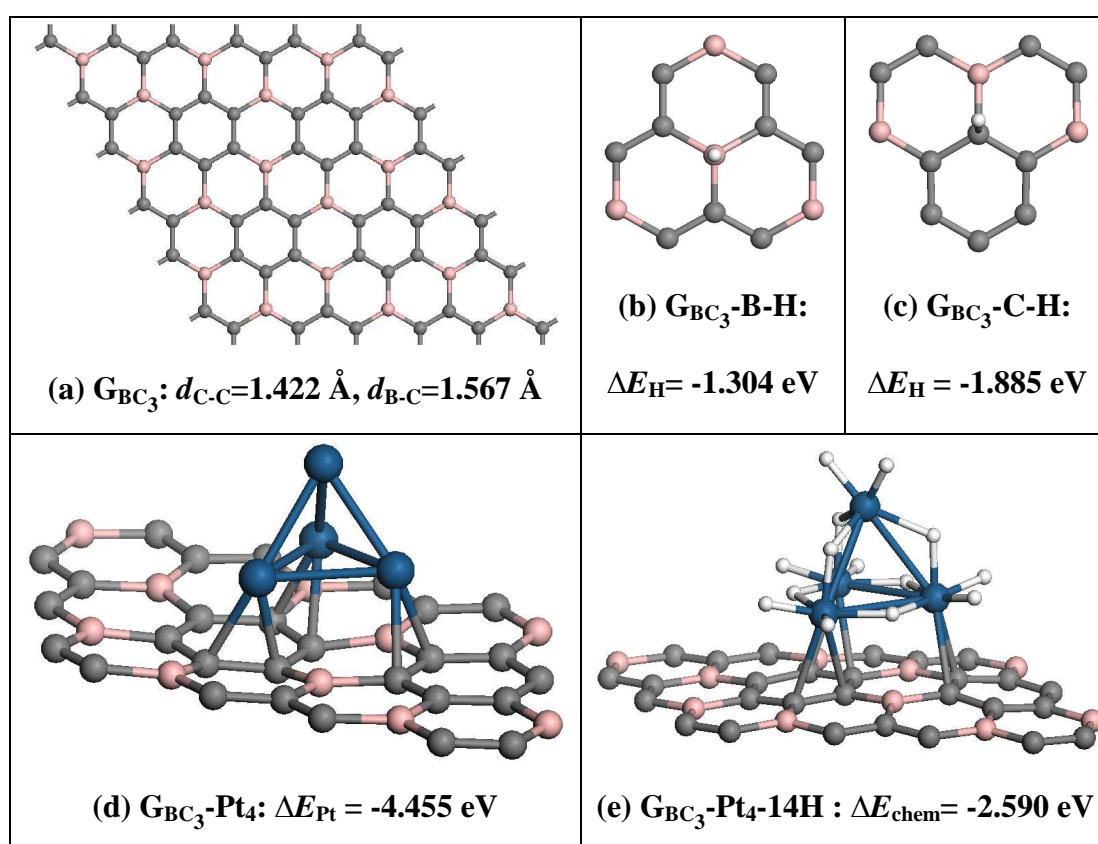


Figure 3.4 Optimized structures of (a) BC₃ sheet (G_{BC₃}), (b) H adsorption on B in G_{BC₃} (G_{BC₃}-B-H), (c) H adsorption on C in G_{BC₃} (G_{BC₃}-C-H), (d) Pt₄ cluster on G_{BC₃} (G_{BC₃}-Pt₄), and (e) saturated Pt₄ cluster on G_{BC₃} with 14 H atoms chemisorbed (G_{BC₃}-Pt₄-14H) (H, white; B, pink; C, grey; Pt, cyan). A (3×3) supercell was used for modelling the BC₃ substrate. The optimized bond length of C-C (d_{C-C}) and B-C (d_{B-C}) for G_{BC₃} is 1.422 Å and 1.567 Å, respectively.

We used a (3×3) supercell for modelling the BC₃ sheet (G_{BC₃}), which is a high symmetry substrate with the optimized C-C and B-C bond length of 1.422 Å and 1.567 Å, respectively (Figure 3.4a). The high symmetry configuration of BC₃ substrate used here is the most stable structure for BC₃ sheet, which was also commonly used by other groups in modelling BC₃ surface.^{21,36,37} The H atom can be adsorbed on either B (Figure 3.4b, G_{BC₃}-B-H) or C atom (Figure 3.4c, G_{BC₃}-C-H) in G_{BC₃} to form a stable state. Similar to the G_B case, H is more favorably bound on C (G_{BC₃}-C-H) with an adsorption energy $\Delta E_H = -1.885$ eV, compared with $\Delta E_H = -1.304$ eV for G_{BC₃}-B-H. A similar procedure to that used in the G/G_B case has been implemented for finding stable structures of Pt₄ and H-saturated Pt₄ cluster on the BC₃ sheet. As shown in Figure 3.4d, the Pt₄ cluster is firmly bound on G_{BC₃} with three C-C bonds (G_{BC₃}-Pt₄), and the adsorption strength $|\Delta E_{Pt}|$ is about 4.455 eV, much stronger than that for G_B-Pt₄. Same as G_B-Pt₄-14H, the catalytic metal can accommodate up to a total of seven dissociated H₂ molecules. The 14 H atoms can bind to the corner or bridge sites of the cluster (Figure 3.4e, G_{BC₃}-Pt₄-14H). The average chemisorption strength per H atom $|\Delta E_{chem}|$ for G_{BC₃}-Pt₄-14H was estimated to be 2.590 eV, which is weaker than that for G_B-Pt₄-14H.

For the BC₃ sheet, we investigated the H migration process from the catalytic metal to the supporting substrate, as well as the H diffusion behavior along the C-C and C-B-C paths on G_{BC₃}. The reaction diagram of each migration/diffusion process is plotted in Figure 3.5, together with the top views of the critical structures involved in these reactions. Figure 3.5a shows the schematic energy profile along the reaction coordinate for H migrating from Pt-Pt bond to C on the BC₃ sheet. A sufficiently lowered activation barrier E_a of 0.648 eV has been obtained for H migration from Pt₄ to G_{BC₃}. A fast kinetics for H migration thus can be achieved under ambient

conditions. However, the migration process remains thermodynamically unfavored, where the energy of final state (FS1) is about 0.639 eV with respect to that of initial state (IS), only 9 meV lower than that of transition state (TS1), whose imaginary frequency is around -754.0 cm^{-1} . The C-H bond length is 1.457 \AA and 1.280 \AA for TS1 and FS1, respectively.

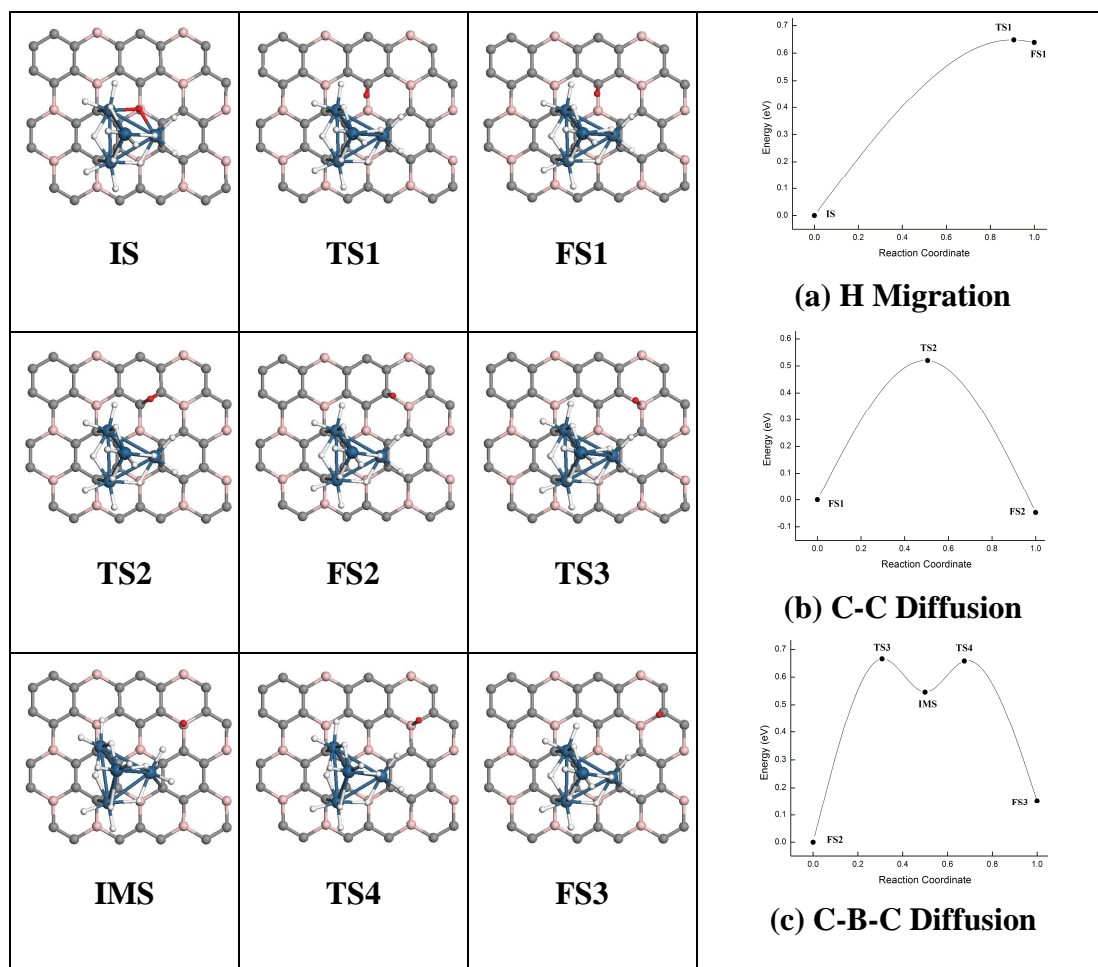


Figure 3.5 Calculated reaction diagrams of (a) H migration from saturated Pt₄ to C on the BC₃ sheet, (b) H diffusion along the C-C path on G_{BC₃}, and (c) H diffusion along the C-B-C path on G_{BC₃}. The schematic diagrams of initial (IS), transition (TS), intermediate (IMS), and final (FS) states involved in the reactions are illustrated by top views (H, white; B, pink; C, grey; Pt, cyan). The reactive H atom is highlighted by red. The lines that link critical points are used to guide the eyes. The energy of reactant in each reaction diagram is set to be zero.

Further diffusion of H atom away from the vicinity of the catalytic metal, can

make full use of surface sites of the substrate for hydrogen storage applications. For the BC_3 sheet, two distinct diffusion paths were investigated following the H migration process. The H atom first diffuses from FS1 to FS2 along the C-C path, as shown in Figure 3.5b, and undergoes an activation barrier of 0.52 eV. The corresponding transition state (TS2) has an imaginary frequency of -742.9 cm^{-1} . The diffusion reaction along the C-C path is exothermic, with the reaction energy being -0.047 eV with respect to the energy of FS1. Then, H further diffuses from FS2 to FS3 via the C-B-C path. It turns out to be a little endothermic, and the energy of FS3 is about 0.153 eV larger than that of FS2, as seen in Figure 3.5c. The B atom adsorbs H and forms an intermediate state (IMS) in the middle of the C-B-C path, where two transition states (TS3, TS4) close to IMS are located, with the energy of TS3(TS4) being around 0.66 eV higher than that of FS2. The imaginary frequencies of TS3 and TS4 are calculated to be -773.1 cm^{-1} and -740.8 cm^{-1} , respectively. Both activation barriers are sufficiently low for H diffusion along the C-C and C-B-C paths, indicating that a fast H diffusion on the substrate can be achieved under ambient conditions.

Combining the data obtained for G, G_B , and G_{BC_3} cases, we find a strong dependence of H migration energy E_m on the hydrogenation strength $|\Delta E_\text{H}|$ of the substrate. As shown in Figure 3.6, from G to G_{BC_3} the reaction energy E_m for H migration decreases as the H adsorption strength $|\Delta E_\text{H}|$ of the supporting sheet increases; i.e., there is a downward trend of ΔE_H toward the binding energy of H_2 molecule per H atom $E_{\text{H-bind}} = -2.272 \text{ eV}$. In contrast, the average H chemisorption energy ΔE_chem exhibits an upward though not obvious trend toward $\Delta E_{\text{H-bind}}$ on the energy profile. The energy difference between ΔE_H and ΔE_chem is reduced to 0.705 eV for the G_{BC_3} sheet, compared with that of 1.832 eV for the undoped graphene. The decreased energy difference surely draws closer the energies of initial and final states involved in the H migration reaction, thus resulting in an improved thermodynamical H migration process. Noticeably seen from Figure 3.6, since ΔE_H is higher than $E_{\text{H-bind}}$ on the energy profile, it is hard for the substrate to chemisorb H atoms directly from

H₂ gas. The reported activation barrier for direct H₂ dissociation on the BC₃ sheet was about 1.2 eV,²¹ much higher than our calculated H migration barrier of 0.648 eV from Pt₄ to G_{BC₃}. Thus, the metal cluster not only plays the catalytic role in dissociating H₂ molecules but also shows the great advantage of H spillover method in the hydrogen storage study by providing a sufficiently low activation barrier for H adsorption on the substrate.

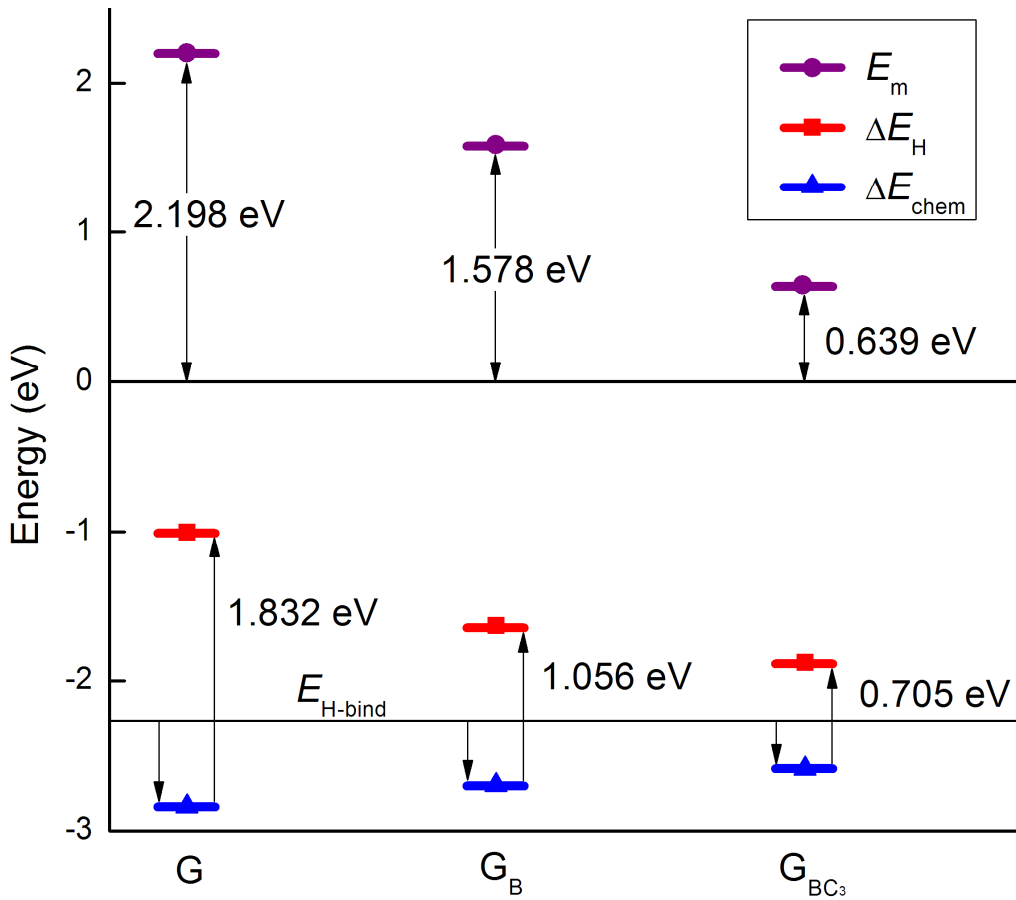


Figure 3.6 Evolution profiles of migration reaction energy E_m , hydrogen adsorption energy ΔE_H , and average H chemisorption energy ΔE_{chem} for the G, G_B, and G_{BC₃} sheets. The binding energy of H₂ molecule per H atom $E_{H-bind} = -2.272$ eV is denoted with a horizontal line. The single-arrow line points downward from E_{H-bind} to ΔE_{chem} , indicating the energetically favored H₂ dissociation process on the catalytic metal, and then points upward from ΔE_{chem} to ΔE_H , showing that the H migration from metal to substrate is endothermic. The difference between ΔE_{chem} and ΔE_H is labeled beside the single-arrow line.

Furthermore, under ambient conditions usually a small endothermic reaction is

affordable. The BC_3 sheet is a high symmetry substrate, with boron atoms uniformly distributed. The C atoms in G_{BC_3} are equivalent with the same ΔE_{H} ; thus, the H diffusion process on the G_{BC_3} sheet is thermodynamically favored or experimentally affordable under ambient conditions. As for the H migration process, the endothermic reaction can be improved by either enhancing $|\Delta E_{\text{H}}|$ of B-doped graphene or using other metal catalyst with smaller $|\Delta E_{\text{chem}}|$ than that of Pt_4 . Since the H adsorption strength $|\Delta E_{\text{H}}|=1.885$ eV for $\text{G}_{\text{BC}_3}\text{-C-H}$ is weaker than $|\Delta E_{\text{H}}|=1.933$ eV for $\text{G}_{\text{B}}\text{-C-H-ortho}$, a moderately B-doped graphene with boron uniformly distributed plus a proper catalytic metal may be a better candidate for hydrogen storage applications via hydrogen spillover, which would need further investigation in my future work.

3.4 Summary

In summary, by introducing B atoms into graphene, DFT calculations show substantially enhanced hydrogen adsorption strength for C atoms around B on the substrate, where the catalytic metal can also be firmly absorbed and further dissociate more H_2 molecules into H atoms. Upon H-saturation on the metal cluster, H atom is more likely to migrate from the bridge site of the cluster onto the supporting sheet. Due to reduced energetic difference between ΔE_{H} and ΔE_{chem} , an improved thermodynamical H migration process can be achieved on B-doped graphene. Both H migration and diffusion processes are investigated to have sufficiently low activation barriers, indicating that more H atoms can adsorb on B-doped graphene than on the undoped graphene under ambient conditions. By simulating the whole hydrogen spillover process, our work not only interprets the catalytic mechanism of the H spillover on B-doped graphene but also supports the experimental findings that B-doped microporous carbon has an enhanced hydrogen storage capacity.⁸⁶ Our calculations conclude that B doping with catalytic metal on the substrate is an effective method of modifying the graphitic surface for hydrogen storage applications.

Chapter 4

DFT Study of Hydrogen Spillover on Nitrogen Doped Graphene

Besides boron doping, nitrogen doping is another frequently used method to modify the properties of graphitic surface. In this chapter, as a comparison to the hydrogen spillover on B-doped graphene discussed in last chapter, the hydrogen spillover on N-doped graphene will be addressed with a focus on the H migration process.

4.1 Introduction

Nitrogen doping has been reported to facilitate the hydrogen uptake on microporous carbon materials.^{95, 96} For proton exchange membrane fuel cell, Pt-supported N-doped carbon was observed to have an enhanced catalytic activity and durability toward oxygen reduction and methanol oxidation.^{97, 98} Recently, Yang's group studied hydrogen storage via spillover on Pt-supported N-doped microporous carbon, and 2.4-fold enhanced hydrogen uptake of 1.26 wt % at 298 K and 10 MPa was obtained.⁹⁹ Apparently, N doping seems to be an effective approach in modifying the carbon materials for metal catalytic performance and hydrogen storage applications.

In the present work, first-principles calculations have been carried out to investigate the N doping effect on the hydrogen spillover on Pt₄-supported graphene. Two typical types of nitrogen species on N-doped graphene, graphitic N and pyridinic N, are considered in the simulation.^{100, 101} For the graphitic N, i.e., the 1N-doped graphene sheet, Pt₄ is found to saturate with 10 H atoms without detaching away from the supporting substrate after geometry optimization, and the H migration barrier from metal to substrate is estimated to be close to 2 eV, similar to that for the G_B case in Chapter 3. For the pyridinic N, where there is a C vacancy surrounded by three N substitutions in the graphene sheet, the Pt₄ cluster stands right above the vacancy site and can accommodate up to 16 H atoms upon saturation. The calculated H migration

barrier is about 1 eV, much lower than that for the graphitic N case. The comparison between B-doped and N-doped graphene for the hydrogen spillover is also addressed at the end.

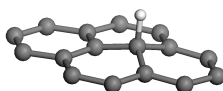
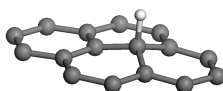

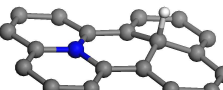
4.2 Computational methods

All calculations have been carried out by using the same methods and parameters as those used for B-doped graphene cases. The detailed descriptions can be found in Section 3.2. The only difference is that the transition state for H migration was estimated by using constrained geometry optimization method, due to the unique structural property of the H-saturated Pt₄ cluster on the N-doped graphene, which would be stated in detail in the following.

4.3 Results and discussion

4.3.1 Adsorption of H on 1N-doped graphene sheet

Table 4.1 Calculated hydrogen adsorption energy (ΔE_H), the corresponding H-bond length (d_{C-H}), and the Hirshfeld charges of N and H-bond related atoms, for the hydrogenation on pure graphene (G) and 1N-doped graphene sheet (G_N).^a

G-H/ G _N -H		ΔE_H (eV)	d_{C-H} (Å)	Hirshfeld charge		
				N	C	H
G-H		-1.009	1.124	-0.019	0.060	
G _N -C-H- <i>ortho</i>		-1.749	1.117	-0.004	0.029	0.039
G _N -C-H- <i>para</i>		-1.514	1.119	0.008	-0.025	0.044

^a The two lowest-energy structures for hydrogenated G_N sheet, as well as the optimized structure for hydrogenated graphene, are illustrated by side views. For clarity, only the hydrogenation regions are drawn as schematic diagrams (H, white; N, blue; C, grey).

For the graphitic N case, one nitrogen atom replaces a carbon atom in the

graphene sheet. Table 4.1 shows the calculated hydrogen adsorption energy of a single H atom on pure graphene (G) and on different sites of one N atom doped graphene sheet (G_N), the corresponding H-bond length, and the Hirshfeld charges of relevant atoms. The schematic diagram of each stable structure obtained after optimization is also illustrated. The deformation electron density isosurfaces, as well as the Hirshfeld charge distributions for the two hydrogenated G_N structures in Table 4.1 are depicted in Figure 4.1 to assist our analysis. According to Eq. (3.1), the calculated hydrogen adsorption strength $|\Delta E_H|$ for H atom adsorbed on the C atom next to (G_N -C-H-*ortho*) and opposite to (G_N -C-H-*para*) the N atom in the same hexagonal ring, is 1.749 eV and 1.514 eV, respectively, both stronger than that of 1.009 eV for the undoped graphene. Different from the G_B case, in which the H atom can be adsorbed on the doped B atom to form a stable structure (see G_B -B-H in Table 3.1), the doped N atom is not a stable site for H adsorption on the G_N sheet, according to our calculations. This is in good agreement with previous investigations that the neighboring carbon atom rather than the nitrogen atom is favorable for H adsorption.¹⁰²

From the isosurface of deformation electron density, which is calculated by subtracting the electron density of the isolated atoms from the total electron density, it can be found that there is a relatively small electron accumulation area (green regions) around the C-N bond, compared with that around other C-C bond on the substrate (Figure 4.1a, 4.1b). In the meantime, it shows a relatively big depletion of electron (yellow regions) around the N atom. This can be attributed to that nitrogen has one more valence electron than carbon, and the doped N disturbs the original π -electron distributions of the graphene sheet. The excessive electrons on N repel the electrons nearby and make them redistribute beyond a certain range towards the nitrogen on the G_N sheet. From the Hirshfeld charge distributions (Figure 4.1c, 4.1d), it can be seen that the Hirshfeld charges on the C atoms next to N are all positive with relatively large values, indicating that the C next to N is electron deficient, and would behave like an electron-acceptor. In this way, it facilitates the electron transfer from H to C, and thus the hydrogen adsorption strength is enhanced for the G_N sheet. In addition, since nitrogen has five valence electrons, the sp^2 -hybridized covalent network with

three C-N bonds formed in the G_N sheet is favorable for the doped N. That is the reason why H is not stable on N for the G_N sheet, because the nitrogen atom could not accommodate more electrons. On the contrary, carbon has four valence electrons and thus can form four covalent bonds to have a sp^3 -hybridized configuration. Therefore, the C-H bond is favorable to form on the graphitic surface. To summarize, the DFT calculations suggest that graphitic N doping can effectively enhance the surface hydrogenation strength of graphene, and the C atom adjacent to N is the most favorable site for hydrogen adsorption.

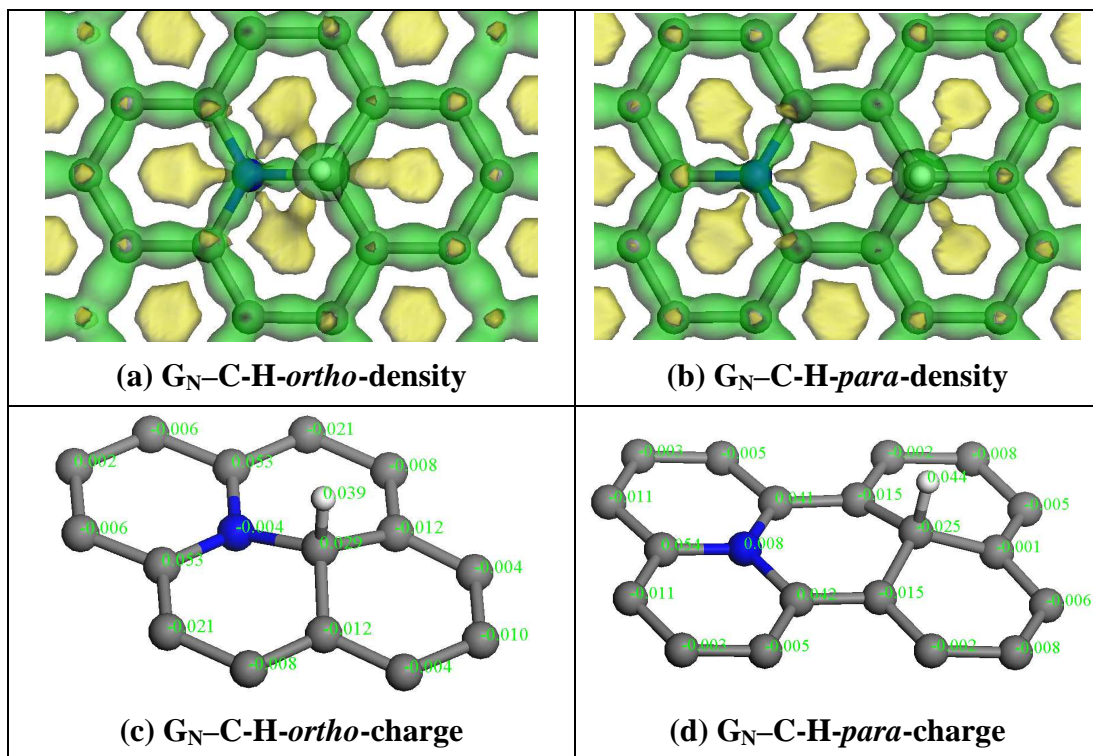


Figure 4.1 (a,b) Deformation electron density isosurfaces of the two hydrogenated structures for G_N sheet in Table 4.1 illustrated by top views (green, electron accumulation; yellow, electron depletion); (c,d) Hirshfeld charge distributions of the two hydrogenated structures for G_N sheet in Table 4.1 illustrated by side views (H, white; N, blue; C, grey).

4.3.2 Hydrogen adsorption and migration on Pt_4 -supported G_N sheet

To find the most stable structure for Pt_4 adsorbed on the G_N sheet, we put the tetrahedral Pt_4 cluster above various sites to have different initial configurations on the supporting substrate. As shown in Figure 4.2a, the Pt_4 cluster forms a stable

structure on the G_N sheet ($G_N\text{-Pt}_4$), in which three Pt atoms interact with the C-C bonds surrounding the N atom after the optimization. The corresponding adsorption strength $|\Delta E_{\text{Pt}}|$ for Pt_4 on G_N is about 1.582 eV, a little bit stronger than that of 1.184 eV for $G\text{-Pt}_4$ (see Figure 3.2a). Similar to the B-doping effect on the graphitic surface property, graphitic N doping not only improves the hydrogen adsorption ability, but also enhances the metal binding strength for graphene sheet.

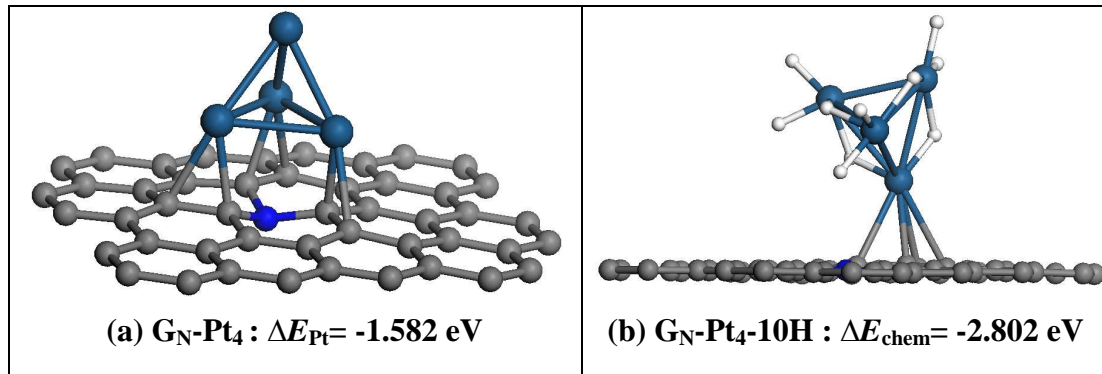


Figure 4.2 Optimized structures of (a) Pt_4 cluster on G_N sheet ($G_N\text{-Pt}_4$), and (b) saturated Pt_4 cluster on G_N sheet with 10 H atoms chemisorbed ($G_N\text{-Pt}_4\text{-10H}$) (H, white; N, blue; C, grey; Pt, cyan). The binding strength of Pt_4 $|\Delta E_{\text{Pt}}|$ on G_N sheet is 1.582 eV, a little bit stronger than that of 1.184 eV for the undoped graphene case. The chemisorption energy per H atom ΔE_{chem} for the saturated Pt_4 cluster on G_N sheet is about -2.802 eV, indicating a strong H_2 dissociation ability for the metal cluster.

The same strategy as that used in Chapter 3 has been implemented to simulate the H_2 dissociation process and model the H saturation on Pt_4 cluster. Initially eight H_2 molecules are put around the metal cluster at various locations for $G_N\text{-Pt}_4$. If the metal cluster detaches away from the supporting substrate after the optimization, then the initial number of H_2 molecules will be gradually reduced and the structure will be reoptimized, until we obtain the H-saturated Pt_4 cluster that does not lose the contact with the G_N sheet. As shown in Figure 4.2b, there are totally 10 H atoms fully chemisorbed on Pt_4 for G_N sheet ($G_N\text{-Pt}_4\text{-10H}$), with only one Pt binding to the underlying substrate. According to Eq. (3.2), the average chemisorption energy per H atom ΔE_{chem} on Pt_4 is estimated to be -2.802 eV for G_N sheet, with respect to the energy of a single H atom. Similar to the undoped graphene case (see Figure 3.2c), the Pt_4 cluster has a tendency to detach and leaves only one Pt atom in direct contact with

the supporting substrate upon hydrogenation, which indicates a weak interaction between Pt_4 and G_N sheet. Obviously, though the graphitic N doping enhances the metal binding strength for graphene sheet, it is still not strong enough to stabilize the Pt_4 cluster upon hydrogenation, and thus there is not much improvement of the H_2 dissociation ability for the metal cluster supported on the G_N sheet.

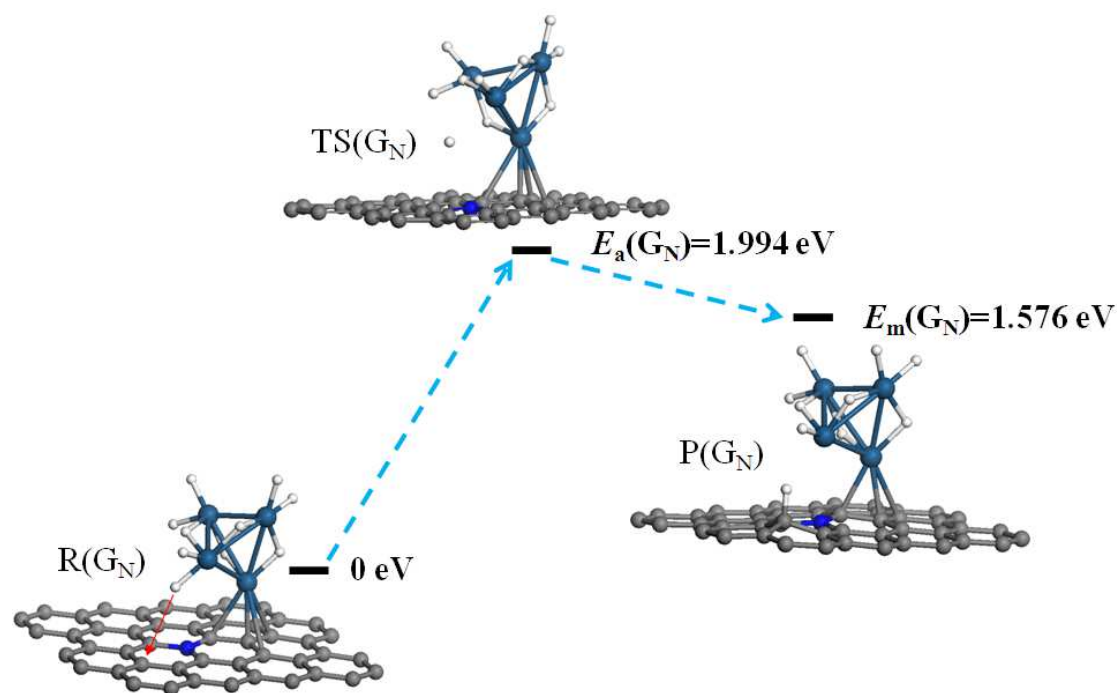


Figure 4.3 Optimized structures of initial (R), transition (TS), and final (P) states for the H migration process from saturated Pt_4 cluster to the supporting G_N sheet. The black bars denote the relative energy levels of these structures, with the corresponding schematic diagrams (H, white; N, blue; C, grey; Pt, cyan) drawn aside. The calculated activation energy E_a for the H migration from Pt_4 to the G_N sheet is 1.994 eV. The reaction energy of the migration E_m with respect to the initial state is estimated to be 1.576 eV. The dashed arrows are used to guide the eyes.

As we have known from Chapter 3, the H migration is the rate-limiting step in the hydrogen spillover process, and the migration barrier is the key factor that determines whether the H spillover gains fast kinetics under ambient conditions. As shown in Figure 4.3, by dragging one H atom from the initial reactant $\text{R}(\text{G}_\text{N})$ to the top of a C atom in the substrate, we carried out geometry optimizations subsequently to get the final product $\text{P}(\text{G}_\text{N})$. For clarity, the red arrow is used to depict the H migration direction, pointing to the targeted C atom on the G_N sheet. From our

calculations about H adsorption on G_N sheet, we know that the C atom adjacent to N is the most favorable site to adsorb H with $\Delta E_H = -1.749$ eV (see Table 4.1). However, the H atom would rebind to the Pt_4 cluster after optimization, due to the relatively close distance between the H atom and the metal cluster. Therefore, the C atom opposite to N in the hexagonal ring becomes the most favorable site for H adsorption, where H binds on top of the C to form a stable structure, with a C-H bond length of 1.136 Å (see $P(G_N)$ in Figure 4.3). Noticeably seen in $P(G_N)$, the Pt_4 cluster also moves toward the migrating H atom, showing kind of vibrational behavior for the metal cluster during the H migration process. Hence, the complete LST/QST method used to locate the transition state in Chapter 3 would not be valid for the G_N case, i.e., it would not find the transition state along the expected reaction coordinate for the H migration process. In this case, we thus used the constrained geometry optimization to estimate the H migration barrier, by gradually changing the Pt-H bond distance. The transition state $TS(G_N)$, as illustrated in Figure 4.3, has an activation energy $E_a(G_N) = 1.994$ eV for the H migration. The migrating H atom is away from hydrogenated Pt_4 with a Pt-H distance about 2.5 Å, and there is also no C-H bond formed in $TS(G_N)$. The corresponding reaction energy $E_m(G_N)$ is about 1.576 eV with respect to the energy of $R(G_N)$. Compared with the undoped graphene case (see Figure 3.3), both the activation and reaction energies have been lowered by almost 30% for the H migration on G_N sheet. However, the H migration process still has the activation energy of around 2 eV for G_N sheet, which greatly inhibits the hydrogen spillover at ambient conditions.

4.3.3 Adsorption of H on pyridinic-N doped graphene sheet

For the pyridinic N case, there are three nitrogen substitutions surrounding a carbon vacancy in the graphene sheet. By putting one H atom on different sites of the pyridinic-N doped graphene sheet (G_{pyr-N}), we obtained two lowest-energy structures for the hydrogenated G_{pyr-N} sheet after optimization. The schematic diagrams (a,b), the deformation electron density isosurfaces (c,d), as well as the Hirshfeld charge distributions (e,f) for these two hydrogenated G_{pyr-N} structures are illustrated in Figure

4.4. Figure 4.4a shows the most stable structure for the hydrogenated $G_{\text{pyr-N}}$ sheet, where the H atom occupies the vacancy site and binds with the three N atoms in the graphene plane ($G_{\text{pyr-N-V-H}}$). The calculated hydrogen adsorption energy is about -4.226 eV, indicating extremely high hydrogenation strength for the pyridinic-N doped graphene sheet. When the H atom binds onto the C atom opposite to the vacancy site in the hexagonal ring, it also forms a stable structure for the hydrogenated $G_{\text{pyr-N}}$ sheet (Figure 4.4b: $G_{\text{pyr-N-C-H-para}}$). The corresponding hydrogen adsorption energy for $G_{\text{pyr-N-C-H-para}}$ is estimated to be -2.021 eV, also showing enhanced hydrogenation ability for the $G_{\text{pyr-N}}$ sheet, compared with the undoped graphene case.

From the isosurface of deformation electron density, it can be found that there is a relatively small depletion of electron (yellow regions) around the vacancy site, accompanied by excessive electrons accumulation (green regions) around the N atoms, with dangling bonds pointing towards the vacancy (Figure 4.4c, 4.4d). On one hand, since nitrogen has one more valence electron than carbon and possesses relatively strong electron affinity, the N substitutes attract electrons from the nearby C atoms, resulting in a Hirshfeld charge of about -0.1 for each doped N, and that of ~ 0.05 for the adjacent C (Figure 4.4e, 4.4f). On the other hand, the excessive electrons on N atoms are stabilized by the vacancy site, which behaves as a hole and is very easy to trap electron donors like the H atom, thereby forming strong N-H bonds due to electron-hole interactions. Moreover, the pyridinic-N doping greatly changes the in-plane π -electron distribution of the graphene sheet. Electrons are more readily to move upward and thus facilitate the covalent bond formation. In this way, the hydrogen adsorption strength is also substantially enhanced, considering both the sp^3 -hybridization and structural symmetry, for the C atom on the $G_{\text{pyr-N}}$ sheet ($G_{\text{pyr-N-C-H-para}}$). In a word, the DFT calculations suggest that pyridinic-N doping is more effective in modifying surface hydrogenation strength of graphene, compared with the graphitic-N doping. Therefore, great improvement of H migration barrier in the hydrogen spillover process is expected on the $G_{\text{pyr-N}}$ sheet.

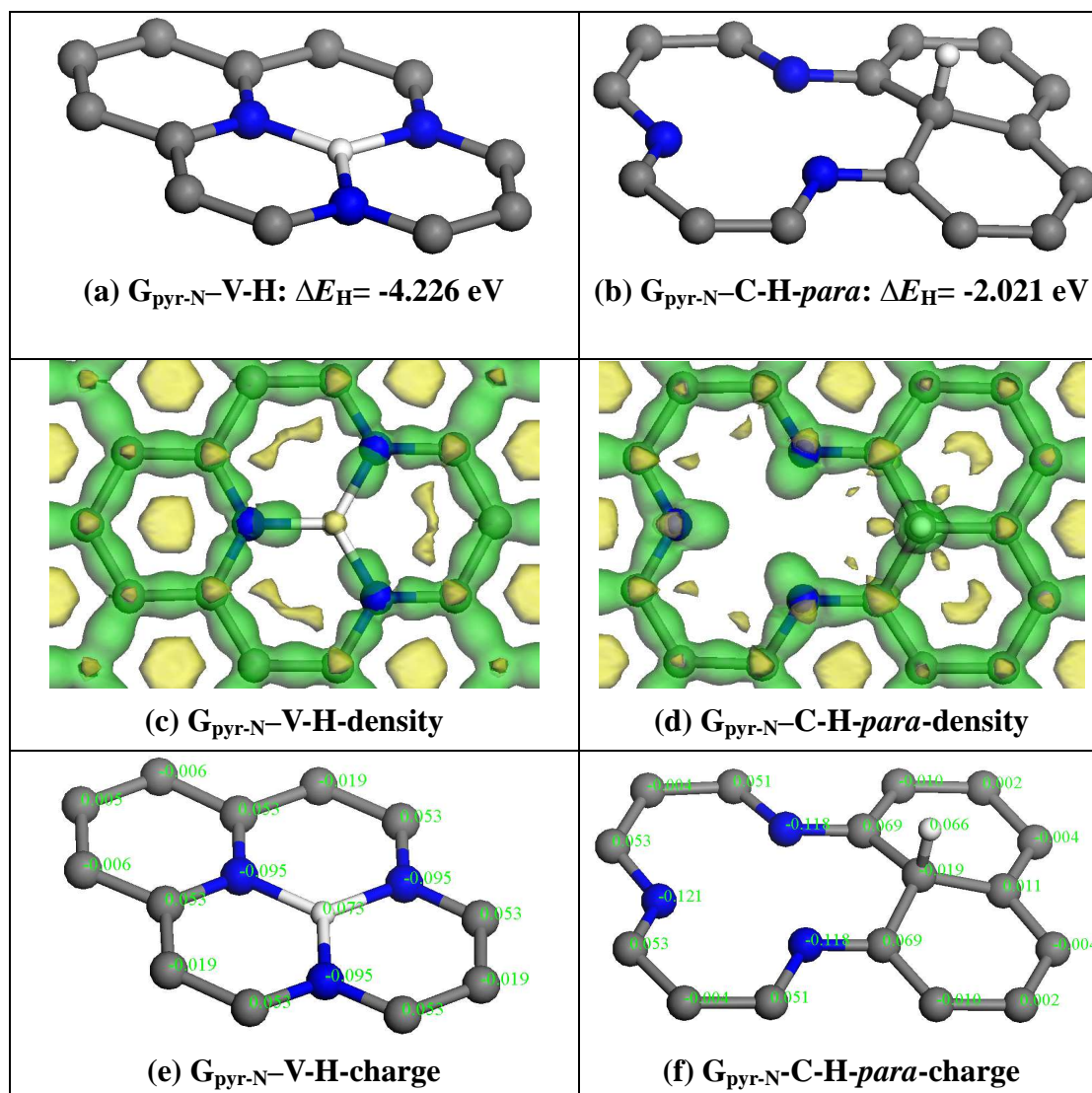


Figure 4.4 (a,b) Schematic diagrams of two lowest-energy structures for hydrogenated $G_{\text{pyr-N}}$ sheet illustrated by side views (H, white; N, blue; C, grey); (c,d) Top views of deformation electron density isosurfaces of (a,b) (green, electron accumulation; yellow, electron depletion); (e,f) Side views of Hirshfeld charge distributions of (a,b).

4.3.4 Hydrogen adsorption and migration on Pt_4 -supported $G_{\text{pyr-N}}$ sheet

Different from the G_{N} case, the tetrahedral Pt_4 cluster was found to stand above the vacancy site and bind with three N atoms after the optimization, with only one Pt atom in contact with the $G_{\text{pyr-N}}$ sheet to form a stable structure (Figure 4.5a: $G_{\text{pyr-N-Pt}_4}$). The calculated adsorption strength $|\Delta E_{\text{Pt}}|$ for Pt_4 on $G_{\text{pyr-N}}$ is about 3.925 eV, much stronger than that of 1.582 eV for $G_{\text{N-Pt}_4}$ (see Figure 4.2a). Apparently, pyridinic-N doping produces better hydrogen/metal adsorption ability for graphene sheet than the

graphitic N does.

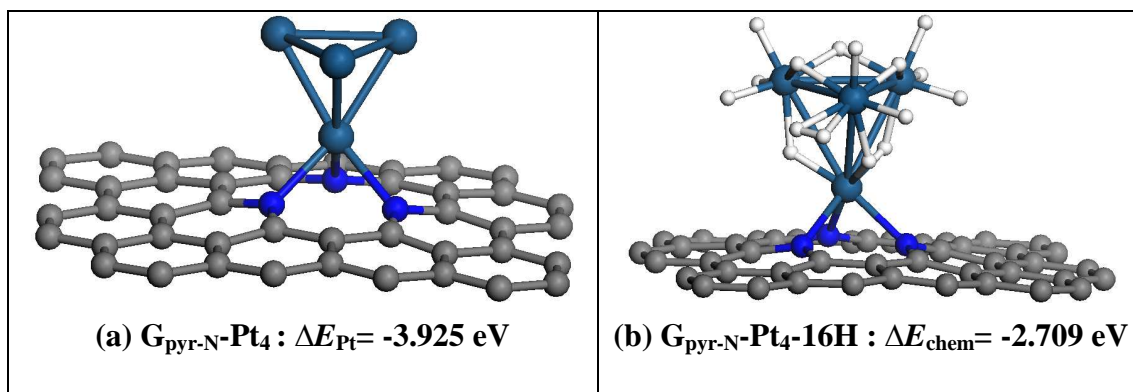


Figure 4.5 Optimized structures of (a) Pt₄ cluster on G_{pyr-N} sheet (G_{pyr-N-Pt₄}), and (b) saturated Pt₄ cluster on G_{pyr-N} sheet with 16 H atoms chemisorbed (G_{pyr-N-Pt₄-16H}) (H, white; N, blue; C, grey; Pt, cyan). The binding strength of Pt₄ $|\Delta E_{\text{Pt}}|$ on G_{pyr-N} sheet is 3.925 eV, much stronger than that for G_N-Pt₄. The average chemisorption strength per H atom $|\Delta E_{\text{chem}}|$ for the saturated Pt₄ cluster on G_{pyr-N} sheet is about 2.709 eV, which is weaker than that for G_N-Pt₄-10H.

Without losing the contact with the G_{pyr-N} sheet, as shown in Figure 4.5b, it was found to saturate with 16 H atoms chemisorbed on the bridge or corner sites of Pt₄ (G_{pyr-N-Pt₄-16H}) after the optimization. Among these sixteen H atoms, fourteen are from seven fully dissociated H₂ molecules via the metal cluster, and two are from one partially dissociated H₂ with a H-H bond length of about 0.846 Å. The corresponding chemisorption strength per H atom $|\Delta E_{\text{chem}}|$ for G_{pyr-N-Pt₄-16H} is estimated to be 2.709 eV, weaker than that of 2.802 eV for G_N-Pt₄-10H. Compared with the G_N case, more H₂ molecules can be dissociated by and then adsorbed on the Pt₄ cluster supported by the G_{pyr-N} sheet, resulting in the averagely reduced chemisorption strength per H atom for the H-saturated Pt₄ cluster. Although only one Pt atom is in direct contact with the supporting substrate, the metal cluster upon H-saturation still firmly binds with the nitrogen atoms in the G_{pyr-N} sheet. Obviously, the pyridinic-N doping can effectively stabilize the metal catalyst upon hydrogenation, which would then serve as a stable H source for the subsequent H migration from metal to the G_{pyr-N} sheet.

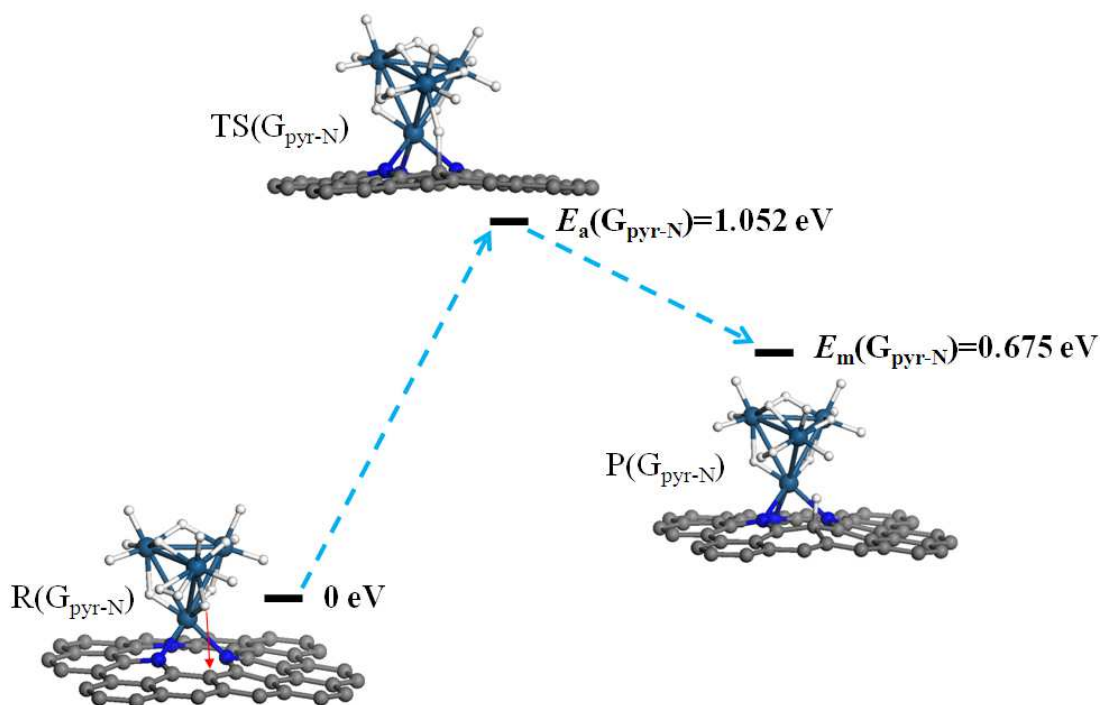


Figure 4.6 Optimized structures of initial (R), transition (TS), and final (P) states for the H migration process from saturated Pt_4 cluster to the supporting $\text{G}_{\text{pyr-N}}$ sheet. The black bars denote the relative energy levels of these structures, with the corresponding schematic diagrams (H, white; N, blue; C, grey; Pt, cyan) drawn aside. The calculated activation energy E_a for the H migration from Pt_4 to the $\text{G}_{\text{pyr-N}}$ sheet is about 1.052 eV. The reaction energy of the migration E_m with respect to the initial state is estimated to be 0.675 eV. The dashed arrows are used to guide the eyes.

As shown in Figure 4.6, by dragging one H atom from the initial reactant $\text{R}(\text{G}_{\text{pyr-N}})$ to the top of the unoccupied C atom opposite to the vacancy site in the hexagonal ring, which represents the most feasible way for the H migration reaction from Pt_4 to the $\text{G}_{\text{pyr-N}}$ sheet according to our calculations (see Figure 4.4b), we carried out geometry optimizations subsequently to get the final product $\text{P}(\text{G}_{\text{pyr-N}})$. For clarity, the red arrow is used to depict the H migration direction, pointing to the targeted C atom on the $\text{G}_{\text{pyr-N}}$ sheet. The optimized structure of $\text{P}(\text{G}_{\text{pyr-N}})$ has a C-H bond length of 1.132 Å, with the metal cluster slightly lean to the migration H atom. We used the constrained geometry optimization method to estimate the H migration barrier, by gradually changing the C-H bond distance. The transition state $\text{TS}(\text{G}_{\text{pyr-N}})$, as illustrated in Figure 4.6, was located at a C-H bond length of about 1.5 Å, with the activation energy $E_a(\text{G}_{\text{pyr-N}})=1.052$ eV for the H migration. The corresponding

reaction energy $E_m(G_{\text{pyr-N}})$ is about 0.675 eV with respect to the energy of $R(G_{\text{pyr-N}})$. Compared with the G_N case, the H migration process is substantially improved both kinetically and thermodynamically on the $G_{\text{pyr-N}}$ sheet. Accordingly, we can conclude that the pyridinic-N doping can greatly enhance the surface hydrogenation strength of the graphene sheet and effectively lower the H migration barrier to be about 1 eV, though still high for room temperature applications. The pyridinic-N doping thus should be responsible for the H spillover process on N-doped graphene rather than the graphitic-N doping.

4.3.5 Comparison between B-doped and N-doped graphene for the H spillover

Since we have investigated the hydrogen spillover process through first-principles calculations on both B-doped and N-doped graphenes, the comparison between these two cases would certainly lead us to some basic points about the H spillover mechanism on the graphitic surface.

First, the metal cluster as a catalyst for hydrogen dissociation in the H spillover is an indispensable medium, through which H atoms can migrate onto the supporting substrate with relatively fast kinetics, since direct dissociation of H_2 on the graphene is always with a high activation barrier.

Second, the low activation barrier for H migration from metal to substrate requires both the stable H-saturated metal cluster and the strong surface hydrogenation strength. Both boron doping and nitrogen doping can meet the requirements but with different manners. For B-doped graphene, direct substitution of boron for carbon can effectively enhance the hydrogen adsorption ability of graphene, and stabilize the metal catalyst upon hydrogenation. While for N-doped graphene, direct substitution of nitrogen for carbon, i.e. the graphitic-N doping, has small influence on the metal stabilization. It is the pyridinic-N doping that greatly improves both the hydrogenation ability and the metal binding strength for the graphene sheet.

Third, since the doped B or N atoms only have an influence on the nearby C atoms on the substrate, further diffusion of the migrated H atoms on the graphene sheet would be difficult with a high diffusion barrier. Therefore, a doped graphene

sheet with B or N uniformly distributed would be a good candidate for hydrogen storage applications by H spillover. For B-doped graphene, the high symmetry BC₃ sheet, the bulk material of which can be experimentally synthesized, can have a relatively low activation barrier for the H diffusion on the substrate (see Figure 3.5). While for the N-doped case, no proper materials with uniform distributions of the pyridinic-N on the graphitic surface are ever reported. Nevertheless, since both graphitic N and pyridinic N are observed experimentally, it is more likely to have some graphitic-N distributed among the pyridinic-N on the substrate, which would facilitate the whole H spillover process for practical applications. Such a kind of graphene sheet in which graphitic-N and pyridinic-N are co-doped with some pattern, is an interesting model substrate, and it will be investigated for the hydrogen spillover study in my future work.

4.4 Summary

In summary, two types of N-doped (graphitic-N, pyridinic-N) graphene sheets were investigated for the hydrogen spillover study. DFT calculations show that both graphitic-N and pyridinic-N doping can enhance the hydrogenation strength for C atoms around N on the substrate. However, the catalytic metal can only be firmly absorbed on the pyridinic-N doped graphene sheet and further dissociate more H₂ molecules into H atoms, compared with the undoped graphene case. The simulation on the hydrogen migration reaction, the rate-limiting step in the H spillover process, gives a substantially lowered activation barrier of about 1 eV for H migration from metal to pyridinic-N doped graphene, indicating that pyridinic-N doping could be an effective approach in modifying graphitic surface for hydrogen storage applications by H spillover. Further improvement on the H spillover effect for N-doped graphene is highly desired, and the co-doping of graphitic-N and pyridinic-N on the graphene sheet, where graphitic-N may distribute among pyridinic-N with some pattern, is expected to contribute at this point, which needs further investigations in the future.

Chapter 5

DFT Study of Hydrogen Spillover on Carbon Doped Boron Nitride Sheet

As an analogue to the graphene sheet, boron nitride (BN) sheet is chosen as a substrate for hydrogen spillover study in this chapter. The carbon doping effect on the surface hydrogenation ability of the BN sheet will be investigated. The metal catalytic performance, as well as the possibility of hydrogen spillover on C doped BN sheet will be addressed.

5.1 Introduction

As an analogue to the graphene, hexagonal boron nitride (BN) sheet has received much attention. Graphene and BN sheet have similar structural motifs yet different electronic properties. The graphene sheet is a semimetal, with purely covalent C-C bonds. While the BN sheet is a wide band gap semiconductor, with partially ionic B-N bonds due to the electron donation from B to N. Recently, the single layer BN sheet has been successfully synthesized.¹⁰³ The polarizable property of BN sheet was predicted to be beneficial to the H₂ adsorption under the electric fields.⁵⁴ The hydrogen chemisorption property on the hexagonal BN sheet was also investigated, and the barrier was estimated to be 2.39 eV when a H₂ was dissociated on the neighboring B and N atoms.¹⁰⁴ Obviously, the high H₂ dissociation barrier indicates the weak hydrogenation ability for the BN sheet. As we have known from the last two chapters, the hydrogen spillover method is a good approach in lowering the activation barrier for hydrogen chemisorption with the help of metal catalyst, and the doping method is very effective in modifying the hydrogen adsorption strength of the substrate. Therefore, it could be an interesting work to study the hydrogen spillover property on the carbon doped BN sheet.

In the present work, first-principles calculations have been carried out to investigate the hydrogen spillover property on Pt₄-supported BN sheet. We used a C

atom to substitute for one B (C_B) or N (C_N) site in the BN sheet, both showing great enhancement in the hydrogenation ability for the substrate. For the C_B case, Pt_4 is found to saturate with 10 H atoms without detaching away from the supporting substrate after geometry optimization, and the H migration barrier from metal to substrate is estimated to be over 2 eV, which inhibits the H spillover from taking place. For the C_N case, the Pt_4 can accommodate up to 16 H atoms towards saturation without losing the contact with the BN sheet. The calculated H migration barrier is about 1.4 eV, much lower than that for the C_B case, though still high for the H spillover to occur under ambient conditions. The comparison between B/N-doped graphene and C-doped BN sheet for the hydrogen spillover is also addressed at the end of this chapter.

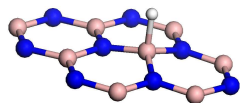
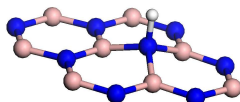
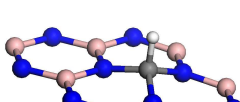
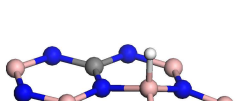
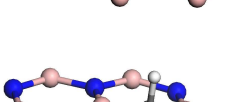
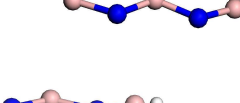
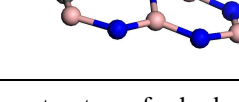
5.2 Computational methods

All calculations have been carried out by using the same methods and parameters as those used for B(N)-doped graphene cases in the last two chapters. The detailed descriptions can be found in Section 3.2. A (6×6) supercell with periodic boundary conditions on the x - y plane was employed to model the infinite boron nitride sheet. The vacuum space was set with 20 Å in the z direction to avoid the interactions between periodic images. The transition state for H migration was estimated by using constrained geometry optimization method. The in-plane lattice parameter of the BN sheet has been optimized to be 2.519 Å, which is close to the experimental value of 2.505 Å.¹⁰⁵

5.3 Results and discussion

5.3.1 Adsorption of H on boron nitride sheet and 1C-doped BN sheet

Table 5.1 Calculated hydrogen adsorption energy (ΔE_H), the corresponding H-bond length ($d_{C-H}/d_{B(N)-H}$), and the Hirshfeld charges of C and H-bond related atoms, for the hydrogenation on boron nitride sheet and 1C-doped BN sheet (BN- $C_{B(N)}$).^a

BN-H/ BN- $C_{B(N)}$ -H		ΔE_H (eV)	$d_{C-H}/d_{B(N)-H}$ (Å)	Hirshfeld charge			
				B	N	C	H
BN-B-H		-0.011	1.299	0.092			-0.002
BN-N-H		0.836	1.075		-0.120		0.104
BN- C_B -C-H		-3.556	1.107			0.120	0.031
BN- C_B -B-H- <i>meta</i>		-2.659	1.237	0.065		0.200	-0.104
BN- C_N -C-H		-3.946	1.117			-0.219	0.067
BN- C_N -N-H- <i>meta</i>		-1.997	1.036		-0.098	-0.304	0.161

^a The two lowest-energy structures for hydrogenated BN- $C_{B(N)}$ sheet, as well as the optimized structures for hydrogenated boron nitride sheet, are illustrated by side views. For clarity, only the hydrogenation regions are drawn as schematic diagrams (H, white; B, pink; C, grey; N, blue).

The influence of carbon doping on the hydrogenation of boron nitride sheet was investigated. There are two simplest ways for C doping on the BN sheet: one is a C substituting for a B atom (C_B); the other is a C replacing one N atom (C_N). Table 5.1 shows the calculated hydrogen adsorption energy of a single H atom on boron nitride sheet and on one C atom doped BN sheet (BN- $C_{B(N)}$), the corresponding H-bond

length, and the Hirshfeld charges of relevant atoms. The schematic diagram of each stable structure obtained after optimization is also illustrated. The deformation electron density isosurfaces for the six hydrogenated structures in Table 5.1 are depicted in Figure 5.1 to assist our analysis. According to Eq. (3.1), the calculated hydrogen adsorption energy ΔE_H for H atom adsorbed on the B (BN-B-H) and N (BN-N-H) site of the BN sheet is -0.011 eV and 0.836 eV, respectively. Evidently, the surface hydrogenation ability of BN sheet is even weaker than that of pure graphene, indicating that the hydrogen spillover could not take place on the pristine BN sheet under ambient conditions. In contrast, great improvement on the hydrogenation strength is obtained for the C doped BN sheet. For the C_B case, the hydrogen adsorption strength $|\Delta E_H|$ is about 3.556 eV for H adsorbed on the doped C (BN- C_B -C-H). When H is adsorbed on the nearest B site to the doped C atom (BN- C_B -B-H-*meta*), the corresponding $|\Delta E_H|$ is estimated to be 2.659 eV, much larger than that for BN-B-H on the pristine BN. Similarly, for the C_N case, $|\Delta E_H|$ also has a large value of 3.946 eV and 1.997 eV for H adsorbed on C (BN- C_N -C-H) and the nearest N site to C (BN- C_N -N-H-*meta*), respectively. Therefore, not only the doped C atom works as an active site for H adsorption but also the B or N site close to the doped C on the BN sheet is greatly influenced with strong hydrogenation ability.

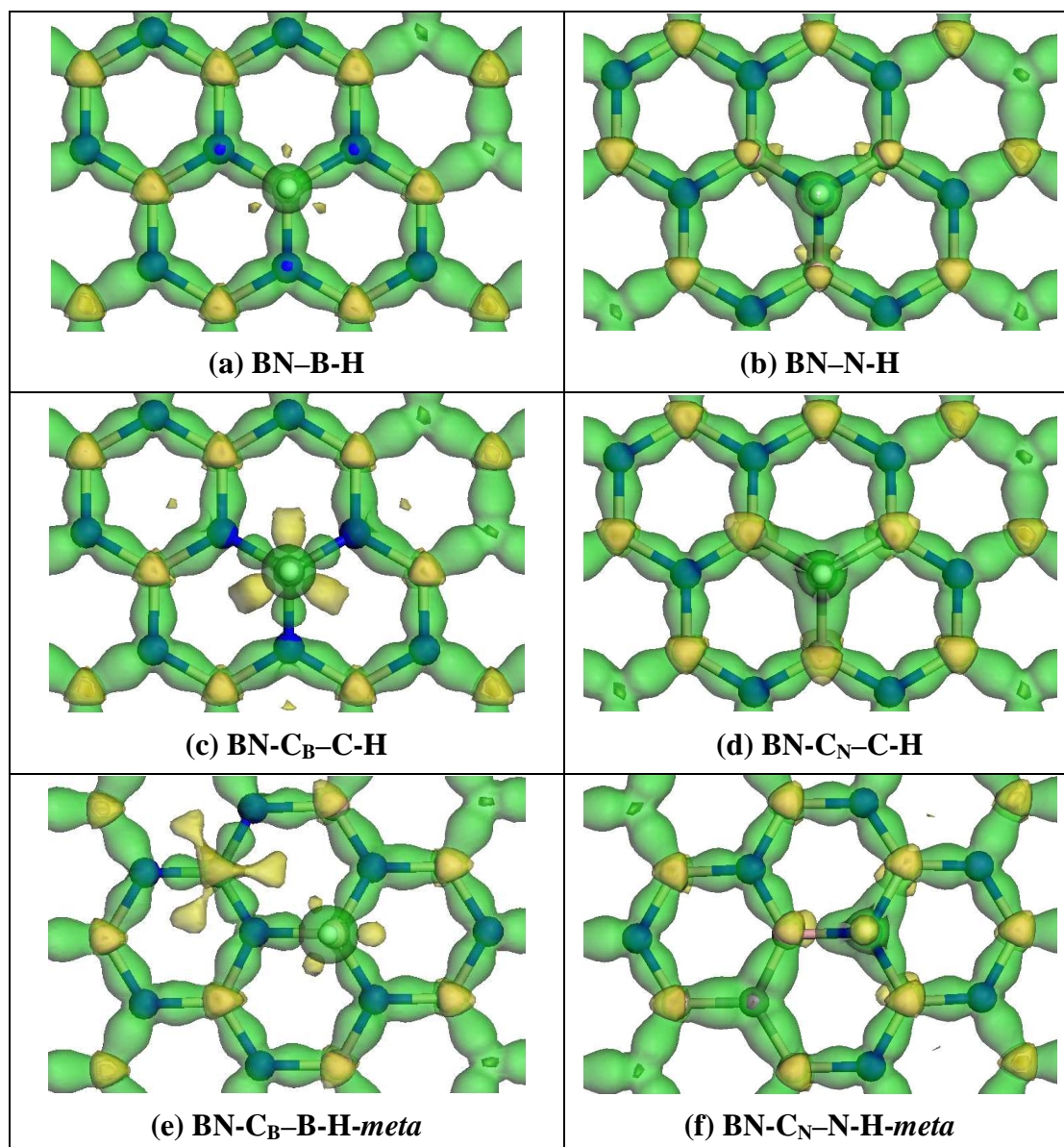


Figure 5.1 Deformation electron density isosurfaces of the six hydrogenated structures in Table 5.1 illustrated by top views (green, electron accumulation; yellow, electron depletion).

From the isosurface of deformation electron density, as shown in Figure 5.1, it can be found that the electrons accumulate (green regions) between B-N bonds and deplete (yellow regions) on boron atoms due to the electron transfer from B to N on the BN sheet. However, there is no electron depletion area in the centre of the BN hexagonal ring, which is different from that of the graphene case (see Figure 3.1), indicating that the electrons are more localized in the BN sheet than they are in the graphene. Since both B and N atoms prefer the sp^2 -hybridized interactions, they form

a very stable B-N network in 2D, i.e. the BN sheet. In this way, the coupling between the localized in-plane electrons and the electron of H atom is very small, resulting in very weak hydrogen adsorption on either B (BN-B-H) or N (BN-N-H) for the pristine BN sheet. When one C substitutes for a B, there is a relatively large electron depletion area around the doped C (Figure 5.1c, 5.1e) due to the electron transfer from C to N, with C possessing a large positive value in terms of Hirshfeld charge. On one hand, C atom prefers sp^3 -hybridized interactions and thus leads to greatly enhanced hydrogenation strength for BN-C_B-C-H. On the other hand, since C has one more valence electron than B, the electron transfer from C to N weakens the electron donation from B to N. Hence, more electrons on B can assist in the B-H bonding and produce strong H adsorption strength for BN-C_B-B-H-*meta*. In contrast, when a C replaces one N, the doped C will behave as an electron acceptor with a large negative value of Hirshfeld charge, and there is a relatively large electron accumulation area around it (Figure 5.1d, 5.1f). Since C has one less valence electron than N, much electron transfer from B to C will result in less electron flow from B to N. Therefore, the electron of H would have more coupling with the electrons of the targeted N atom without experiencing strong electron repulsion, compared with the undoped BN case. So improved hydrogenation strength is obtained for BN-C_N-N-H-*meta*. Increased H adsorption strength is also achieved for BN-C_N-C-H due to the sp^3 -hybridization of the C atom. In a word, C doping greatly improves the hydrogenation ability of the BN sheet, and the hydrogen spillover is thus expected on the C doped BN sheet.

5.3.2 Hydrogen adsorption on Pt₄ cluster supported by C-doped BN sheet

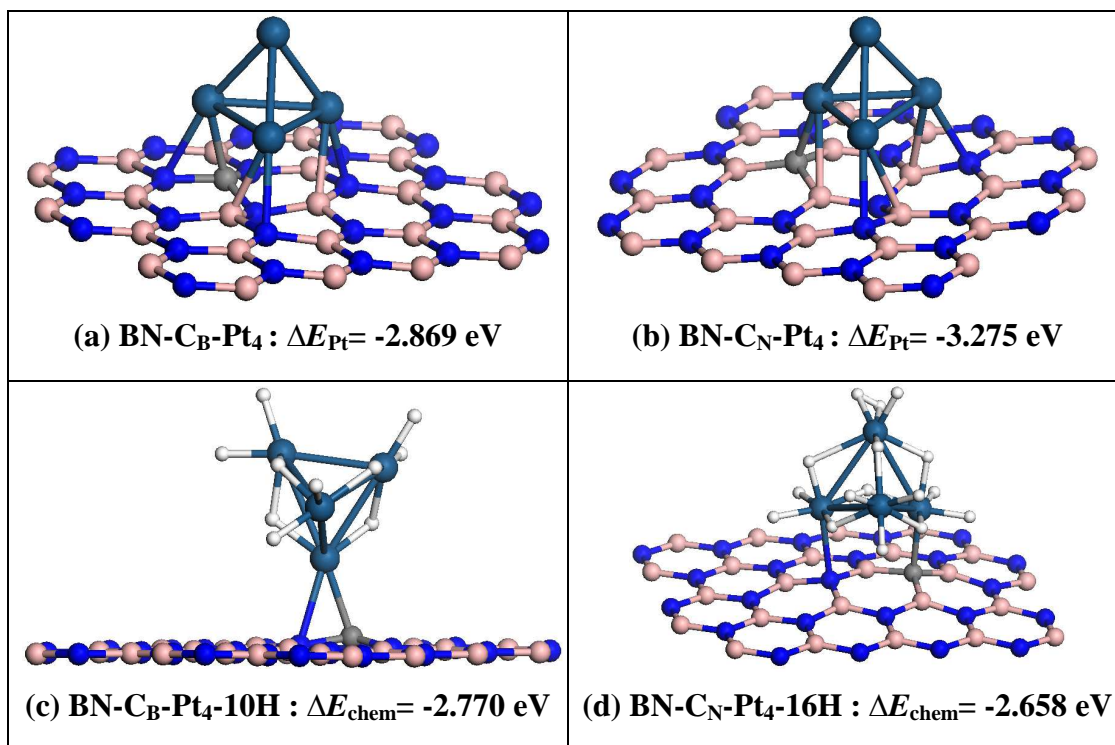


Figure 5.2 Optimized structures of (a) Pt₄ cluster on BN-C_B sheet (BN-C_B-Pt₄), (b) Pt₄ cluster on BN-C_N sheet (BN-C_N-Pt₄), (c) saturated Pt₄ cluster on BN-C_B with 10 H atoms chemisorbed (BN-C_B-Pt₄-10H), and (d) saturated Pt₄ cluster on BN-C_N sheet with 16 H atoms chemisorbed (BN-C_N-Pt₄-16H) (H, white; B, pink; C, grey; N, blue; Pt, cyan). The binding strength of Pt₄ $|\Delta E_{Pt}|$ on BN-C_N sheet is 3.275 eV, stronger than that of 2.869 eV on BN-C_B sheet. The chemisorption energy per H atom ΔE_{chem} for the saturated Pt₄ cluster on BN-C_B and BN-C_N sheet is -2.770 eV and -2.658 eV, respectively, indicating a strong H₂ dissociation ability for the metal cluster.

As stated in the last two chapters, the tetrahedral Pt₄ cluster is chosen as the representative metal catalyst and is put above various sites of the BN-C_{B(N)} sheet, in order to find the most stable structure for Pt₄ adsorbed on the supporting substrate. As shown in Figure 5.2a, the Pt₄ cluster is attached to the BN-C_B sheet (BN-C_B-Pt₄) with three Pt atoms above the B-N or C-N bonds after the optimization. The adsorption energy of Pt₄ on the BN-C_B sheet ΔE_{Pt} is calculated to be -2.869 eV. Similarly, there are also three Pt atoms that interact with the B-N or B-C bonds to form a stable structure on the BN-C_N sheet (Figure 5.2b, BN-C_N-Pt₄). The corresponding adsorption strength $|\Delta E_{Pt}|$ for Pt₄ on BN-C_N is about 3.275 eV, stronger than that for BN-C_B-Pt₄.

The same procedure as described in the last two chapters was carried out to model the H₂ dissociation process on Pt₄ cluster and to obtain a H-saturated metal cluster on the supporting BN-C_{B(N)} sheet. For BN-C_B, without losing the contact between Pt₄ and the supporting substrate after the optimization, there are totally 10 H atoms fully chemisorbed on Pt₄ (Figure 5.2c, BN-C_B-Pt₄-10H), which has only one Pt remain binding with the C-N bond of the BN-C_B sheet upon H saturation. According to Eq. (3.2), the average chemisorption energy per H atom ΔE_{chem} on Pt₄ is estimated to be -2.770 eV for BN-C_B sheet, with respect to the energy of a single H atom. While for BN-C_N, the supported Pt₄ cluster can chemisorb 16 H atoms (Figure 5.2d, BN-C_N-Pt₄-16H) with $\Delta E_{\text{chem}}=-2.658$ eV, where the Pt₄ cluster has a lateral moving and leaves two Pt atoms still bind to the underlying substrate after the optimization. Noticeably on the upper Pt atom, two adsorbed H atoms are from one partially dissociated H₂ with a H-H bond length of about 0.863 Å. Both cases of the C-doped BN sheets show somehow unstable metal binding on the substrate upon hydrogenation, which indicates that the H-saturated Pt₄ cluster may not serve as a stable H source for the subsequent H migration from metal to the BN-C_{B(N)} sheet.

5.3.3 H migration from Pt₄ cluster onto the supporting BN-C_{B(N)} sheet

As shown in Figure 5.3, by dragging one H atom from the starting reactant (R) to the top of a B(N) atom in the substrate, we carried out geometry optimization subsequently to get the final product (P). However, for the BN-C_{B(N)} sheet, we found the H atom would migrate back to the Pt₄ cluster after the optimization, i.e. it only forms a metastable state for the hydrogenation due to the presence of Pt₄ cluster (see P(BN-C_B) and P(BN-C_N) in Figure 5.3). In this case, we thus used the constrained geometry optimization to locate the transition state (TS) and estimate the H migration barrier, by gradually changing the Pt-H bond length. For clarity, the red arrow is used to depict the H migration direction, pointing to the targeted B(N) atom on the substrate.

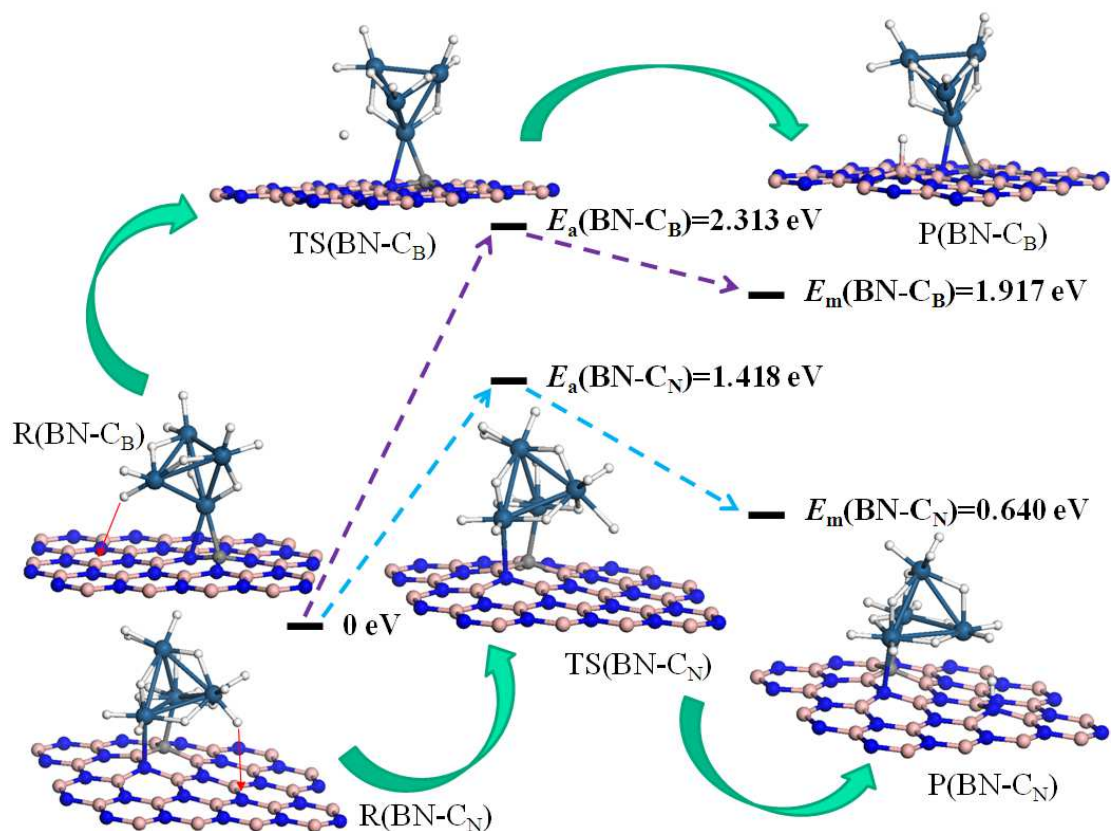


Figure 5.3 Optimized structures of initial (R), transition (TS), and final (P) states for the H migration process from saturated Pt_4 cluster to the supporting $\text{BN-C}_{\text{B(N)}}$ substrate. The black bars denote the relative energy levels of these structures, with the corresponding schematic diagrams (H, white; B, pink; C, grey; N, blue; Pt, cyan) drawn above or below. The calculated activation energy E_a for the H migration from Pt_4 to BN-C_B and BN-C_N sheet is 2.313 eV and 1.418 eV, respectively. The purple and blue dashed arrows are respectively used to guide the eyes for the two separate migration reactions on BN-C_B and BN-C_N substrates. The reaction energy of the migration E_m with respect to the initial state is estimated to be 1.917 eV and 0.640 eV, respectively, for the BN-C_B and BN-C_N cases.

As illustrated in Figure 5.3, the calculated activation barrier $E_a(\text{BN-C}_\text{B})$ for H migrating to the BN-C_B sheet is about 2.313 eV, and the corresponding transition state $\text{TS}(\text{BN-C}_\text{B})$ has a Pt-H distance about 2.7 Å. There is no bond formed for the migrating H atom in $\text{TS}(\text{BN-C}_\text{B})$, indicating an unrealistic migration process for the BN-C_B sheet. The migration reaction energy $E_m(\text{BN-C}_\text{B})$ is around 1.917 eV with respect to the energy of initial state $\text{R}(\text{BN-C}_\text{B})$. Both the high values of $E_a(\text{BN-C}_\text{B})$ and $E_m(\text{BN-C}_\text{B})$ prohibit the H migration at ambient conditions for BN-C_B . While for the BN-C_N case, the transition state $\text{TS}(\text{BN-C}_\text{N})$, as shown in Figure 5.3, has an

activation energy $E_a(\text{BN-C}_N)=1.418$ eV for the H migration, with a Pt-H bond length of 2.15 Å. The corresponding reaction energy $E_m(\text{BN-C}_N)$ is about 0.640 eV with respect to the energy of R(BN-C_N). Both the activation and reaction energies have been greatly improved for the H migration on BN-C_N sheet compared with the BN-C_B case. Noticeably seen from Figure 5.3, the partially dissociated H₂ molecule in R(BN-C_N) becomes fully dissociated on the upper Pt atom of the metal cluster in P(BN-C_N) after the H migration. This eventually results in the much improved thermodynamical migration reaction. However, the H migration barrier for BN-C_N is still as high as about 1.4 eV, which is not applicable for the hydrogen spillover at ambient conditions.

Moreover, the direct dissociation of H₂ on the BN-C_{B(N)} sheet was also investigated since the doped C atom is very active with strong hydrogenation ability. The H₂ vertically binds over the doped C atom to form a physisorption state. We performed the constrained geometry optimizations by gradually changing the H-H bond distance. The calculated H₂ dissociation barriers for both C-doped cases are over 1 eV, indicating the difficulty for direct dissociation of H₂ on the BN-C_{B(N)} sheet. Hence, whether to use metal catalyst or not on the substrate, the H chemisorption is hard to achieve on the BN-C_{B(N)} sheet under ambient conditions.

5.3.4 Comparison between B/N-doped graphene and C-doped BN sheet for the H spillover

Now we can have a comparison between B/N-doped graphene and C-doped BN sheet to have a better understanding of the hydrogen spillover on these substrates. First, the doping method (B/N replacing C or vice versa) is an effective approach in modifying the hydrogenation ability of the substrates, both B/N-doped graphene and C-doped BN sheet exhibiting enhanced hydrogen adsorption strength compared with the undoped case. Second, the electron-deficient doping (G_B , $G_{\text{pyr-N}}$, and BN-C_N), which creates an electron acceptor on the substrate, can have relatively stronger metal binding strength than the electron-sufficient doping (G_N and BN-C_B) for graphene or BN sheet, and thus can have more H atoms chemisorbed on the metal cluster with

relatively high stability. The activation barrier of H migration from metal to substrate is also relatively lower for the electron-deficient doping than the electron-sufficient doping on graphene or BN sheet. Therefore, the electron-deficient doping is the favored method to improve kinetics for hydrogen spillover on both graphene and BN sheet. Third, as we have discussed in the last chapter, a uniform distribution of B or N dopants on graphene would facilitate the whole H spillover process on the substrate. However, since C-C and B-N bonds are more stable than B-C and C-N bonds, C atoms would not uniformly distribute but form a domain on the BN sheet, which indicates that C-doped BN sheet is not a suitable material for hydrogen storage applications by H spillover. We can conclude that B/N-doped graphene is a favorable material over C-doped BN sheet for H spillover and should be investigated with much efforts in the future.

5.4 Summary

In summary, C-doped BN sheet with a C replacing one B (BN-C_B) or one N (BN-C_N) was investigated for the hydrogen spillover study. DFT calculations show that C doping can greatly improve the hydrogenation ability for the BN-C_{B(N)} sheet, in which the doped C atom is the most favorable site for hydrogen adsorption. Strong metal binding strength is also obtained on the BN-C_{B(N)} sheet; however, the catalytic metal upon hydrogenation shows a tendency of detaching away from the supporting substrate, indicating some kind of instability for the catalytic performance in the hydrogen spillover process. The calculated activation barriers for H migration from metal to substrate are about 2.3 eV and 1.4 eV for BN-C_B and BN-C_N, respectively, both high values prohibiting the H migration reaction at ambient conditions. Further improvement on the substrate to have C atoms uniformly distributed on the BN sheet is also unfeasible, since carbon and boron nitride prefer phase separation. In a word, C-doped BN sheet is not an appropriate material for hydrogen storage applications by H spillover.

Chapter 6

DFT Study of Hydrogen Storage on Carbon Doped Boron

Nitride Fullerene

Following the study on boron nitride sheet in the last chapter, here we are going to investigate another form of BN material, boron nitride fullerene, which has been proposed for hydrogen storage applications. First, we will examine the $(\text{BN})_{12}$ cluster, the smallest stable BN fullerene, to see how C-doping influences the hydrogenation/dehydrogenation properties of BN fullerenes. Then the kinetic issues of the hydrogenation reactions on both pristine and C-doped BN cages will be discussed. At the end, two more BN nanocages, $(\text{BN})_{16}$ and $(\text{BN})_{24}$, will be introduced in our theoretical calculations to see how the material curvature helps in reducing the activation barrier for the hydrogen dissociation on the BN fullerenes.

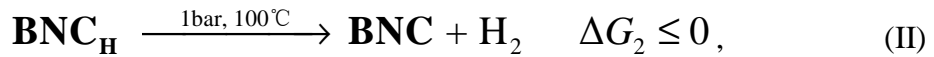
6.1 Introduction

Boron nitride cages (BNC), the analogues of the fullerenes, have been successfully synthesized¹⁰⁶⁻¹⁰⁸ and observed to have the possibility of storing ~3 wt% hydrogen gas.¹⁰⁹ Theoretical prediction¹¹⁰ showed a H_2 storage amount of ~4.9 wt% could be achieved with 38 H_2 molecules in $\text{B}_{60}\text{N}_{60}$. Compared with the storage in carbon cluster, hydrogen is more stable in BN fullerenes, implying that BNC could be good candidates for hydrogen storage materials. However, their research focus on hydrogen storage property of BNC is mainly from the aspect of physisorption, the chemisorption of hydrogen on BNC materials is rarely studied. Recent research pointed out that hydrogen molecules could easily escape from the BN nanocage at room temperature, which would greatly hinder the practical applications of BN fullerenes as hydrogen storage materials.⁴³ It indicates that the physisorption of H_2 molecules in BN cage structures may have its intrinsic drawback in terms of thermal stability for hydrogen storage applications, due to the weak binding strength between H_2 and BN fullerenes. Here, we present a computational study to investigate the

hydrogen chemisorption property of C-doped BN fullerenes, a new class of BNC material. Our prediction indicates that the C-doped BN fullerene is a hydrogen storage material, whose hydrogenation and dehydrogenation reactions can be thermodynamically favored under ambient conditions. The hydrogenation reaction on C-doped BN fullerene is a metal free and self-catalyzed process, in which the C atom works as an activation center for the hydrogen dissociation, and the corresponding activation barrier can be sufficiently low on large curvature BNC materials for practical applications.

6.2 Computational methods

As ideally expected, hydrogen is absorbed in the storage medium at a high pressure, low temperature condition (10 bar, 25 °C), and is released at a low pressure, high temperature condition (1 bar, 100 °C), which ensures safe operations for a practical device.²⁹ Thus, two thermodynamic restrictions for hydrogen storage materials, in terms of BNC, can be set up as follows:



where both Gibbs free energy changes of hydrogenation and dehydrogenation reactions are required to be negative. This helps us screen the appropriate BNC by analyzing the Gibbs free energy changes in the hydrogenation reaction of BNC and dehydrogenation of the corresponding BNC hydride ($\mathbf{BNC}_\mathbf{H}$), in which hydrogen atoms are chemisorbed on the outside of the BNC.

We choose $(\text{BN})_{12}$ (Figure 6.1), the smallest stable BN fullerene,¹¹¹⁻¹¹³ as a representative to search the suitable BNC for hydrogen storage. Since all B sites are equivalent in $(\text{BN})_{12}$ under T_h symmetry, by substituting C atoms for up to two B atoms, we totally get seven BNC structures for investigation. As illustrated in the second column of Table 6.1, the seven BNC are: undoped $(\text{BN})_{12}$ fullerene ($\text{B}_{12}\text{N}_{12}$), 1C-doped $(\text{BN})_{12}$ ($\text{B}_{11}\text{N}_{12}\text{C}$), and five 2C-doped $(\text{BN})_{12}$ with different C-C spans ($\text{B}_{10}\text{N}_{12}\text{C}_2\text{-1} \sim \text{B}_{10}\text{N}_{12}\text{C}_2\text{-5}$). To determine whether these BNC are thermodynamically

avored in the hydrogenation and dehydrogenation reactions, we carried out *ab initio* calculations using hybrid density functional B3LYP method^{70, 71} with the standard 6-31G* basis set, which has been found to be quite adequate for the present system.¹¹⁴ For simulating the full hydrogenation process, we modelled the BNC_H molecules by putting one H atom on each site of the nanocages as our initial structures, where the distance between the H atom and the site is set to be 1 Å. All the structures were fully optimized and found stable, which was examined by vibrational frequency calculations. To study the thermodynamic quantities, Gibbs free energy G , enthalpy H , entropy S , and heat capacity c_v of each structure are calculated with the consideration of the contribution from the vibration. Since the theoretical calculation usually gives a relative overestimation to the vibrational modes, a frequency scaling factor of 0.96 was adopted for thermal energy corrections¹¹⁵ from the vibration of chemical bonds, in order to compare with the experimental results. Then, with standard thermodynamics theory,⁵¹ we can evaluate the thermodynamic properties of each structure under different temperature and pressure conditions. Here, all the calculations were performed with the Gaussian 03 program.⁷⁵

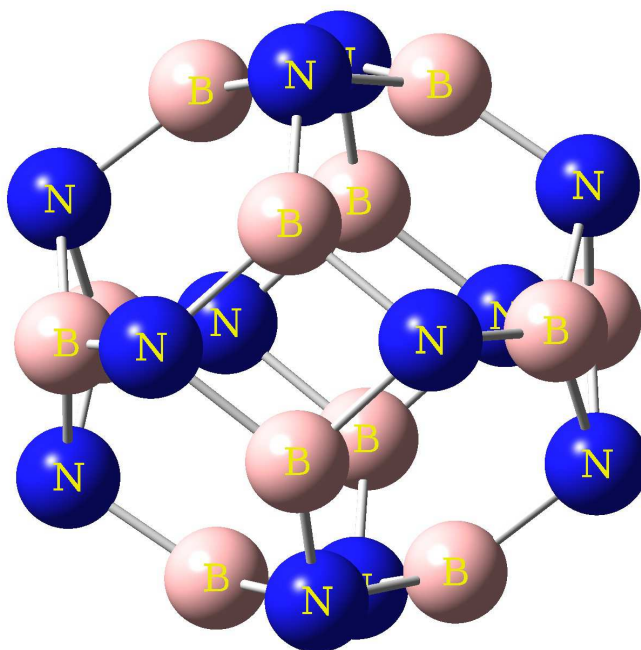


Figure 6.1 $(\text{BN})_{12}$ fullerene with an overall symmetry of T_h , composed of six squares and eight hexagons. All B sites are equivalent, so are all N.

6.3 Results and discussion

6.3.1 Thermodynamics of hydrogen chemisorption on C-doped BN fullerenes

Table 6.1 Calculated thermodynamic data (ΔH_e , ΔG , ΔG_1 , ΔG_2 , kJ/mol; ΔS_e , J/mol-K) per mole of H_2 gas (average values of full hydrogenation) adsorbed/released in the hydrogenation reaction of the BNC, and the maximum hydrogen content (wt%) of the corresponding BNC_H . T_e ($^{\circ}C$) refers to the temperature when Gibbs free energy change for the dehydrogenation reaction equals zero. The front views of investigated BNC molecules are shown (B, pink; C, grey; N, blue).

BNC	ΔH_e	ΔG	ΔS_e	T_e	ΔG_1	ΔG_2	wt%
$B_{12}N_{12}$	55.26	15.79	131.11	148.7	-21.49	6.29	7.46
$B_{11}N_{12}C$	39.31	1.79	125.81	39.3	-7.50	-7.74	7.43
$B_{10}N_{12}C_2$ -1	81.78	38.68	138.68	320.1	-44.39	29.12	6.84
$B_{10}N_{12}C_2$ -2	73.05	31.12	136.53	264.0	-36.83	21.57	6.84
$B_{10}N_{12}C_2$ -3	23.74	-11.90	118.14	-72.5	6.19	-21.53	7.41
$B_{10}N_{12}C_2$ -4	24.62	-11.17	118.85	-66.3	5.47	-20.81	7.41
$B_{10}N_{12}C_2$ -5	23.47	-12.24	118.23	-75.0	6.53	-21.91	7.41

Table 6.1 shows the computational results per mole of H_2 molecules of the

reaction. ΔG_1 is the Gibbs free energy change per mole of H_2 gas adsorbed at 10 bar and 25 °C in reaction (I), calculated as below:

$$\Delta G_1 = [G(\text{BNC}_H) - G(\text{BNC}) - nG(\text{H}_2)] / n, \quad (6.1)$$

where n is the number of H_2 molecules. ΔG_2 is the Gibbs free energy change per mole of H_2 released at 1 bar and 100 °C in reaction (II):

$$\Delta G_2 = [G(\text{BNC}) + nG(\text{H}_2) - G(\text{BNC}_H)] / n. \quad (6.2)$$

ΔG is the Gibbs free energy change for the dehydrogenation reaction calculated at 25 °C and 1 bar via Eq. (6.2). In our case, for the full hydrogenated fullerene, n equals 12, and the calculated Gibbs free energy change per mole of H_2 is actually an average value of the reaction. T_e is the H_2 release equilibrium temperature when Gibbs free energy change for the dehydrogenation reaction equals zero. The corresponding enthalpy and entropy changes, ΔH_e and ΔS_e , are obtained based on Ellingham approximation.² For the $(\text{BN})_{12}$ fullerene, the dehydrogenation reaction is endothermic, with ΔG , ΔH_e and ΔS_e all being positive. Though its free energy change for reaction (I) is negative, 6.29 kJ/mol energy cost in reaction (II) makes the H_2 release at 100 °C not thermodynamically favored for $(\text{BN})_{12}$. With one C atom substituting for a B site on $(\text{BN})_{12}$, the free energy change ΔG is effectively lowered to 1.79 kJ/mol, indicating a much improved dehydrogenation process for $\text{B}_{11}\text{N}_{12}\text{C}$, which is predicted to dehydrogenate spontaneously at 39.3 °C according to our calculations. Moreover, both free energy changes of $\text{B}_{11}\text{N}_{12}\text{C}$ for reaction (I) and (II) are negative, showing that $\text{B}_{11}\text{N}_{12}\text{C}$ can reversibly store 7.43 wt% hydrogen (one H atom adsorbed on each site of $\text{B}_{11}\text{N}_{12}\text{C}$) under ambient conditions. This C-doping

² The changes of enthalpy ΔH_e and entropy ΔS_e per mole of H_2 molecules released at the equilibrium temperature T_e are calculated according to $\Delta H_e = \Delta H(298) + (\Delta c_v/n + R)(T_e - 298)$ and $\Delta S_e = \Delta S(298) + (\Delta c_v/n + R) \ln(T_e / 298)$, where $R = 8.314 \text{ J/mol-K}$, $\Delta H(298)$, $\Delta S(298)$ and Δc_v are respectively the changes of enthalpy, entropy and total heat capacity at 25 °C and 1 bar, calculated in a dehydrogenation reaction. Since the Gibbs free energy change equals zero at T_e , we can have $T_e \approx \Delta H_e / \Delta S_e$.

effect as previously reported for BN nanotubes,^{116, 117} is attributed to the different electronic structures between C and B atoms. Since C atom has one more valence electron than B, B₁₁N₁₂C locally behaves electron-rich and possesses the electron donor property around the C atom. Consequently, the repulsion between the electrons of the H and the π -electrons of the B₁₁N₁₂C nanocage is enhanced, thus weakening the chemical bonds between the hydrogen and the nanocage. Ultimately, hydrogen is more easily released from B₁₁N₁₂C.

Interestingly, as one more C atom doped on the B site, two different effects are observed. On one hand, following the dehydrogenation-enhanced effect as discussed above, the free energy changes ΔG for B₁₀N₁₂C₂-3 ~ B₁₀N₁₂C₂-5 are all negative, implying a thermodynamically favored H₂ release process. But the penalty is that the binding of H atoms onto these BNC becomes difficult due to the positive values of ΔG_1 . On the other hand, when the two C atoms are too close as in the B₁₀N₁₂C₂-1 (C-C: 2.06 Å) and B₁₀N₁₂C₂-2 (C-C: 2.57 Å), the two neighboring N atoms (the two N atoms at the center of BNC front views in Table 6.1) will not adsorb H atoms, because their excessive electrons transferred from the two C atoms greatly weaken the chemical bonds between the nanocage and the hydrogen. Therefore, different from the above cases where a full H coverage of 24 H atoms can be achieved, only 22 H atoms now can be attached to the BNC, resulting in an overall dehydrogenation-worsen effect for B₁₀N₁₂C₂-1 and B₁₀N₁₂C₂-2, whose free energy changes ΔG have larger positive values compared with that of (BN)₁₂. We can draw a conclusion that no more potential BNC for hydrogen storage can be found, as more C atoms replace B atoms in the (BN)₁₂ fullerene (B_{12-x}N₁₂C_x, x>2).

Furthermore, noticeably seen from Table 6.1, the entropy changes of the reactions are around 130 J/mol-K, indicating that the entropy change of the dehydrogenation reaction is mainly due to the release of the hydrogen gas, not much dependent on the structures of BNC molecules.

We have also investigated the other two possible cases, where C atoms substitute for N atoms in (BN)₁₂ fullerene or a B-N pair of (BN)₁₂ is replaced by a C-C pair. Unfortunately, neither of them can provide good candidates for hydrogen storage

materials. Since C atom has one less valence electron than N, $B_{12}N_{12-x}C_x$ ($x=1,2$) is an electron-deficient complex having the electron acceptor property. So the hydrogen chemisorption energy of BNC in the first case is increased, resulting in even worse dehydrogenation property of the corresponding BNC_H . However, this strategy can be applied to BN fullerenes with larger sizes than $(BN)_{12}$, for large BN nanocages with a full H coverage have small H chemisorption energy. As for the second case, which can be viewed as a combination of $(BN)_{12}$ and C_{24} , the same trend as in the first case with respect to the dehydrogenation property is obtained, due to the high release equilibrium temperature of *ca.* 900 °C for C_{24} fullerene.

6.3.2 Kinetics of the hydrogenation reaction on C-doped BN fullerenes

To investigate the kinetic issue in the process of the hydrogenation on the BN fullerene, we calculated the activation barrier for one H_2 fully chemisorbed on the above proposed $B_{11}N_{12}C$ nanocage, as well as that for the undoped $(BN)_{12}$ case for comparison. To obtain a more accurate result of the activation barrier for the hydrogenation reaction, we used the standard 6-31+G** basis set, where both electron diffusion and polarization effects have been included. The transition states located in our calculation were verified by the intrinsic reaction coordinate (IRC) method.^{118, 119}

Figure 6.2 shows the calculated reaction diagram for the H_2 adsorption on the undoped $B_{12}N_{12}$ fullerene. Seen from the schematic diagrams of the initial (IS), transition (TS) and final (FS) states in Figure 6.2, the H_2 molecule initially adsorbs above the B atom of the $B_{12}N_{12}$ cluster, and then as the H_2 further approaches parallel to the B-N bond, the two H atoms gradually separate and a transition state is formed when the H-H bond length is about 0.980 Å. The corresponding activation barrier (energy difference between TS and IS) for the hydrogenation reaction is estimated to be 1.194 eV, which is a little bit high for hydrogen storage applications under ambient conditions. Thus, the pristine $(BN)_{12}$ fullerene has the disadvantage of slow hydrogenation kinetics as a candidate of hydrogen storage materials.

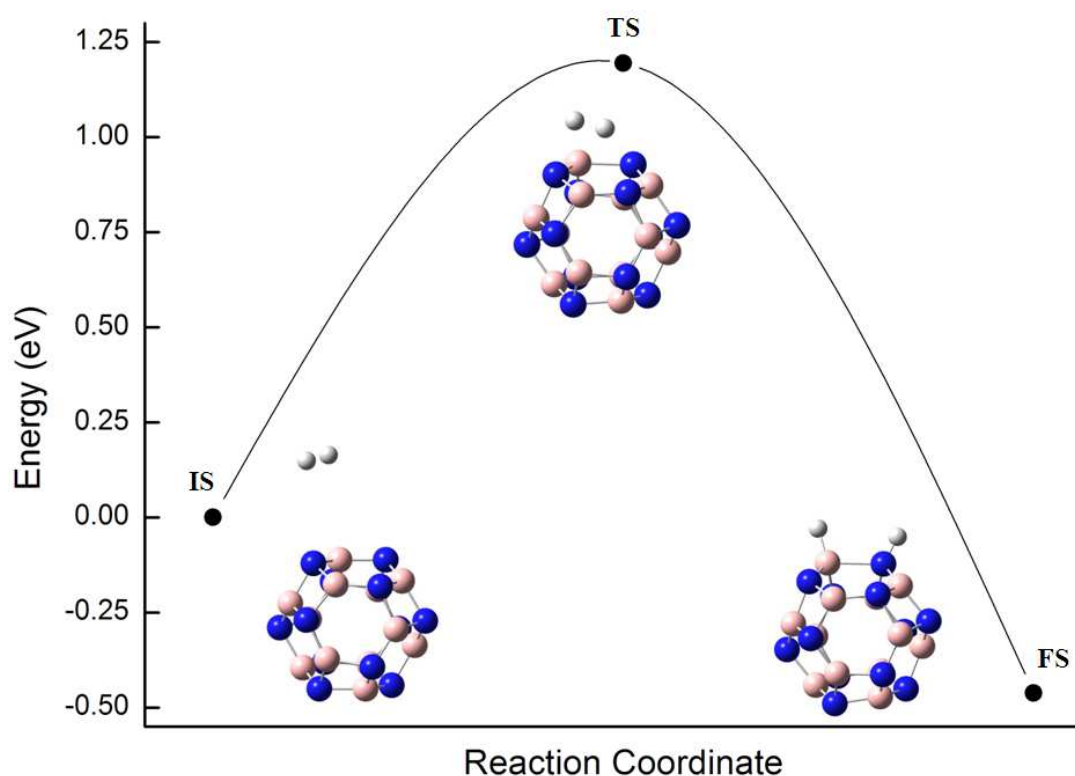


Figure 6.2 Calculated hydrogenation reaction diagram for the undoped $B_{12}N_{12}$ fullerene. The schematic diagrams of initial (IS), transition (TS), and final (FS) states are illustrated by side views (H, white; B, pink; N, blue.). The energy of the reactant (IS), which corresponds to the H_2 physisorption state of $B_{12}N_{12}$, is set to be zero. The activation barrier for the H_2 adsorption on $B_{12}N_{12}$ is about 1.194 eV, and the energy of product (FS) with respect to reactant (IS) is estimated to be -0.464 eV.

Compared with the undoped $(BN)_{12}$ case, the hydrogenation reaction has a much lowered activation barrier for the $B_{11}N_{12}C$ fullerene, as shown in Figure 6.3. Different from the H_2 physisorption manner on $B_{12}N_{12}$, the H_2 molecule is initially adsorbed perpendicularly to the C atom of the $B_{11}N_{12}C$ cluster to form a physisorption state (IS), which is attributed to the polarization effect from the excess electron on the C atom. As the H_2 molecule further approaches the C site, the hydrogen is dissociated with a H-H bond distance of 0.965 Å, where a transition state (TS1) is formed with the activation energy of about 0.468 eV. Then one H atom is adsorbed on C, forming a C-H bond of ~ 1.090 Å; the other H atom detaches away and falls in one intermediate state (IMS1), with the energy of about 0.249 eV higher than that of IS. The dissociated H atom proceeds to diffuse along the C-N path and eventually adsorbs onto the N atom (FS), with a N-H bond of around 1.016 Å. The overall activation

barrier for the hydrogenation reaction on the $B_{11}N_{12}C$ fullerene is about 0.677 eV, much lower than that of 1.194 eV for the undoped $(BN)_{12}$ case. The reaction energy (energy difference between FS and IS) for the H_2 adsorption process on $B_{11}N_{12}C$ is estimated to be -0.411 eV, indicating that a thermodynamically favored hydrogenation reaction can be achieved for the $B_{11}N_{12}C$ fullerene.

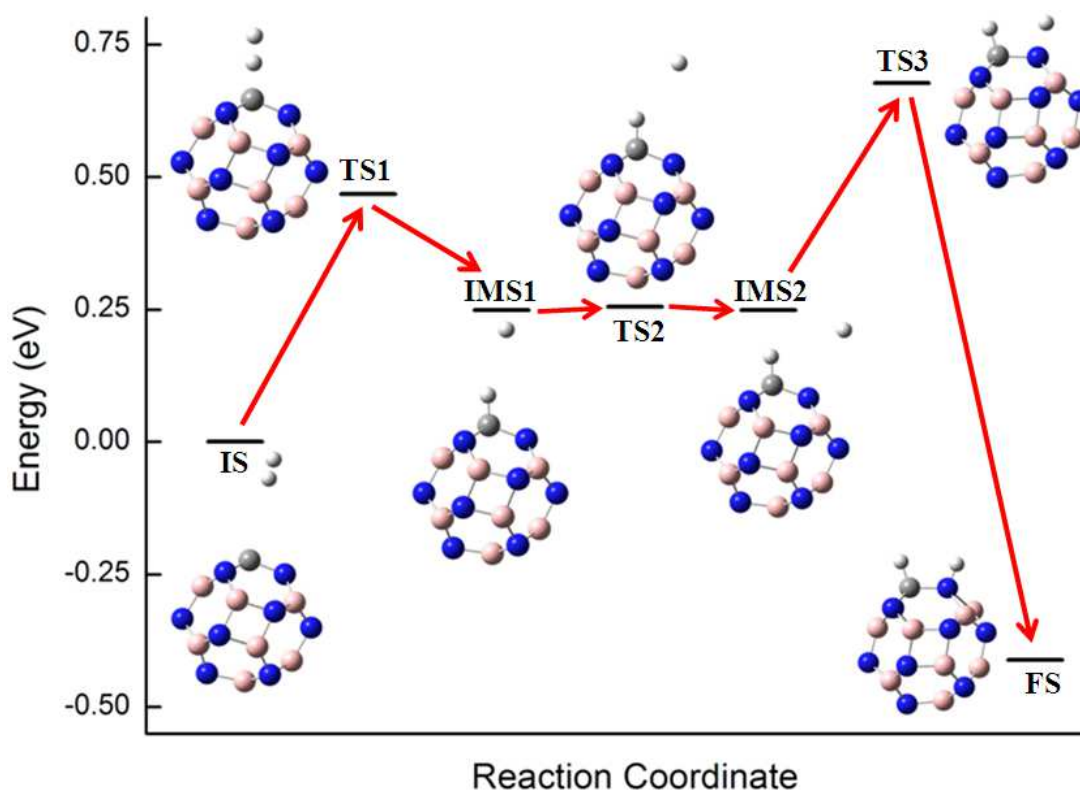


Figure 6.3 Calculated hydrogenation reaction diagram for the $B_{11}N_{12}C$ fullerene. The schematic diagrams of initial (IS), transition (TS), intermediate (IMS), and final (FS) states are illustrated by side views beside each energy bar (H, white; B, pink; C, grey; N, blue.). The energy of the reactant (IS), which corresponds to the H_2 physisorption state of $B_{11}N_{12}C$, is set to be zero. The overall activation barrier for the H_2 adsorption on $B_{11}N_{12}C$ is estimated to be 0.677 eV, much lower than that for the undoped $B_{12}N_{12}$ case. The energy of product (FS) with respect to reactant (IS) is around -0.411 eV, indicating a thermodynamically favored hydrogenation reaction for the $B_{11}N_{12}C$ nanocage.

Noticeably seen from Figure 6.3, the diffusion process for the H atom from IMS1 to IMS2 is almost barrierless. It indicates that the H atom can freely move around the BN fullerene before it chemisorbs stably on the cluster, and the H diffusion process gains fast kinetics, which is of great help in practical applications for hydrogen

storage. The catalytic role of C in the hydrogenation reaction on $B_{11}N_{12}C$ is same as that of a metal cluster in the spillover phenomenon, where H_2 molecules are dissociated by the supported metal cluster, and the dissociated H atoms then further diffuse onto the supporting substrate. However, the catalytic cluster usually used in the spillover consists of noble metals, which are heavy and expensive. This will certainly reduce the overall weight percentage of hydrogen adsorbed and increase the production cost of the storage materials. In our case, the $B_{11}N_{12}C$ fullerene is a self-catalyst in the hydrogenation reaction, where the C atom works as an activation center to dissociate H_2 molecule and provide the free H atom. In this way, a metal free hydrogenation reaction can be readily achieved on the $B_{11}N_{12}C$ cluster, thus both the hydrogen storage capacity and the materials cost are substantially improved.

We have also examined the hydrogenation reaction on the $B_{12}N_{11}C$ fullerene. Just like the $B_{11}N_{12}C$ case, the H_2 molecule initially adsorbs perpendicularly to the active C atom to form a stable physisorption state, and then dissociates with a H-H bond distance of 0.915 Å, forming a transition state with the corresponding activation barrier of about 0.252 eV. Finally, one H atom adsorbs on the C atom, while the other H atom detaches away from the $B_{12}N_{11}C$ cluster. The reaction energy for the H_2 dissociation on $B_{12}N_{11}C$ with respect to the physisorption state is estimated to be -0.010 eV, indicating that a thermodynamically favored hydrogenation reaction can be achieved on the $B_{12}N_{11}C$ fullerene.

Since C atom has one less valence electron than N, it exhibits the electron acceptor property for $B_{12}N_{11}C$ around the C atom. More electrons can be transferred from hydrogen to $B_{12}N_{11}C$ and thus lower activation energy for hydrogen dissociation can be achieved on the $B_{12}N_{11}C$ fullerene, compared with the $B_{11}N_{12}C$ case. On one hand, the electron-deficient doping (one C replacing one N, $B_{12}N_{11}C$) is more kinetically favored than the electron-sufficient doping (one C replacing one B, $B_{11}N_{12}C$) for the hydrogenation reaction on the $(BN)_{12}$ fullerene. On the other hand, $B_{11}N_{12}C$ is more thermodynamically favored than $B_{12}N_{11}C$ for full hydrogenation and dehydrogenation reactions on the BN cluster, as we have discussed in the previous section; however, we have also pointed out that the electron-deficient doping would

become more thermodynamically suitable than the electron-sufficient doping for the BN fullerenes that are larger than $(\text{BN})_{12}$ as hydrogen storage materials. Thus, to replace B or N by C depends on the size of the BN cluster.

From the above results, we can see that C-doping can effectively lower the activation barrier for the hydrogenation reaction on the BN fullerene, thus facilitating the hydrogen storage applications of the materials. In addition, the electron-deficient doping ($\text{B}_{12}\text{N}_{11}\text{C}$) has a lower activation barrier for the hydrogen dissociation than the electron-sufficient doping ($\text{B}_{11}\text{N}_{12}\text{C}$), which has the same preference as that for the H migration in the hydrogen spillover process, as we have discussed in the last chapter.

6.3.3 Curvature effect on the hydrogenation kinetics of C-doped BN fullerenes

As we have discussed in the last chapter, the direct dissociation of hydrogen on C-doped BN sheet is difficult; however, it becomes possible for the H_2 dissociation on C-doped $(\text{BN})_{12}$ fullerene without the help of metal catalyst according to our calculations. So it seems that the curvature of small BN nanocage facilitates the sp^3 -hybridization of the C atom and thus helps in the hydrogenation reaction on the C-doped BN fullerene.

To further investigate the curvature effect on the hydrogenation kinetics of C-doped BN fullerenes, we have studied the H_2 dissociation on two other BN nanocages, $(\text{BN})_{16}$ and $(\text{BN})_{24}$, with bigger size (smaller curvature) than that of $(\text{BN})_{12}$ fullerene. $(\text{BN})_{16}$ is the second smallest stable BN fullerene,^{112, 113} and is composed of six squares and twelve hexagons under the symmetry of T_d (Figure 6.4a). $(\text{BN})_{24}$ has been successfully synthesized,¹²⁰ and consists of twelve squares, eight hexagons and six octagons under the symmetry of O (Figure 6.4b). To compare with the data we have got for $(\text{BN})_{12}$, we doped one C atom into these two BN fullerenes, and calculated the activation energy for the H_2 dissociation on the pristine/C-doped $(\text{BN})_{16}$ and $(\text{BN})_{24}$ nanocages.

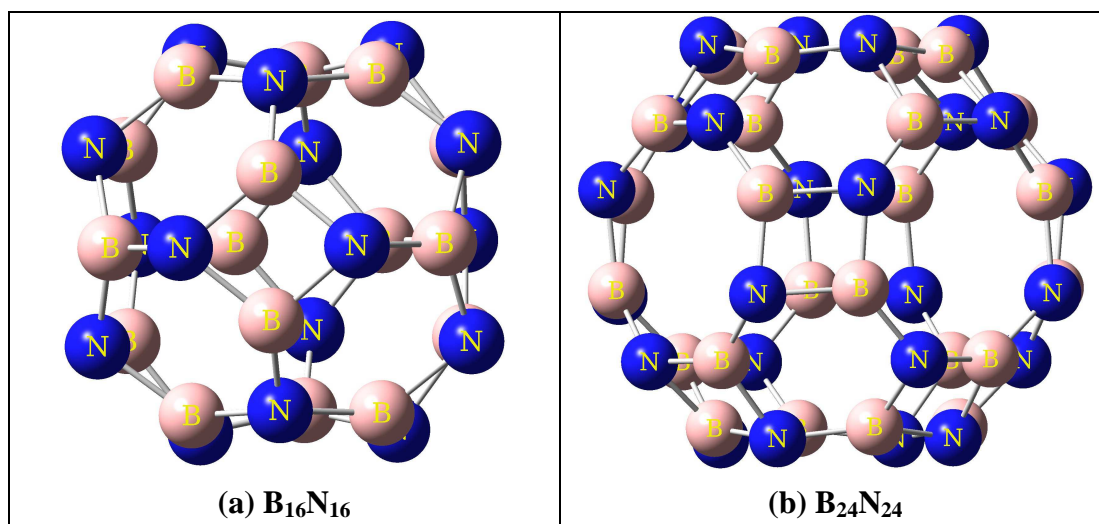
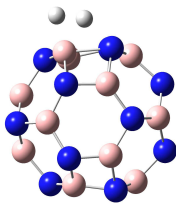
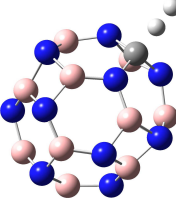
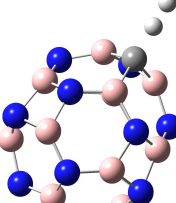
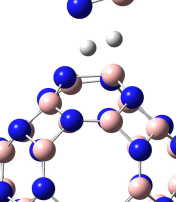
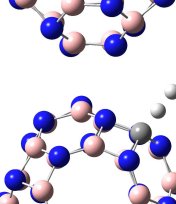
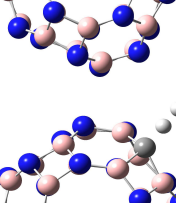


Figure 6.4 (a) $(\text{BN})_{16}$ fullerene under the symmetry of T_d , composed of six squares and twelve hexagons; (b) $(\text{BN})_{24}$ fullerene under the symmetry of O , composed of twelve squares, eight hexagons and six octagons.

Table 6.2 shows the calculated activation energy, reaction energy, and the H-H bond distance in the transition state, for the hydrogenation reaction on pristine/C-doped $(\text{BN})_{16}$ and $(\text{BN})_{24}$ fullerenes. The same hydrogenation manner as that for pristine/C-doped $(\text{BN})_{12}$ has been obtained for the corresponding $(\text{BN})_{16}$ and $(\text{BN})_{24}$ clusters. For the undoped $(\text{BN})_{16}$ and $(\text{BN})_{24}$, the H_2 molecule adsorbs above the B site first, and then dissociates on the B-N bond; while for the C-doped case, the H_2 molecule adsorbs perpendicularly to the C atom, and then dissociates into two H atoms, one forming a C-H bond and the other detaching away from the fullerene. Combining the data in Table 6.2 and that for $(\text{BN})_{12}$, we can see that both activation energy and reaction energy increase with the size of the BN fullerene, and the electron-deficient doping ($\text{B}_{12}\text{N}_{11}\text{C}$, $\text{B}_{16}\text{N}_{15}\text{C}$, $\text{B}_{24}\text{N}_{23}\text{C}$) is the most favorable method to lower the hydrogenation barrier on the BN fullerene of each size. The curvature effect on the hydrogenation kinetics of BN fullerenes is obvious, and the small BN nanocage with large curvature is preferred for hydrogen storage applications.

Table 6.2 Calculated activation energy (E_a), reaction energy (E_r), and the H-H bond distance ($d_{\text{H-H}}$) in the transition state, for the hydrogenation reaction on pristine/C-doped (BN) $_{16}$ and (BN) $_{24}$ fullerenes. The side views of the transition states (TS) for the hydrogen dissociation on these clusters are shown (H, white; B, pink; C, grey; N, blue).

BNC	TS	E_a (eV)	E_r (eV)	$d_{\text{H-H}}$ (Å)
B $_{16}$ N $_{16}$		1.276	-0.472	0.986
B $_{15}$ N $_{16}$ C		0.497	0.307	0.985
B $_{16}$ N $_{15}$ C		0.306	0.080	0.942
B $_{24}$ N $_{24}$		1.514	0.100	0.996
B $_{23}$ N $_{24}$ C		0.608	0.494	1.063
B $_{24}$ N $_{23}$ C		0.399	0.221	1.006

6.4 Summary

In summary, by introducing C atoms into $(\text{BN})_{12}$ fullerene, full hydrogenation calculations show that the $\text{B}_{11}\text{N}_{12}\text{C}$ compound can spontaneously store hydrogen at room temperature and 10 bar and release hydrogen at 100 °C and 1 bar, with the hydrogen storage capacity of up to 7.43 wt%, indicating that $\text{B}_{11}\text{N}_{12}\text{C}$ is a potential candidate for hydrogen storage materials. Further investigation on the hydrogenation reactions of BN fullerenes shows that C-doped BN nanocage can effectively dissociate the H_2 molecule with the C atom as an activation center, and the corresponding activation barrier for the H_2 chemisorption is substantially lowered, compared with the undoped case. The hydrogenation reaction turns out to be a metal free and self-catalyzed process on C-doped BN fullerene, indicating that C doping is an effective approach in modifying the hydrogen storage property of the BN fullerene. There is also a curvature effect on the hydrogenation kinetics of BN fullerenes, that small BN nanocage with large curvature would be beneficial for practical applications as hydrogen storage material. We hope that our research work will stimulate the experimental effort in this direction.

Chapter 7

Conclusions and Future Work

7.1 Conclusions

In chapter 3-6, I have studied the hydrogen spillover effect on graphene and boron nitride sheet, as well as the hydrogen storage property of boron nitride fullerenes with a focus on the doping effect and the kinetic issues. Through DFT calculations, we can see that doping method is very effective in improving the hydrogenation ability and the metal binding strength of graphene and BN sheet. A stable catalytic center is then created with metal catalyst supported on the substrate, where H_2 molecules efficiently dissociate into H atoms on the metal cluster and the H subsequently migrates onto the supporting sheet with a much lowered activation barrier, compared with the undoped case. On one hand, to have a steady catalytic performance on the substrate, the metal cluster upon H saturation is required to keep contact with the underlying sheet, thus the electron-deficient doping (G_B , G_{pyr-N} , and $BN-C_N$), which can have stronger metal binding strength and chemisorb more H atoms than the electron-sufficient doping (G_N and $BN-C_B$), is the preferred method to modify surface properties of graphene or BN sheet. On the other hand, since the local doping effect is too strong to have the H atom diffuse away on the substrate, a supporting substrate with dopants uniformly distributed is beneficial to the H diffusion process on it, thus facilitating the hydrogen storage applications under ambient conditions. As we have proposed, the uniform BC_3 sheet is a good candidate of hydrogen storage material via hydrogen spillover. Both H migration and diffusion processes on the BC_3 sheet are investigated to have low activation barriers within 0.7 eV. However, no proper materials with uniform distributions of N dopants on the graphene were ever reported. It is also not favored to have C uniformly distributed on the BN sheet, since carbon and boron nitride prefer phase separation.

According to our calculations, both hydrogen spillover and direct hydrogen dissociation on C-doped BN sheet are not applicable under ambient conditions. We

then proceed to study the C-doping effect on the hydrogen storage properties of boron nitride fullerenes. By introducing C atoms into (BN)₁₂ fullerene, full hydrogenation calculations show that C-doping has great tunability of the thermodynamic properties of BN nanocages, and the B₁₁N₁₂C compound is predicted to be able to reversibly adsorb up to 7.43 wt% hydrogen under ambient conditions, being a potential candidate of hydrogen storage materials. In addition, the H₂ molecule can be effectively dissociated via the doped C atom as an activation center on the BN fullerene, with the substantially lowered activation barrier for the H₂ chemisorption process, compared with the undoped case. It turns out to be a metal free and self-catalyzed process for the hydrogenation reaction on C-doped BN fullerene. Compared with the BN sheet, the curvatures do have an influence on the hydrogenation kinetics of BN fullerenes, i.e. small BN nanocage with large curvature has the advantage for practical applications as hydrogen storage material.

Our calculations conclude that graphene-based materials are more suitable for hydrogen storage applications by hydrogen spillover rather than materials based on the BN sheet, and the small BN fullerene with large curvature also has its advantage over the BN sheet as potential hydrogen storage materials. Doping is an effective approach in modifying hydrogen storage properties of materials and the improved hydrogenation kinetics can thus be expected. We propose that the BC₃ sheet with proper metal catalyst and the B₁₁N₁₂C fullerene should be potential candidates of hydrogen storage materials and hope our research work will stimulate the experimental effort in this direction.

7.2 Future work

Through the calculation results of the hydrogen spillover on B/N-doped graphene in this thesis, we can see that there are still a lot of options that may improve the hydrogen spillover process and these would be the future research directions in this field.

First, as we have suggested in chapter 4, the co-doping of graphitic-N and pyridinic-N on the graphene sheet, where graphitic-N may distribute among

pyridinic-N with some pattern, could facilitate the hydrogen spillover on N-doped graphene. The single pyridinic-N can firmly bind the metal cluster, which then dissociates H₂ molecules into H atoms, followed by H migration from metal to substrate; while the graphitic-N is expected to lower the activation barrier for the diffusion of the migrated H atom on the graphene sheet. In this way, two types of doped N are used for different purposes, and the ratio of these two types on the graphene needs to be determined for an optimal effect of the hydrogen storage by spillover.

Second, the metal catalyst we used in the theoretical study is Pt₄ cluster, and the average binding strength $|\Delta E_{\text{chem}}|$ of H atoms on the saturated Pt₄ seems to be too high. If the $|\Delta E_{\text{chem}}|$ can be lowered by using other metal catalyst, then the H migration barrier would be lowered accordingly. From this point, Ni, Pd and Ru are all possible alternatives to Pt, and whether they can provide good catalytic performance for hydrogen spillover needs to be investigated.

Another thing needs to be mentioned is that the microporous carbon materials investigated for hydrogen spillover in the experiments are not flat sheet materials. So the curvatures of these materials may have some effects on the kinetic issues in the H spillover process, like what we have seen for the BN fullerenes in chapter 6. To model the more realistic system like the microporous carbon, molecular dynamics (MD) method should be used in order to treat the relatively complex system, and the hydrogen dissociation, migration and diffusion processes can be viewed in MD simulations. The kinetics of the hydrogen spillover under ambient conditions can also be investigated with MD, which serves as a helpful tool in the future research work on the hydrogen storage by spillover.

References

- [1] L. Schlapbach and A. Züttel, *Nature* **414**, 353 (2001).
- [2] S. Satyapal, J. Petrovic, C. Read, G. Thomas, and G. Ordaz, *Catal. Today* **120**, 246 (2007).
- [3] G. W. Crabtree and M. S. Dresselhaus, *MRS Bull.* **33**, 421 (2008).
- [4] Y. Ye, C. C. Ahn, C. Witham, B. Fultz, J. Liu, A. G. Rinzler, D. Colbert, K. A. Smith, and R. E. Smalley, *Appl. Phys. Lett.* **74**, 2307 (1999).
- [5] W. Q. Deng, X. Xu, and W. A. Goddard, *Phys. Rev. Lett.* **92**, 166103 (2004).
- [6] Z. X. Yang, Y. D. Xia, and R. Mokaya, *J. Am. Chem. Soc.* **129**, 1673 (2007).
- [7] J. Y. Lee, C. D. Wood, D. Bradshaw, M. J. Rosseinsky, and A. I. Cooper, *Chem. Commun.*, 2670 (2006).
- [8] P. M. Budd, A. Butler, J. Selbie, K. Mahmood, N. B. McKeown, B. Ghanem, K. Msayib, D. Book, and A. Walton, *Phys. Chem. Chem. Phys.* **9**, 1802 (2007).
- [9] A. Li, R. F. Lu, Y. Wang, X. Wang, K. L. Han, and W. Q. Deng, *Angew. Chem.-Int. Edit.* **49**, 3330 (2010).
- [10] J. L. C. Rowsell and O. M. Yaghi, *Angew. Chem.-Int. Edit.* **44**, 4670 (2005).
- [11] S. S. Han, W. Q. Deng, and W. A. Goddard, *Angew. Chem.-Int. Edit.* **46**, 6289 (2007).
- [12] S. H. Yang, X. Lin, A. J. Blake, G. S. Walker, P. Hubberstey, N. R. Champness, and M. Schroder, *Nat. Chem.* **1**, 487 (2009).
- [13] B. Schmitz, U. Muller, N. Trukhan, M. Schubert, G. Ferey, and M. Hirscher, *ChemPhysChem* **9**, 2181 (2008).
- [14] A. D. Lueking and R. T. Yang, *Appl. Catal. A* **265**, 259 (2004).
- [15] A. Lueking and R. T. Yang, *J. Catal.* **206**, 165 (2002).
- [16] A. J. Lachawiec, G. S. Qi, and R. T. Yang, *Langmuir* **21**, 11418 (2005).
- [17] Y. W. Li and R. T. Yang, *J. Am. Chem. Soc.* **128**, 726 (2006).
- [18] Y. W. Li and R. T. Yang, *J. Am. Chem. Soc.* **128**, 8136 (2006).
- [19] Y. W. Li and R. T. Yang, *AIChE J.* **54**, 269 (2008).
- [20] B. Bogdanovic and M. Schwickardi, *J. Alloy Compd.* **253**, 1 (1997).
- [21] C. M. Jensen, R. Zidan, N. Mariels, A. Hee, and C. Hagen, *Int. J. Hydrogen Energy* **24**, 461 (1999).
- [22] P. Chen, Z. T. Xiong, J. Z. Luo, J. Y. Lin, and K. L. Tan, *Nature* **420**, 302 (2002).
- [23] J. J. Vajo, S. L. Skeith, and F. Mertens, *J. Phys. Chem. B* **109**, 3719 (2005).
- [24] V. Ozolins, E. H. Majzoub, and C. Wolverton, *J. Am. Chem. Soc.* **131**, 230 (2009).
- [25] E. Ronnebro and E. H. Majzoub, *J. Phys. Chem. B* **111**, 12045 (2007).
- [26] M. Chong, A. Karkamkar, T. Autrey, S. Orimo, S. Jalisatgi, and C. M. Jensen, *Chem. Commun.* **47**, 1330 (2011).
- [27] S. Hodoshima, H. Arai, S. Takaiwa, and Y. Saito, *Int. J. Hydrogen Energy* **28**, 1255 (2003).

-
- [28] A. Moores, M. Poyatos, Y. Luo, and R. H. Crabtree, *New J. Chem.* **30**, 1675 (2006).
- [29] R. F. Lu, G. Boethius, S. H. Wen, Y. Su, and W. Q. Deng, *Chem. Commun.*, 1751 (2009).
- [30] P. G. Campbell, L. N. Zakharov, D. J. Grant, D. A. Dixon, and S. Y. Liu, *J. Am. Chem. Soc.* **132**, 3289 (2010).
- [31] P. Wang and X. D. Kang, *Dalton Trans.*, 5400 (2008).
- [32] C. W. Hamilton, R. T. Baker, A. Staubitz, and I. Manners, *Chem. Soc. Rev.* **38**, 279 (2009).
- [33] M. E. Bluhm, M. G. Bradley, R. Butterick, U. Kusari, and L. G. Sneddon, *J. Am. Chem. Soc.* **128**, 7748 (2006).
- [34] F. H. Stephens, R. T. Baker, M. H. Matus, D. J. Grant, and D. A. Dixon, *Angew. Chem.-Int. Edit.* **46**, 746 (2007).
- [35] A. D. Sutton, A. K. Burrell, D. A. Dixon, E. B. Garner, J. C. Gordon, T. Nakagawa, K. C. Ott, J. P. Robinson, and M. Vasiliu, *Science* **331**, 1426 (2011).
- [36] M. Rzepka, P. Lamp, and M. A. de la Casa-Lillo, *J. Phys. Chem. B* **102**, 10894 (1998).
- [37] G. Garberoglio, A. I. Skoulidas, and J. K. Johnson, *J. Phys. Chem. B* **109**, 13094 (2005).
- [38] G. K. Dimitrakakis, E. Tylianakis, and G. E. Froudakis, *Nano Lett.* **8**, 3166 (2008).
- [39] S. S. Han, J. L. Mendoza-Cortes, and W. A. Goddard, *Chem. Soc. Rev.* **38**, 1460 (2009).
- [40] H. Gunaydin, K. N. Houk, and V. Ozolins, *Proc. Natl. Acad. Sci. USA* **105**, 3673 (2008).
- [41] X. W. Sha, M. T. Knippenberg, A. C. Cooper, G. P. Pez, and H. S. Cheng, *J. Phys. Chem. C* **112**, 17465 (2008).
- [42] F. Salles, H. Jobic, G. Maurin, M. M. Koza, P. L. Llewellyn, T. Devic, C. Serre, and G. Ferey, *Phys. Rev. Lett.* **100**, 245901 (2008).
- [43] Q. Sun, Q. Wang, and P. Jena, *Nano Lett.* **5**, 1273 (2005).
- [44] O. V. Pupysheva, A. A. Farajian, and B. I. Yakobson, *Nano Lett.* **8**, 767 (2008).
- [45] P. Hohenberg and W. Kohn, *Phys. Rev.* **136**, B864 (1964).
- [46] W. Kohn and L. J. Sham, *Phys. Rev.* **140**, A1133 (1965).
- [47] R. C. Lochan and M. Head-Gordon, *Phys. Chem. Chem. Phys.* **8**, 1357 (2006).
- [48] F. Negri and N. Saendig, *Theor. Chem. Acc.* **118**, 149 (2007).
- [49] B. Magyari-Kope, V. Ozolins, and C. Wolverton, *Phys. Rev. B* **73**, 220101 (2006).
- [50] C. Wolverton and V. Ozolins, *Phys. Rev. B* **75**, 064101 (2007).
- [51] J. W. Ochterski, *Thermochemistry in Gaussian*, Gaussian, Inc., April 2000, http://www.gaussian.com/g_whitepap/thermo.htm.
- [52] S. V. Alapati, J. K. Johnson, and D. S. Sholl, *Phys. Chem. Chem. Phys.* **9**, 1438 (2007).
- [53] M. Yoon, S. Y. Yang, E. Wang, and Z. Y. Zhang, *Nano Lett.* **7**, 2578 (2007).

-
- [54] J. Zhou, Q. Wang, Q. Sun, P. Jena, and X. S. Chen, Proc. Natl. Acad. Sci. USA **107**, 2801 (2010).
- [55] L. Spruch, Rev. Mod. Phys. **63**, 151 (1991).
- [56] J. C. Slater, Phys. Rev. **34**, 1293 (1929).
- [57] J. C. Slater, Phys. Rev. **81**, 385 (1951).
- [58] B. T. Sutcliffe, "Breakdown of the Born-Oppenheimer Approximation," in *Handbook of Molecular Physics and Quantum Chemistry*, edited by S. Wilson (John Wiley & Sons, Chichester, 2003), Vol. 1, p. 599.
- [59] J. C. Slater, *Quantum Theory of Molecules and Solids*, Vol. IV, McGraw-Hill, New York, 1982.
- [60] D. Ceperley, Phys. Rev. B **18**, 3126 (1978).
- [61] U. v. Barth and L. Hedin, J. Phys. C **5**, 1629 (1972).
- [62] O. Gunnarsson and B. I. Lundqvist, Phys. Rev. B **13**, 4274 (1976).
- [63] S. H. Vosko, L. Wilk, and M. Nusair, Can. J. Phys. **58**, 1200 (1980).
- [64] J. P. Perdew and A. Zunger, Phys. Rev. B **23**, 5048 (1981).
- [65] A. D. Becke, Phys. Rev. A **38**, 3098 (1988).
- [66] C. Lee, W. Yang, and R. G. Parr, Phys. Rev. B **37**, 785 (1988).
- [67] J. P. Perdew, J. A. Chevary, S. H. Vosko, K. A. Jackson, M. R. Pederson, D. J. Singh, and C. Fiolhais, Phys. Rev. B **46**, 6671 (1992).
- [68] J. P. Perdew, K. Burke, and M. Ernzerhof, Phys. Rev. Lett. **77**, 3865 (1996).
- [69] A. D. Becke, J. Chem. Phys. **98**, 1372 (1993).
- [70] P. J. Stephens, F. J. Devlin, C. F. Chabalowski, and M. J. Frisch, J. Phys. Chem. **98**, 11623 (1994).
- [71] A. D. Becke, J. Chem. Phys. **98**, 5648 (1993).
- [72] S. J. Clark, M. D. Segall, C. J. Pickard, P. J. Hasnip, M. I. J. Probert, K. Refson, and M. C. Payne, Z. Kristallogr. **220**, 567 (2005).
- [73] B. Delley, J. Chem. Phys. **92**, 508 (1990).
- [74] B. Delley, J. Chem. Phys. **113**, 7756 (2000).
- [75] Gaussian 03, M. J. Frisch, G. W. Trucks, H. B. Schlegel, G. E. Scuseria, M. A. Robb, J. R. Cheeseman, J. A. Montgomery, Jr., T. Vreven, K. N. Kudin, J. C. Burant, J. M. Millam, S. S. Iyengar, J. Tomasi, V. Barone, B. Mennucci, M. Cossi, G. Scalmani, N. Rega, G. A. Petersson, H. Nakatsuji, M. Hada, M. Ehara, K. Toyota, R. Fukuda, J. Hasegawa, M. Ishida, T. Nakajima, Y. Honda, O. Kitao, H. Nakai, M. Klene, X. Li, J. E. Knox, H. P. Hratchian, J. B. Cross, V. Bakken, C. Adamo, J. Jaramillo, R. Gomperts, R. E. Stratmann, O. Yazyev, A. J. Austin, R. Cammi, C. Pomelli, J. W. Ochterski, P. Y. Ayala, K. Morokuma, G. A. Voth, P. Salvador, J. J. Dannenberg, V. G. Zakrzewski, S. Dapprich, A. D. Daniels, M. C. Strain, O. Farkas, D. K. Malick, A. D. Rabuck, K. Raghavachari, J. B. Foresman, J. V. Ortiz, Q. Cui, A. G. Baboul, S. Clifford, J. Cioslowski, B. B. Stefanov, G. Liu, A. Liashenko, P. Piskorz, I. Komaromi, R. L. Martin, D. J. Fox, T. Keith, M. A. Al-Laham, C. Y. Peng, A. Nanayakkara, M. Challacombe, P. M. W. Gill, B. Johnson, W. Chen, M. W. Wong, C. Gonzalez, and J. A. Pople, Gaussian, Inc., Wallingford CT, 2004.
- [76] G. Kresse and J. Hafner, Phys. Rev. B **47**, 558 (1993).

-
- [77] G. Kresse and J. Furthmuller, *Comp. Mater. Sci.* **6**, 15 (1996).
- [78] L. F. Wang and R. T. Yang, *Energy Environ. Sci.* **1**, 268 (2008).
- [79] L. Chen, A. C. Cooper, G. P. Pez, and H. Cheng, *J. Phys. Chem. C* **111**, 18995 (2007).
- [80] G. M. Psofogiannakis and G. E. Froudakis, *J. Phys. Chem. C* **113**, 14908 (2009).
- [81] A. K. Singh, M. A. Ribas, and B. I. Yakobson, *Acs Nano* **3**, 1657 (2009).
- [82] Y. Ferro, F. Marinelli, A. Jelea, and A. Allouche, *J. Chem. Phys.* **120**, 11882 (2004).
- [83] Z. H. Zhu, G. Q. Lu, and H. Hatori, *J. Phys. Chem. B* **110**, 1249 (2006).
- [84] T. C. M. Chung, Y. Jeong, Q. Chen, A. Kleinhammes, and Y. Wu, *J. Am. Chem. Soc.* **130**, 6668 (2008).
- [85] Y. Jeong and T. C. M. Chung, *Carbon* **48**, 2526 (2010).
- [86] L. F. Wang, F. H. Yang, and R. T. Yang, *AIChE J.* **55**, 1823 (2009).
- [87] H. J. Monkhorst and J. D. Pack, *Phys. Rev. B* **13**, 5188 (1976).
- [88] N. Govind, M. Petersen, G. Fitzgerald, D. King-Smith, and J. Andzelm, *Comp. Mater. Sci.* **28**, 250 (2003).
- [89] F. L. Hirshfeld, *Theo. Chim. Acta* **44**, 129 (1977).
- [90] C. G. Zhou, J. P. Wu, A. H. Nie, R. C. Forrey, A. Tachibana, and H. S. Cheng, *J. Phys. Chem. C* **111**, 12773 (2007).
- [91] A. Schenk, B. Winter, C. Lutterloh, J. Biener, U. A. Schubert, and J. Kupperts, *J. Nucl. Mater.* **222**, 767 (1995).
- [92] J. Kouvetakis, R. B. Kaner, M. L. Sattler, and N. Bartlett, *J. Chem. Soc. Chem. Commun.*, 1758 (1986).
- [93] C. J. Zhang and A. Alavi, *J. Chem. Phys.* **127**, 214704 (2007).
- [94] X. W. Sha, A. C. Cooper, W. H. Bailey, and H. S. Cheng, *J. Phys. Chem. C* **114**, 3260 (2010).
- [95] Z. X. Yang, Y. D. Xia, X. Z. Sun, and R. Mokaya, *J. Phys. Chem. B* **110**, 18424 (2006).
- [96] Y. D. Xia, G. S. Walker, D. M. Grant, and R. Mokaya, *J. Am. Chem. Soc.* **131**, 16493 (2009).
- [97] Y. Y. Shao, J. H. Sui, G. P. Yin, and Y. Z. Gao, *Appl. Catal. B-Environ.* **79**, 89 (2008).
- [98] Y. K. Zhou, R. Pasquarelli, T. Holme, J. Berry, D. Ginley, and R. O'Hayre, *J. Mater. Chem.* **19**, 7830 (2009).
- [99] L. F. Wang and R. T. Yang, *J. Phys. Chem. C* **113**, 21883 (2009).
- [100] P. X. Hou, H. Orikasa, T. Yamazaki, K. Matsuoka, A. Tomita, N. Setoyama, Y. Fukushima, and T. Kyotani, *Chem. Mater.* **17**, 5187 (2005).
- [101] L. S. Zhang, X. Q. Liang, W. G. Song, and Z. Y. Wu, *Phys. Chem. Chem. Phys.* **12**, 12055 (2010).
- [102] Z. H. Zhu, H. Hatori, S. B. Wang, and G. Q. Lu, *J. Phys. Chem. B* **109**, 16744 (2005).
- [103] W. Q. Han, L. J. Wu, Y. M. Zhu, K. Watanabe, and T. Taniguchi, *Appl. Phys. Lett.* **93**, 223103 (2008).

-
- [104] S. A. Shevlin and Z. X. Guo, *Phys. Rev. B* **76**, 024104 (2007).
- [105] W. Paszkowicz, J. B. Pelka, M. Knapp, T. Szyszko, and S. Podsiadlo, *Appl. Phys. A-Mater. Sci. Process.* **75**, 431 (2002).
- [106] O. Stephan, Y. Bando, A. Loiseau, F. Willaime, N. Shramchenko, T. Tamiya, and T. Sato, *Appl. Phys. A-Mater. Sci. Process.* **67**, 107 (1998).
- [107] T. Oku, A. Nishiwaki, and I. Narita, *Sci. Technol. Adv. Mater.* **5**, 635 (2004).
- [108] T. Oku, I. Narita, and A. Nishiwaki, *Mater. Manuf. Process.* **19**, 1215 (2004).
- [109] T. Oku, M. Kuno, and I. Narita, *J. Phys. Chem. Solids* **65**, 549 (2004).
- [110] N. Koi and T. Oku, *Solid State Commun.* **131**, 121 (2004).
- [111] F. Jensen and H. Toftlund, *Chem. Phys. Lett.* **201**, 89 (1993).
- [112] G. Seifert, P. W. Fowler, D. Mitchell, D. Porezag, and T. Frauenheim, *Chem. Phys. Lett.* **268**, 352 (1997).
- [113] W. H. Moon, M. S. Son, and H. J. Hwang, *Appl. Surf. Sci.* **253**, 7078 (2007).
- [114] X. F. Fan, Z. X. Zhu, Z. X. Shen, and J. L. Kuo, *J. Phys. Chem. C* **112**, 15691 (2008).
- [115] R. D. Johnson III, NIST Computational Chemistry Comparison and Benchmark Database, NIST Standard Reference Database Number 101, Release 14, Sept 2006, <http://srdata.nist.gov/cccbdb>.
- [116] S. H. Jhi and Y. K. Kwon, *Phys. Rev. B* **69**, 245407 (2004).
- [117] R. J. Baierle, P. Piquini, T. M. Schmidt, and A. Fazzio, *J. Phys. Chem. B* **110**, 21184 (2006).
- [118] C. Gonzalez and H. B. Schlegel, *J. Chem. Phys.* **90**, 2154 (1989).
- [119] C. Gonzalez and H. B. Schlegel, *J. Phys. Chem.* **94**, 5523 (1990).
- [120] T. Oku, A. Nishiwaki, I. Narita, and M. Gonda, *Chem. Phys. Lett.* **380**, 620 (2003).